

DYNAMICAL PROPERTIES OF STRONGLY CORRELATED FERMIONIC SYSTEMS

Stephan W. Haas, Ph.D.
Florida State University, 1995
Major Professor: E. R. Dagotto, Ph.D.

The Exact Diagonalization method is a powerful numerical tool to study Quantum Many Body systems on finite clusters. In particular, using this technique one can accurately calculate energy and momentum dependent dynamic correlation functions which are observable in scattering experiments, such as Neutron Scattering, Raman Scattering, and Photoemission Spectroscopy which measures the spectral function of the system. Here we give an outline of the Lanczos method with special emphasis on the evaluation of dynamical quantities.

In this thesis, we apply this method to two-dimensional models of strongly correlated electrons which are believed to describe the physics of the recently discovered cuprate high- T_c compounds. We show that simple models of strongly correlated electrons, such as the Hubbard and the t-J model, can account for some normal state properties of these materials. In particular, the occurrence of photoemission bands which are introduced by short-range antiferromagnetic correlations is discussed.

The precursor materials of the cuprate superconductors are antiferromagnets. Here, we address the properties of antiferromagnets as they evolve from an insulating

to a metallic phase upon doping. We focus on the shape of the Fermi surface at small hole doping and on the influence of long-range Coulomb interactions on the occurrence of superconducting and charge density wave phases.

We also investigate systems in one spatial dimension where mechanisms similar to the ones in higher dimensions can be studied on larger clusters. However, there are some significant dimension dependent differences, e.g. in contrast to the two-dimensional case, one-dimensional antiferromagnets exhibit a gapped spectrum if the participating spins have integer value. We discuss the physics of these ‘Haldane’ chains. The calculated spectra for these materials are in excellent agreement with recent Neutron Scattering Experiments.

The effect of random exchange interaction in quantum antiferromagnets is also discussed. We show that such interactions do not necessarily induce an exponential decay in the spin correlations. Also, we argue that random exchange interactions can be induced by phononic disorder and might be responsible for the lineshape of Raman spectra observed in the cuprates. Our calculated Raman spectra are in good agreement with recent experiments on various cuprate precursors.

THE FLORIDA STATE UNIVERSITY
COLLEGE OF ARTS AND SCIENCES

DYNAMICAL PROPERTIES OF STRONGLY CORRELATED
FERMIONIC SYSTEMS

By
STEPHAN W. HAAS

A dissertation submitted to the
Department of Physics
in partial fulfillment of the
requirements for the degree of
Doctor of Philosophy

Degree Awarded:
Summer Semester, 1995

CONTENTS

List of Tables	viii
List of Figures	ix
Abstract	xii
1 Introduction	1
1.1 Strongly Correlated Electrons in Magnets and High-Temperature Superconductors	4
1.1.1 $\text{La}_{2-x}\text{Sr}_x\text{CuO}_4$	7
1.1.2 $\text{YBa}_2\text{Cu}_3\text{O}_{6+x}$	10
1.1.3 $\text{Ni}(\text{C}_2\text{H}_8\text{N}_2)_2\text{NO}_2\text{ClO}_4$	13
1.2 Electronic Models : Microscopic Foundation of Generic Hamiltonians	15
1.2.1 The Three-Band Hubbard Model	15
1.2.2 One-Band Models	19
1.3 Conclusions	23
2 The Lanczos Method	25
2.1 Introduction	25
2.2 Setting Up the Basis	28
2.3 Calculating the Matrix Elements	41
2.4 The Lanczos Procedure	53

2.5	Calculating Expectation Values	63
2.6	Dynamical Properties	68
2.7	Conclusions	84
3	Antiferromagnetically Induced Photoemission Band in the Cuprates	86
3.1	Magnetic Correlations in High- T_c Compounds	86
3.2	$A(p, \omega)$ for the Hubbard Model	88
3.3	$A(p, \omega)$ for the t-J Model	93
3.4	Conclusions	96
4	Quasiparticle Dispersion of One-Band Electronic Models	98
4.1	Introduction	98
4.2	Photoemission Spectra in the t-J and Hubbard Models at Half-Filling	100
4.3	Photoemission Spectra in the t-J Model away from Half-Filling	104
4.4	Conclusions	107
5	On the Fermi Surface of Strongly Correlated Electronic Models	109
5.1	Introduction	109
5.2	Momentum Distribution Function in 1D	111
5.3	Momentum Distribution Function in 2D	116
5.4	Conclusions	120
6	Influence of Long-Range Interactions on Superconductivity and Phase Separation	122
6.1	Introduction	122

6.2	The t - J - $1/r$ Model in 1D	123
6.3	The t - J - $1/r$ Model in 2D	126
6.4	Conclusions	127
7	Dynamical Properties of Antiferromagnetic Heisenberg Spin Chains	128
7.1	Introduction	128
7.2	Spin Dynamics on the Heisenberg Chain	130
7.2.1	Spin-1 AHC	132
7.2.2	Spin- $1/2$ AHC	136
7.3	Conclusions	140
8	Random Exchange Disorder in the Spin-$1/2$ XXZ Chain	142
8.1	Introduction	142
8.2	The Heisenberg Chain in the Presence of a Random Exchange Potential	143
8.3	Diagonalization and Quenched Averaging	144
8.4	Phase Diagram of the Spin- $1/2$ Heisenberg Chain in the Presence of Disorder in the Exchange Integral	148
8.5	Conclusions	153
9	Magnetic Raman Scattering in Two-Dimensional Spin-$1/2$ Heisenberg Antiferromagnets: Spectral Shape Anomaly and Magnetostriuctive Effects	154
9.1	Introduction	155
9.2	Raman Lineshape without Phonon-Magnon Coupling	157
9.3	Lineshape Anomaly	160

9.4	Magnetostriction	162
9.5	Superexchange-Phonon Coupling	162
9.6	A_{1g} and B_{2g} Symmetries	163
9.7	Conclusions	164
10	Conclusions	165
	Appendices	171
A	Strong Coupling Expansion of the Hubbard Model	172
A.1	Derivation of the Effective Hamiltonian	173
A.2	t-J Model	177
B	Diagonalization of a 4-Site Cluster	188
	Bibliography	193
	Biographical Sketch	204

LIST OF TABLES

1.1	Superconducting transition temperature for various compounds . . .	6
1.2	Parameters entering the three-band Hubbard Hamiltonian	20
2.1	Table for the logical operations ‘and’ and ‘or’	32
2.2	Spin correlation functions and their Fourier transforms	83

LIST OF FIGURES

1.1	Phase diagram for an electron-doped and a hole-doped high- T_c superconductor	2
1.2	Crystal structure of $\text{La}_{2-x}\text{Sr}_x\text{CuO}_4$	8
1.3	Phase diagram of $\text{La}_{2-x}\text{Sr}_x\text{CuO}_4$	10
1.4	Crystal structure of $\text{YBa}_2\text{Cu}_3\text{O}_{6+x}$	11
1.5	Crystal structure of $\text{Ni}(\text{C}_2\text{H}_8\text{N}_2)_2\text{NO}_2\text{ClO}_4$	13
1.6	Level splitting between Cu^{2+} and O^{2-} ions.	16
1.7	Schematic effect of doping for a charge-transfer CuO_2 plane	19
1.8	Schematic band structure of the CuO_2 planes	22
2.1	Construction of a tilted square cluster	27
2.2	Shapes of some tilted 2D clusters used in the Lanczos literature.	28
2.3	Symmetry operation on a tilted 8-site square cluster	38
2.4	Labeling of sites and bonds on a periodic tilted cluster	43
2.5	Schematic matrix representation for a Hamiltonian	44
2.6	Schematic representation of a Lanczos iteration step	61
2.7	Spin correlation functions for the 16-site spin-1/2 Heisenberg chain	82
3.1	Antiferromagnetically induced photoemission signal in Bi2212	89
3.2	Photoemission spectra in the 2D Hubbard model at various doping levels	91

3.3	Spin-spin correlations in one-band electronic models	93
3.4	Photoemission spectra in the 2D t-J model at various doping levels .	94
3.5	High-energy structure in the PES spectra of the 2D t-J model	96
4.1	Photoemission spectra in the 2D t-J model at half-filling	101
4.2	Photoemission spectra in the 2D Hubbard model at half-filling	103
4.3	Photoemission spectra in the 2D t-J model with 2 holes	104
4.4	Photoemission spectra in the 2D t-J model with 4 holes	106
4.5	Photoemission spectra in the 2D t-J model with 8holes	107
5.1	Schematic plot of the Fermi surface in strongly correlated electronic systems at low hole-doping	111
5.2	Phase diagram of the 1D t-J model	113
5.3	Momentum distribution functions in the 1D t-J model	114
5.4	Momentum distribution functions in the 1D and 2D Hubbard model .	115
5.5	Phase diagram of the 2D t-J model	117
5.6	Momentum distribution functions in the 2D t-J model	119
6.1	Phase diagram of the 1D t-J model with long-range $1/r$ interactions. .	124
6.2	CDW and SC susceptibilities in the 1D t-J- $1/r$ model	125
6.3	Phase diagram of the 2D t-J model with long-range $1/r$ interactions. .	127
7.1	Dispersion curve for a spin-1 Antiferromagnetic Heisenberg Chain . .	133
7.2	Dynamical spectrum of the spin-1 AHC	134
7.3	Dispersion curve for the spin-1/2 Antiferromagnetic Heisenberg Chain	137

7.4	Schematic plot of a spinon pair propagating on top of an antiferromagnetic background	138
7.5	Dynamical spectrum of the spin-1/2 chain	139
8.1	Double-logarithmic plot of real-space spin-spin correlations	145
8.2	Exponents of the power-law decay $ \omega^z(l) = Al^{-\eta_z}$ as a function of the disorder parameter	147
8.3	Ground state energy and antiferromagnetic structure factor of the 14-site spin-1/2 XXZ chain as a function of the disorder parameter	150
8.4	Phase diagram of the spin-1/2 XXZ chain in the presence of a random exchange potential	152
9.1	Phases associated with the Raman scattering channels	158
9.2	Raman cross section for the 2D spin-1/2 Heisenberg model	159
A.1	Hopping processes in the extended t-J model	187

ABSTRACT

The Exact Diagonalization method is a powerful numerical tool to study Quantum Many Body systems on finite clusters. In particular, using this technique one can accurately calculate energy and momentum dependent dynamic correlation functions which are observable in scattering experiments, such as Neutron Scattering, Raman Scattering, and Photoemission Spectroscopy which measures the spectral function of the system. Here we give an outline of the Lanczos method with special emphasis on the evaluation of dynamical quantities.

In this thesis, we apply this method to two-dimensional models of strongly correlated electrons which are believed to describe the physics of the recently discovered cuprate high- T_c compounds. We show that simple models of strongly correlated electrons, such as the Hubbard and the t-J model, can account for some normal state properties of these materials. In particular, the occurrence of photoemission bands which are introduced by short-range antiferromagnetic correlations is discussed.

The precursor materials of the cuprate superconductors are antiferromagnets. Here, we address the properties of antiferromagnets as they evolve from an insulating to a metallic phase upon doping. We focus on the shape of the Fermi surface at small hole doping and on the influence of long-range Coulomb interactions on the occurrence of superconducting and charge density wave phases.

We also investigate systems in one spatial dimension where mechanisms similar to the ones in higher dimensions can be studied on larger clusters. However, there

are some significant dimension dependent differences, e.g. in contrast to the two-dimensional case, one-dimensional antiferromagnets exhibit a gapped spectrum if the participating spins have integer value. We discuss the physics of these ‘Haldane’ chains. The calculated spectra for these materials are in excellent agreement with recent Neutron Scattering Experiments.

The effect of random exchange interaction in quantum antiferromagnets is also discussed. We show that such interactions do not necessarily induce an exponential decay in the spin correlations. Also, we argue that random exchange interactions can be induced by phononic disorder and might be responsible for the lineshape of Raman spectra observed in the cuprates. Our calculated Raman spectra are in good agreement with recent experiments on various cuprate precursors.

CHAPTER 1

INTRODUCTION

In 1986, the discovery of a new class of perovskite materials which undergo a superconducting phase transition at a temperature around 30K initiated a renewed effort to understand the physics of strongly correlated electronic systems.[1] Since the generation of the first compound $\text{La}_{2-x}\text{Ba}_x\text{CuO}_4$ (where 'x' indicates the variable number of Ba dopants replacing La), many similar materials have been synthesized.[2] The compound $\text{HgBa}_2\text{Ca}_2\text{Cu}_3\text{O}_{8+\delta}$ has the currently known highest *critical temperature*, T_c , of about 133K. Since the critical temperature below which these materials become superconducting is between one and two orders of magnitude larger than for previously known superconductors (e.g. Pb), they are commonly referred to as *high- T_c superconductors*. There has been much progress in characterizing the thermodynamic behavior (i.e. magnetic susceptibility and heat capacity) and some of the microscopic properties (i.e. using Neutron Scattering and Photoemission spectroscopy) of these compounds.[3] However, there has not been much general agreement on the microscopic mechanisms which ultimately lead to the formation of a superconducting condensate in these compounds.

Contrary to previously known superconductors, the high- T_c superconductors show strong magnetic correlations throughout their phase diagram.[4] The presence of magnetic instabilities is indicative of strong Coulomb interactions between the

conduction-band electrons. A generic phase diagram for these materials is shown in Fig. (1.1).[5]

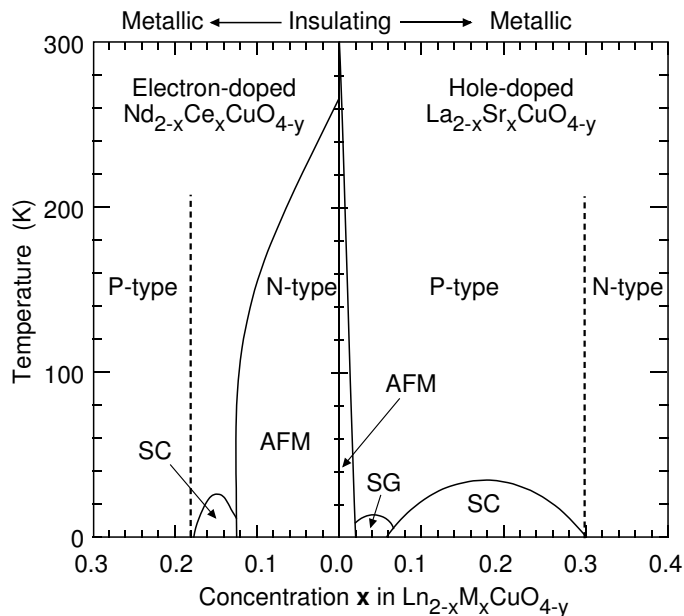


Figure 1.1: Phase diagram for an electron-doped and a hole-doped high- T_c superconductor.[5] Antiferromagnetic (AFM), superconducting (SC), and spin-glass (SG) phases are shown. The areas marked “p-type” (+) and “n-type” (-) correspond to positive and negative charge carriers in the material as determined by Hall measurements.

There are two kinds of cuprate compounds which are commonly distinguished with regard to what kind of charge carriers they can be doped with, namely electrons (i.e. $\text{Nd}_{2-x}\text{Ce}_x\text{CuO}_{4-y}$) or holes (i.e. $\text{La}_{2-x}\text{Sr}_x\text{CuO}_4$). The undoped parent compounds are in an antiferromagnetically ordered phase. Upon introduction of charge carriers into the system the long-range antiferromagnetism is destroyed, e.g. typically the magnetically ordered phase vanishes beyond a hole-doping level of $\delta_h \approx 2\%$. For electron-doped materials, the antiferromagnetic phase typically persists a little further up to electron-doping levels of $\delta_e \approx 12\%$. However, short-range antiferromagnetic fluctuations persist much further into the phase diagram as will

be discussed below. A possible explanation for the asymmetry of the antiferromagnetic phases in Fig. 1.1 is that in the hole-doped materials the dopant- holes go onto the oxygen atoms, while in the electron-doped materials dopant-electrons tend to occupy the copper sites (as will be discussed below in detail). It seems that the non-magnetic regions in the material created by hole-doping are more extended than for electron-doping, leading to an earlier break-down of the magnetically ordered phase.

Between $\delta_h \approx 5\% - 30\%$ there exists a superconducting phase with a maximum critical temperature around $x \approx 0.15$ (optimal doping) in $\text{La}_{2-x}\text{Sr}_x\text{CuO}_4$. Similarly, there is an optimum doping of $\delta_e \approx 15\%$ ($x=0.15$) for $\text{Nd}_{2-x}\text{Ce}_x\text{CuO}_{4-y}$. Both in the hole and electron-doped phase diagrams, superconductivity occupies a relatively small region compared to antiferromagnetism, and thus in theoretical studies it may become important to isolate the proper energy scales of the pairing mechanism responsible for superconductivity from those causing the bulk magnetic properties. (In $\text{La}_{2-x}\text{Sr}_x\text{CuO}_4$ an additional spin-glass phase around $\delta_h \approx 4\%$ has been reported, which extends over a very small region in the phase diagram.)

One of the most challenging problems posed by this new class of materials is that because of their inherent strong electronic correlations it is not obvious that Landau Fermi Liquid theory - which has been very successful in the context of metals - is applicable here.[6] Fermi Liquid Theory makes predictions about thermodynamic observables and transport properties which cannot be reconciled with experiments on the high- T_c compounds. Most significantly, a *linear* temperature dependence of the normal state resistivity (in the vicinity of optimal doping) has been established to be a universal property of these materials, while Fermi Liquid Theory predicts $\rho \propto T^2$. This observation is also very different from $\rho \propto a + bT^5$, which is valid for

conventional superconductors and can be understood in terms of electron-phonon scattering. Another puzzling experimental fact is that the Hall angle seems to depend quadratically on temperature, i.e. $\frac{\sigma_{xx}}{\sigma_{xy}} \propto T^2$. [7]

In our studies, we will mainly be concerned with the dynamical properties of materials whose physics is believed to be dominated by strongly correlated electrons such as quantum magnets and superconductors in their normal state. For this purpose, we study model Hamiltonians which are believed to capture the essential physics of these systems. In the second part of this chapter, we discuss the microscopic origin of these models. Typically, many degrees of freedom have to be integrated out of the original problem to make it accessible to present day computer capacities. The strongest common feature of all high- T_c compounds is the presence of CuO_2 planes. Thus, most models address solely these planes. However, inter-plane interactions might be important in the formation of hole pairs and are subject of much attention recently.

1.1 Strongly Correlated Electrons in Magnets and High-Temperature Superconductors

In this section, we discuss the chemical structure of some quasi two-dimensional cuprate superconductors and of a quasi one-dimensional spin-1 antiferromagnet. Here, the dimensionality assigned to the materials corresponds to strong anisotropies, e.g. the dominant exchange integral in the cuprates is found to lie in 2D CuO_2 sheets common to all high- T_c compounds, while the out-of-plane exchange constant is believed to be several orders of magnitude smaller. Similarly, the exchange integrals for the spin-1 antiferromagnet NENP are highly anisotropic,

i.e. they are negligible in all but one direction. Anisotropies of the magnitude found in the cuprates are not present in conventional superconductors such as Nb or Pb.

It is remarkable that all high- T_c compounds apparently have two features in common :

- The dominant physical processes (charge transport, antiferromagnetic exchange ...) that participate in the formation of the superconducting condensate are believed to be confined to the CuO_2 planes, while the out-of-plane atoms (e.g. Ba, O, La, ...) serve only as charge reservoirs. Upon doping the insulating parent compounds, the out-of-plane atoms provide charge carriers to the CuO_2 planes. However, some researchers believe that out-of-plane optical phonon modes are also important for the occurrence of superconductivity.
- In their undoped regime, the cuprates develop long-range antiferromagnetic order. Upon doping, this order is rapidly destroyed. However, even without strict long-range order, the spin correlation length can be large in the normal and superconducting phases producing a local arrangement of magnetic moments that at short distances differs very little from that observed below the Néel temperature in the insulating regime.

There also seems to be a correlation between the number of neighboring CuO_2 planes and the optimal value for the critical temperature, e.g. $\text{Tl}_2\text{Ca}_2\text{Ba}_2\text{Cu}_3\text{O}_{10}$ which has a large T_c of 125K, has three adjacent CuO_2 planes, while $\text{La}_{1.85}\text{Sr}_{0.15}\text{CuO}_4$ with only one CuO_2 layer has a T_c of 39K. Also, although there is only little variation among the cuprates with regard to the Cu-O bond length (within the planes), there

Material	$T_c(K)$
$\text{HgBa}_2\text{Ca}_2\text{Cu}_3\text{O}_{8+\delta}$	133
$\text{Tl}_2\text{Ca}_2\text{Ba}_2\text{Cu}_3\text{O}_{10}$	125
$\text{YBa}_2\text{Cu}_3\text{O}_7$	92
$\text{Bi}_2\text{Sr}_2\text{CaCu}_2\text{O}_8$	89
$\text{La}_{1.85}\text{Sr}_{0.15}\text{CuO}_4$	39
$\text{Nd}_{1.85}\text{Ce}_{0.15}\text{CuO}_4$	24
$\text{RbCs}_2\text{C}_{60}$	33
Nb_3Ge	23.2
Nb	9.25
Pb	7.20
UPt_3	0.54

Table 1.1: Superconducting transition temperature for various compounds.[3]

is evidence that those compounds with a bond length slightly shorter than the typical 1.9\AA have an increased T_c . [8]

In their insulating phase, the cuprates (in particular $\text{La}_{1.85}\text{Sr}_{0.15}\text{CuO}_4$) are an almost ideal realization of the 2D Heisenberg antiferromagnet.[9] In the early days of high- T_c research, this phase was subject to much discussion. After some effort, it was established that the 2D Heisenberg model,

$$H = J_{\parallel} \sum_{\langle i,j \rangle} \mathbf{S}_i \cdot \mathbf{S}_j, \quad (1.1)$$

has gapless magnon excitations, and the quantum fluctuations associated with these excitations are not strong enough to destroy long-range antiferromagnetic order at $T=0$ in 2D.

The fact that antiferromagnetic order persists in the cuprates for finite temperatures and small dopings can be understood in terms of the weak inter-plane coupling J_{\perp} . An estimated $J_{\perp} \approx 10^{-5} J_{\parallel}$ is sufficient to establish the magnetically ordered phase observed in the cuprates.[10]

A large number of compounds with the characteristic CuO_2 planes have been synthesized. This is not too surprising since it is possible to modify the number of planes per unit cell, the atoms separating the nearby planes, as well as the structure, composition, and size of the charge reservoir, producing a huge number of combinations. In the table above, taken from E. Dagotto's recent review article,[3] we present a very short list of the most widely studied compounds in this field, with their critical temperatures T_c . For comparison we also show the critical temperature of some conventional superconductors like Nb, Pb, and Nb_3Ge . The latter had the highest critical temperature known before 1986. The T_c 's of a superconducting heavy fermion material (UPt_3) and a fullerene are also given.

In the remainder of this section, we discuss the structure and phase diagram of some particular high- T_c compounds in more detail.

1.1.1 $\text{La}_{2-x}\text{Sr}_x\text{CuO}_4$

$\text{La}_{2-x}\text{Sr}_x\text{CuO}_4$ is one of the earliest high- T_c materials. In our notation, 'x' controls the doping level when some of the La-ions in the parent compound La_2CuO_4 are randomly replaced by 'x' Sr-ions per unit cell. The structure of this material is

shown in Fig. 1.2. At intermediate doping levels, $\text{La}_{2-x}\text{Sr}_x\text{CuO}_4$ crystallizes into the body centered tetragonal lattice shown in this picture. However, at lower Sr concentrations there is a minor structural rearrangement which renders an orthorhombic distortion. This change in the lattice geometry is usually neglected in calculations, but it might become important in the discussion of the symmetry of the superconducting order parameter.

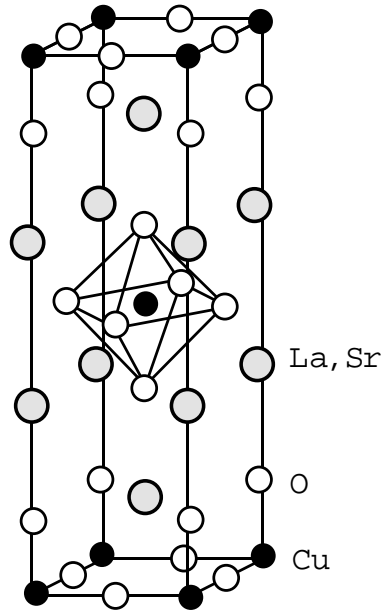


Figure 1.2: Crystal structure of $\text{La}_{2-x}\text{Sr}_x\text{CuO}_4$. [5]

The atomic configurations of the elements which go into this material are given by : Cu : $[\text{Ar}](3d)^{10}(4s)$, La : $[\text{Xe}](5d)(6s)^2$, O : $[\text{He}](2s)^2(2p)^4$, and Sr : $[\text{Kr}](5s)^2$. As can be seen from Fig. 1.2, the CuO_2 planes are separated by two sheets of LaO which serve as a charge reservoir for the planes as we will discuss below. The distance between the CuO_2 planes is 6.6\AA , and the distance between the LaO sheets and the closest CuO_2 plane is 2.4\AA . Within the CuO_2 planes, the distance between the Cu and the O is 1.9\AA . As can be seen from the CuO_2 plane in the center of Fig.

1.2, there are also ‘apical’ oxygens centered 2.4\AA above the Cu in the planes. Thus each copper ion is surrounded by an octahedron of oxygen ions.

In the crystal it becomes important what ionization state the elements are in. In the parent compound (La_2CuO_4), Lanthanum is in the closed shell [Xe] configuration, e.g. it loses two s-electrons and one d-electron to become La^{3+} . The oxygens gain two additional s-electrons and are thus in the O^{2-} ionization state. Then, the copper ions have to be in the Cu^{2+} state to guaranty charge neutrality. Hence, the copper loses its outer 4s-electron and one of the d^{10} -electrons. Since there are now only 9 of the 10 levels in the copper 3d-shell filled, there is a net spin-1/2 per copper ion. These spin-1/2 holes can super-exchange between the copper ions via the electron-filled p-shells of the oxygen ions. This mechanism gives rise to the antiferromagnetic order which is observed in the cuprate parent compounds. It has been shown that the parent compounds are well described by a 2D Heisenberg model with nearest neighbor interactions, [9] e.g. Eq. 1.1 with $J_{\parallel} \approx 1450K$. The small residual interactions between the CuO_2 planes ($J_{\perp} \approx 10^{-5}J_{\parallel}$) lead to a finite Néel temperature of about $300K$ (see Fig. 1.3).

Upon doping, the La^{3+} ion is replaced by Sr^{2+} , Sr^{2+} being in the [Kr] configuration. It is believed that the Sr dopants enter the material in a random manner. Since Sr^{2+} has one less hole than La^{3+} , it pulls one electron out of the CuO_2 plane. It turns out that the least bound electrons in the CuO_2 planes are in the oxygen p-shell. Thus, effectively doping by Sr leads to a change of the ionization state of the oxygens in the planes from O^{2-} to O^{-} . As explained before, the antiferromagnetic long-range order is destroyed rapidly by introducing holes into the planes, and the system becomes metallic. For Sr-dopings between $x \sim 0.05$ and ~ 0.30 , a supercon-

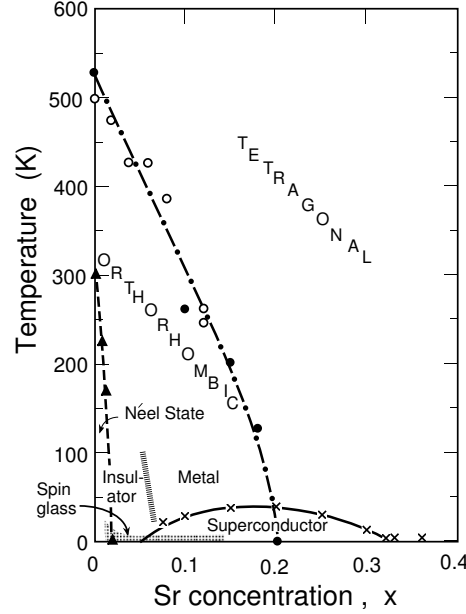


Figure 1.3: Phase diagram of $\text{La}_{2-x}\text{Sr}_x\text{CuO}_4$. [11]

ducting phase is found at low temperatures. The maximum value of T_c is observed at the “optimal” doping $x \simeq 0.15$.

1.1.2 $\text{YBa}_2\text{Cu}_3\text{O}_{6+x}$

Let us now discuss another high- T_c material which has a structure more complicated than $\text{La}_{2-x}\text{Sr}_x\text{CuO}_4$ because it has *two* adjacent CuO_2 planes per unit cell. [12] As mentioned above, there is a tendency in the cuprates that the maximum T_c increases monotonically with the number of adjacent $\text{Cu}-\text{O}$ sheets per unit cell. Indeed, $\text{YBa}_2\text{Cu}_3\text{O}_{6+x}$ has a critical temperature of 92 K which is more than twice as high as the T_c for $\text{La}_{2-x}\text{Sr}_x\text{CuO}_4$. A picture of the crystal structure for this compound is shown in Fig. 1.4. The neighboring CuO_2 planes are 3.2\AA apart, while the $\text{Cu}-\text{O}$ bonds in the planes are still 1.9\AA long. Between the adjacent CuO_2 planes there is an Y-ion which is believed not to affect the physical properties of the CuO_2

planes in any crucial way. However, the Y-ion might have the tendency to influence holes in the planes via trapping Coulomb centers.

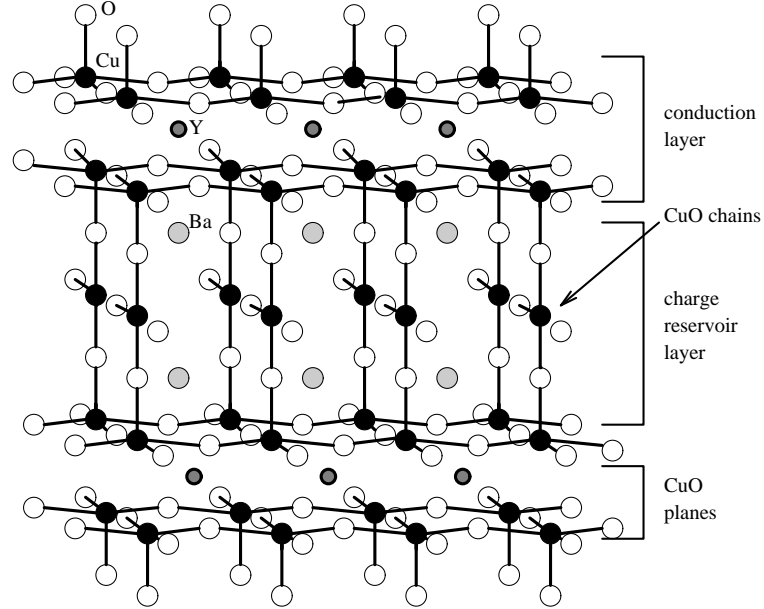


Figure 1.4: Crystal structure of $\text{YBa}_2\text{Cu}_3\text{O}_{6+x}$. [13]

Each pair of neighboring CuO_2 planes in this compound is separated by a charge reservoir containing barium, oxygen and copper atoms. An additional complication in the structure of $\text{YBa}_2\text{Cu}_3\text{O}_{6+x}$ is introduced by the presence of Cu-O chains parallel to the planes. However, as we will discuss below, the coppers on the chains are in a different ionization state than the ones in the planes. Thus, most magnetic and transport properties are not dramatically affected by the Cu-O chains. However, some quantities like the optical conductivity are believed to be affected by the chains.

The atomic configurations of the elements which go into this material are given by : Cu : $[\text{Ar}](3d)^{10}(4s)$, Ba : $[\text{Xe}](6s)^2$, O : $[\text{He}](2s)^2(2p)^4$, and Y : $[\text{Kr}](5s)^2(4d)$. In the crystal, the yttriums lose 2 s-electrons and one d-electron and are thus in the Y^{3+} state. Similarly, the bariums are in Ba^{2+} , and the oxygens are in the O^{2-} state.

However, there is a difference between the ionization state of the copper atoms in the CuO_2 planes and those in the charge reservoir (which includes the Cu-O chains): in the planes the coppers are in the Cu^{2+} state as in $\text{La}_{2-x}\text{Sr}_x\text{CuO}_4$, and hence they have a magnetic moment ($S=1/2$) which leads to antiferromagnetism within the planes with a Néel temperature of about 500K . (Again, a small inter-plane coupling J_\perp is responsible for the finite Néel temperature.) However, the coppers in the charge reservoir are in the Cu^{3+} state, and thus have no net magnetic moment.

$\text{YBa}_2\text{Cu}_3\text{O}_{6+x}$ can be doped by adding oxygens to the magnetically ordered parent compound ($x=0$). The dopant oxygens are believed to become part of the charge reservoir having an ionization state of O^{2-} . Then, two electrons per dopant oxygen are removed out of the planes, and hence oxygen doping is equivalent to introducing holes into the planes. Antiferromagnetic order disappears at a doping level of about $x \approx 0.3$, and a superconducting phase starts to develop immediately thereafter. The optimal doping level with the highest T_c for this compound is reached at $x \approx 0.92$.

Recently, there has been a considerable effort in synthesizing materials with multiple adjacent CuO_2 layers, since apparently inter-layer coupling increases the maximum T_c . To this day, the highest confirmed critical temperature has been seen in the 3-layer mercury compound $\text{HgBa}_2\text{Ca}_2\text{Cu}_3\text{O}_{8+\delta}$. Another experimental thumb-rule to increase T_c for a given material is to apply pressure in order to bring the CuO_2 layers closer together. In particular, by introducing additional ions with a large radius into the charge reservoir (i.e. "applying chemical pressure") T_c can be increased. However, there are natural limits to this procedure given by the stoichiometry and the stability of the crystal configuration.

1.1.3 $\text{Ni}(\text{C}_2\text{H}_8\text{N}_2)_2\text{NO}_2\text{ClO}_4$

In contrast to the cuprate materials discussed in the previous sections, the one-dimensional molecular based compound $\text{Ni}(\text{C}_2\text{H}_8\text{N}_2)_2\text{NO}_2\text{ClO}_4$ (NENP), shown in Fig. 1.5, consists of $[\text{Ni}(\text{C}_2\text{H}_8\text{N}_2)]^{2+}$ moieties bridged by $[\text{NO}_2]^-$ ions. There are also $[\text{ClO}_4]^-$ ions present which provide charge neutrality for the crystal. There has been much interest in this compound and related materials because it exhibits short-range antiferromagnetic order with a correlation length of roughly six times the distance between Ni-ions ($= 8.295\text{\AA}$)[14] and a gap (of about 1.82 meV) at the bottom of its spectrum, called the *Haldane gap*.

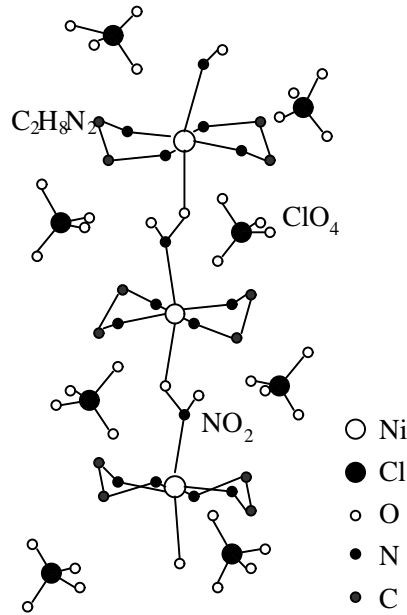


Figure 1.5: Crystal structure of $\text{Ni}(\text{C}_2\text{H}_8\text{N}_2)_2\text{NO}_2\text{ClO}_4$. [15]

NENP crystallizes into an orthorhombic structure. In the solid, the Ni atom ($\text{Ni} : [\text{Ar}](3d)^8(4s)^2$) shares its two outer 4s-electrons with the $[\text{ClO}_4]^-$ and the $[\text{NO}_2]^-$. In particular, the Ni^{2+} ion forms a coordination bond with $[\text{NO}_2]^-$. Ni^{2+} is in a $3d^8$ configuration, and Hund's rules provide that the two magnetic orbitals

(e.g. $d_{x^2-y^2}$ and $d_{3z^2-r^2}$) are occupied by electrons of the same spin orientation (like in the cuprates, the degeneracy among the 3d-orbitals is removed by crystal fields). Hence, the Ni^{2+} ion has a net spin $S=1$, and is in a A_2 triplet configuration.[16] The superexchange between two neighboring Ni^{2+} ions takes place via the highest occupied molecular orbital of $[\text{NO}_2]^-$, e.g. via the antibonding π^* -orbital.[17] In the next section, we will address the issue of super-exchange in more detail.

As we show in a later chapter, NENP can be well described by a Heisenberg antiferromagnet in the presence of single-ion anisotropy (which is typically an order of magnitude smaller than the exchange integral) and an in-plane anisotropy (which is typically two orders of magnitude smaller than the exchange integral). Hence, the Hamiltonian for this system can be written as

$$H = J \sum_i \mathbf{S}_i \cdot \mathbf{S}_{i+1} + D \sum_i (S_i^z)^2 + E \sum_i [(S_i^x)^2 - (S_i^y)^2], \quad (1.2)$$

where $J \approx 50\text{K}$, $D \approx 10\text{K}$, and $E \approx 1\text{K}$ can be determined by fitting Neutron scattering data to theoretically calculated spectra for this model. Both anisotropies which enter Eq. 1.2 are effects of a spin-orbit coupling $\lambda \mathbf{S} \cdot \mathbf{L}$, which enters the Hamiltonian to lowest non-vanishing order in perturbation theory as $\lambda^2 \Lambda_{\mu\nu} \mathbf{S}^\mu \mathbf{S}^\nu$. The degenerate orbital momentum levels of individual atoms in the solid (here $l=2$) are split by crystal field effects, where the anisotropy tensor is given by $\Lambda_{\mu\nu} = \sum_{\Gamma\gamma} \frac{\langle \Gamma\gamma | L_\mu | \Gamma'\gamma' \rangle \langle \Gamma'\gamma' | L_\nu | \Gamma\gamma \rangle}{(E_{\Gamma'\gamma'} - E_{\Gamma\gamma})}$, with Γ labelling the irreducible representation of the crystal point-group. [16]

There is also a finite but small inter-chain coupling $J'/J \approx 10^{-4}$ which potentially could give rise to 3D magnetic ordering as observed in the spin-1 compound CsNiCl_3 which has $J'/J \approx 10^{-2}$ and 3D long-range order below a Néel temperature of 4.85K.

However, for NENP the ratio J'/J is two orders of magnitude smaller, and thus no 3D-1D (order-disorder) transition has been observed down to 1.2 K.

Finally, let us address the question why the exchange constant in NENP is two orders of magnitudes smaller than for the cuprates. The lattice constants of NENP are given by $a=15.223\text{\AA}$, $b=10.3\text{\AA}$ and $c=8.295\text{\AA}$ where the c -axis is along the Ni^{2+} ions as shown in Fig. 1.5. Thus the distance $\text{Ni-NO}_2\text{-Ni}$ in this compound is about twice as large as the Cu-O-Cu bond in the cuprates. The exchange integral J depends strongly on the bond-length between the ions which participate in the super-exchange, e.g. by applying mechanical pressure to NiO a dependence of $J(r) \propto r^{-10}$ has been found.[18] Hence a reduction in the overlap of the orbitals participating in the super-exchange process can account for a dramatic drop in the exchange constant and in the corresponding Néel temperature $T_N \propto J$.

1.2 Electronic Models : Microscopic Foundation of Generic Hamiltonians

1.2.1 The Three-Band Hubbard Model

Here we show how an effective Hamiltonian to describe the behavior of the electrons in the CuO_2 planes can be constructed. From now on, we will only consider a simplified generic 2D crystal square lattice, equivalent to the CuO_2 planes in Figs. 1.2 and 1.4. On such a square lattice, a unit cell contains one copper and two oxygen atoms. (Eventually, additional layers will have to be added to account for 3D effects in real materials.)

Let us first identify the relevant orbitals of the coppers and oxygens in the plane. In the undoped parent compound, the copper atom ($\text{Cu} : [\text{Ar}](3d)^{10}(4s)$), loses one

4s-electron and one of the 3d-electrons and is thus in a $3d^9$ state, while the oxygens ($O : [\text{He}](2s)^2(2p)^4$) gain two electrons (one being provided by the copper, the other one coming from the charge reservoir). Thus, all three 2p-orbitals of the oxygens are filled, and so are four of the five 3d-orbitals of the copper, while the $d_{x^2-y^2}$ Cu orbital has one electron and one hole. The degeneracy among the Cu 3d-orbitals and the O 2p-orbitals is removed by crystal fields present in the solid. Also, the copper and oxygen orbitals tend to hybridize.[19] Thus, we arrive at the levels shown in Fig. 1.6.

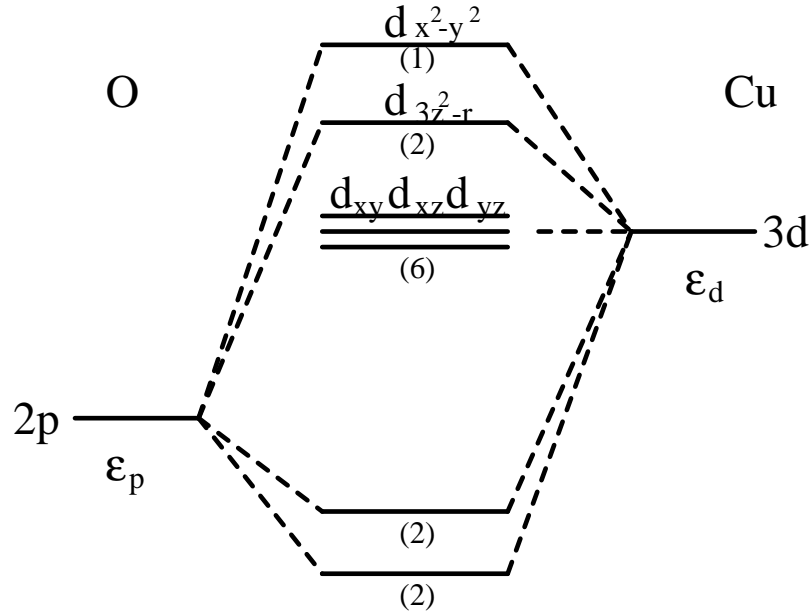


Figure 1.6: Level splitting between Cu^{2+} and O^{2-} ions. Only the 3d-electrons of Cu and the p_x and p_y orbitals of the oxygens are considered. The numbers in parentheses indicate the occupations of the different levels in the undoped compound.[19]

From this figure, we see that in the solid the band highest in energy evolves out of the Cu $d_{x^2-y^2}$ -orbital and one of the O $2p_\sigma$ -orbitals, sometimes referred to as the upper *antibonding band*. Since there is only one hole present in the parent compounds, it is now convenient to switch from “electron-terminology” to “hole-

terminology”, e.g. the ‘vacuum’ for the holes is given by completely electron-filled orbitals. Then, the lowest-energy state for the holes is the highest energy state for the electrons, i.e. the antibonding $d_{x^2-y^2}$ band, and the energy level scheme in Fig. 1.6 has to be read upside-down in the hole-picture.

Why are the cuprates not metallic as would be expected for a system whose lowest band is half-filled Γ Until now, we have neglected Coulomb repulsion between charge carriers. First, let us consider on-site repulsions (U_d and U_p for the Cu and the O respectively). If U_d exceeds the charge transfer gap $\Delta = \epsilon_p - \epsilon_d$, which is the difference in on-site energy levels for the copper (ϵ_d) and the oxygens (ϵ_p), the holes are bound to the Cu at half-filling, and the system is a *charge transfer insulator*.^[22] Indeed, it has been observed that the on-site repulsion on copper is about three times as large as the charge transfer gap in the cuprates. ^[21]

Now, when additional holes are brought into the CuO_2 , will they preferably sit on the Cu or the O atoms Γ Naively, one might think that the additional holes will go on the $d_{x^2-y^2}$ -orbital shown in Fig. 1.6. This would be equivalent to filling Fermi-levels in a non-interacting electron gas. However, as we have seen above, this system is *strongly interacting*, i.e. $U_d/\Delta \gg 1$. Thus, the dopant-holes prefer to go onto the highest O-level, since the Coulomb repulsion between holes strongly disfavors double-occupancy of the Cu $d_{x^2-y^2}$ -orbital. The state with one additional *ligand* hole on one of the oxygens surrounding the copper is often labeled $d^9\bar{L}$.

Based on these considerations, Emery proposed a three-band model which takes into account the on-site Coulomb repulsions in addition to the highest oxygen 2p-level and the Cu $d_{x^2-y^2}$ -orbital.^[20] The corresponding Hamiltonian - often referred

to as the *three-band Hubbard model* - can be written as

$$\begin{aligned}
H = & -t_{pd} \sum_{\langle ij \rangle} (p_j^\dagger d_i + h.c.) - t_{pp} \sum_{\langle jj' \rangle} (p_j^\dagger p_{j'} + h.c.) + \epsilon_d \sum_i n_i^d + \epsilon_p \sum_j n_j^p \\
& + U_d \sum_i n_{i\uparrow}^d n_{i\downarrow}^d + U_p \sum_j n_{j\uparrow}^p n_{j\downarrow}^p + U_{dp} \sum_{\langle ij \rangle} n_i^d n_j^p.
\end{aligned} \tag{1.3}$$

Here, p_j are fermionic operators that destroy holes at the oxygen ions labeled j , while d_i corresponds to annihilation operators at the copper ions at site i . $\langle ij \rangle$ refers to Cu-O nearest neighbor pairs of ions. The hopping terms correspond to the hybridization among nearest neighbors Cu and O atoms, and are roughly proportional to the overlap between orbitals. For completeness, a direct O-O hopping term with amplitude t_{pp} is also included. U_d and U_p are positive constants that represent the repulsion between holes when they are at the same d and p orbitals, respectively. U_{pd} has a similar meaning, i.e. it corresponds to the Coulomb repulsion when two holes occupy adjacent Cu – O ions. In principle, interactions at larger distances should also be included in the Hamiltonian, but they are presumed to be screened by the finite density of electrons.

From a band structure calculation the actual values of the parameters entering the Hamiltonian Eq. 1.3 can be estimated. They are given in table 1.2 showing that we are indeed in the strong coupling regime.[21]

The spin-1/2 holes which preferably sit on the coppers at half-filling, super-exchange with neighboring Cu-spins via the the upper antibonding band. Thus it is possible to describe the half-filled system by an effective 2D Heisenberg Hamiltonian which is a limit (i.e. $U_d/\Delta \gg 1$) of the more complicated multi-band Hamiltonian in Eq. 1.3. In a perturbative approach around the atomic limit, the exchange integral is given by $J = \frac{4t_{pd}^2}{(\Delta + U_{pd})^2} \left(\frac{1}{U_d} + \frac{2}{2\Delta + U_p} \right)$. [22] Similarly, in the 1D compound

NENP, the two spin-1/2 holes which couple into a spin-1 particle due to Hund's rules super-exchange via the highest electron-occupied molecular orbit, i.e. the antibonding π^* -orbital, of the NO_2^- .

Finally, we would like to mention that the considerations leading to the three-band Hubbard Hamiltonian apply to both types of cuprate superconductors, the hole-doped ("p-type") and the electron-doped ("n-type"). Hence, with the same reasoning when additional holes are brought into the system, it can be argued that dopant-electrons prefer to go onto the copper $d_{x^2-y^2}$ -orbital leading to a d^{10} configuration. The doping behavior of the three-band Hubbard model is summarized in Fig. 1.7. Note, that this figure is only schematic since in reality effects of hybridization deform the symmetric ionic bands shown here. [22]

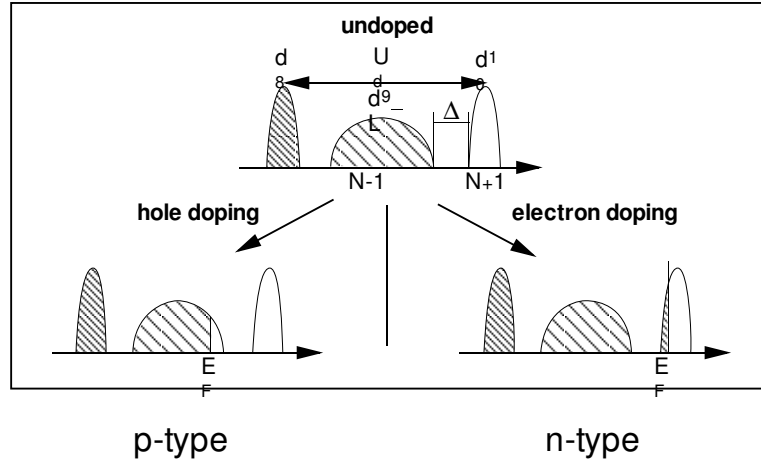


Figure 1.7: Schematic effect of doping for a charge-transfer CuO_2 plane. Hole doping moves the Fermi level into the charge-transfer band, while electron-doping moves it into the upper Hubbard band.[23]

1.2.2 One-Band Models

Unfortunately, the three-band Hubbard model is a system that is very difficult to study since it still contains many degrees of freedom, i.e. it has four states per site

$\epsilon_p - \epsilon_d$	t_{pd}	t_{pp}	U_d	U_p	U_{pd}
3.6eV	1.3eV	0.65eV	10.5eV	4eV	1.2eV

Table 1.2: Parameters entering the three-band Hubbard Hamiltonian.[21]

($|\uparrow\rangle$, $|\downarrow\rangle$, $|\uparrow\downarrow\rangle$, and $|0\rangle$). Thus, an N-site system contains 4^N states, which makes it impossible to study cluster containing more than three CuO_2 unit cells using exact diagonalization techniques, since the required Hilbert space exceeds present day computer capacities.

Also, the parameters entering the Hamiltonian (table 1.2) are of the order 1-10 eV, while the phenomena we want to address have energy scales around 0.125 eV (antiferromagnetism with $J \approx 1450$ K) and 0.009 eV (superconductivity below $T_c \approx 100\text{K}$). It thus becomes desirable to create an effective Hamiltonian, emerging as a strong-coupling limit from the more general three-band Hubbard model, with fewer degrees of freedom (e.g. fewer bands) and with energy scales that can address the antiferromagnetic and superconducting phases observed in the materials of interest.

Zhang and Rice brought forward the idea that the exchange interaction between a dopant-hole on the oxygen and the hole which is confined to the copper at half-filling is so strong that triplet excitations can be neglected.[24] Doping with holes then creates local “Zhang-Rice” singlet states which can be thought of as empty sites on a new lattice made only out of Cu atoms, i.e. in the new lattice the unit cell of the three-band Hubbard model containing 2 oxygens and one copper collapses into a single site. In general, the dopant-hole can be in a linear combination of all four oxygen 2p-orbitals surrounding a Cu spin-1/2 hole. Thus the Zhang-

Rice singlet is a spin-0 charge-2e object that extends over a CuO_4 cluster. By diagonalizing this cluster (and also the Cu_2O_6 cluster) Zhang and Rice showed that indeed there is a gap of ≈ 3.5 eV between the singlet and the closest triplet state. The d^{10} configuration, i.e. double-occupancy of the Cu $d_{x^2-y^2}$ -orbital, is not accessible to the Zhang-Rice singlet. Thus, when writing down an effective Hamiltonian - the *t-J Hamiltonian* - involving only spin-1/2 holes on the Cu and the CuO_4 -singlets centered around Cu sites (Zhang-Rice singlets), the upper Hubbard band corresponding to doubly occupied Cu $d_{x^2-y^2}$ -orbitals will no longer appear. Since the Zhang-Rice singlets are centered around the copper ions anyway, it is not necessary to have oxygen sites to be present in the effective Hamiltonian. Then, it can be shown that the three-band Hubbard model reduces to

$$H = J \sum_{\langle ij \rangle} (\mathbf{S}_i \cdot \mathbf{S}_j - \frac{1}{4} n_i n_j) - t \sum_{\langle ij \rangle \sigma} [c_{i\sigma}^\dagger (1 - n_{i-\sigma})(1 - n_{j-\sigma}) c_{j\sigma} + h.c.], \quad (1.4)$$

where \mathbf{S}_i are spin-1/2 operators at the sites i of a two dimensional square lattice, and J is the antiferromagnetic coupling between nearest neighbor sites $\langle ij \rangle$. The hopping term allows for the movement of spin-half particles, explicitly *excluding* double occupancy due to the presence of the projector operators $(1 - n_{i-\sigma})$. This model has only three possible states per site i.e. a spin-up $|\uparrow\rangle$ or spin-down $|\downarrow\rangle$, or the absence of a spin $|0\rangle$. At half-filling, the hopping term is not active, and the t -J model reduces to a simple Heisenberg model with an irrelevant off-set $-N/2$ for an N -site cluster.

In order to account for hopping between next-nearest neighbor sites, an additional kinetic term $(-t' \sum_{\langle ij \rangle \sigma} [c_{i\sigma}^\dagger (1 - n_{i-\sigma})(1 - n_{j-\sigma}) c_{j\sigma} + h.c.])$ is sometimes

added to Eq. 1.4. Then, by choosing the parameters $J = 0.128\text{eV}$, $t = 0.43\text{eV}$ and $t' = -0.07\text{eV}$ the low-energy spectrum of the hole-doped three-band Hubbard model (with parameters given in table 1.2) can be reproduced quite accurately.[21]

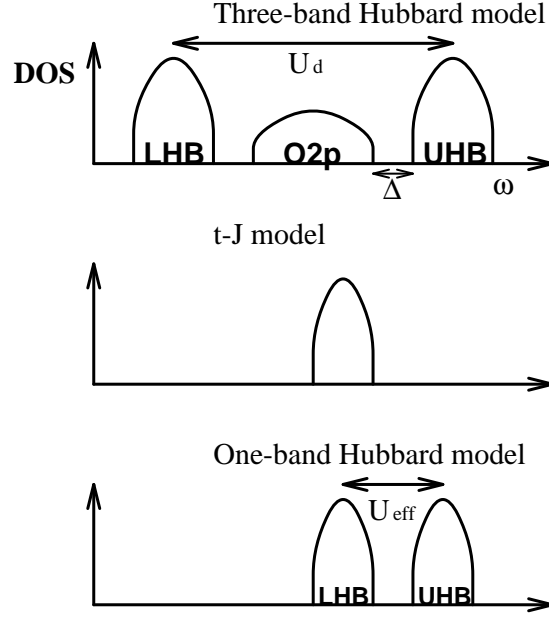


Figure 1.8: Schematic band structure of the CuO_2 planes. In the three-band Hubbard model, U_d is the Coulomb repulsion at the copper ions, and Δ is the difference in energy between the Cu $d_{x^2-y^2}$ -orbital and the O $2p$ -orbitals. In the t - J model, the upper Hubbard band (UHB) is neglected because the strong Coulomb on-site repulsion disfavors double-occupancy. Here, the only band present is formed out of the two lower bands of the three-band model. The one-band Hubbard model simulates the charge transfer gap using an effective U_{eff} between its lower (LHB) and upper (UHB) Hubbard band.

In addition to the $t - J$ and the three-band Hubbard model, theorists have extensively studied the more generic two-dimensional *one*-band Hubbard model.[25] This model can be written as

$$H = -t \sum_{\langle ij \rangle, \sigma} (c_{i\sigma}^\dagger c_{j\sigma} + c_{j\sigma}^\dagger c_{i\sigma}) + U \sum_i (n_{i\uparrow} - \frac{1}{2})(n_{i\downarrow} - \frac{1}{2}), \quad (1.5)$$

where $c_{i\sigma}^\dagger$ is a fermionic operator that creates an electron at site i of a square lattice with spin σ . U is the on-site repulsive interaction, and t the hopping amplitude.

Although we know that the cuprates present a band structure with three dominant bands (as shown in Fig. 1.8), the one-band Hubbard model tries to mimic the presence of the charge transfer gap Δ by means of an *effective* value of the Coulomb repulsion U_{eff} , and thus it presents only two Hubbard-bands. However, in contrast to the t-J Hamiltonian, the one-band Hubbard model is particle-hole symmetric, e.g. there is a symmetry between the upper and the lower Hubbard band which is not present in the t-J model (see Fig. 1.8).

In the strong coupling limit ($U/t \rightarrow \infty$), the one-band Hubbard model can be mapped into the t-J model with the addition of terms involving three sites as is shown in Appendix A.[19] However, close to half-filling the three-site terms are not expected to influence the physical behavior of the plain t-J model (Eq. 1.4) dramatically.

Similar to the t-J model, the low-energy spectrum of the one-band Hubbard model can be fitted quite well to that of the three-band Hubbard model by using the parameters $U = 5.4\text{eV}$, $t = 0.43\text{eV}$ and $t' = -0.07\text{eV}$, i.e. $U/t \sim 12$. [21]

1.3 Conclusions

Having set up Hamiltonians which are believed to contain the physics of anti-ferromagnets and high- T_c superconductors we are left with the formidable task of calculating measurable quantities to gain some understanding of experiments done on these materials. Unfortunately, there is no known perturbative technique that allows us to treat strongly correlated models like the ones discussed above in a controlled manner.

Then we rely heavily on numerical techniques such as Quantum Monte Carlo, high-temperature expansions and exact diagonalization. These methods are unbiased (i.e. in contrast to mean-field based approaches) since they do not make an initial assumption on the nature of the ground state of the system. However, each numerical method has its limitations. High-temperature expansions are usually confined to temperature regimes which are inaccessible to experiments. Quantum Monte Carlo simulations of fermionic systems suffer from the “sign-problem” which is severe in the presence of strong correlations. Finally, the Lanczos approach we are going to take is limited to relatively small cluster sizes, since the Hilbert space of the models under consideration typically grows exponentially with the system size.

In spite of their limitations, numerical studies already have provided us with insights into strongly correlated systems.[3] In particular, we have now a good understanding of the magnetically ordered phase in the cuprates close to half-filling, although no exact solutions exist for that regime. Also, there has been some progress in understanding the “anomalous” normal state properties of the cuprates around optimal doping, i.e. it can be argued on the basis of numerical studies that short-range antiferromagnetic correlations are responsible for the shape of the Fermi surface as it is observed in Photoemission experiments. In the following chapters we will elaborate on the implementation of the exact diagonalization method on strongly correlated fermionic systems described by the model Hamiltonians we have presented here.

CHAPTER 2

THE LANCZOS METHOD

2.1 Introduction

In this chapter, an algorithm is presented which allows us to determine numerically the ground state and some excited states for Hamiltonian operators on finite clusters. The basic idea of this ‘Lanczos method’ is that a special basis can be constructed where the Hamiltonian has a tridiagonal representation. [26] Once in this form the ground state of the matrix can be found easily using standard library subroutines.[27] It is standard terminology to call a matrix ‘exactly diagonalized’ when its ground state has been obtained using the Lanczos method. The algorithm presented here will be illustrated by considering the example of a spin-1/2 Heisenberg chain. However, the ideas brought forward are quite general, and apply to any Quantum Hamiltonian.

In the following section, it will be shown how to set up a basis in which the Hamiltonian operator can be represented. At this point it is also demonstrated how to incorporate translational, spin-inversion and other symmetries into the program. This is essential since the Hilbert space for a given cluster can be dramatically reduced once these symmetries are applied.

Subsequently the Hamiltonian matrix elements for the given basis are calculated. Special attention is given to efficient computer storage of these matrix elements, e.g.

by making use of the hermeticity of the Hamiltonian. Also, typically the matrix representation for a given operator is sparse, and thus a lot of memory can be saved by only storing the non-zero elements and their respective positions.

After the calculation of the matrix elements, the actual Lanczos step is discussed. Certain variations on the original Lanczos idea are presented. We will allude to a very educational modified Lanczos algorithm which might especially appeal to the beginning programmer.[28]

Once the ground state has been obtained the expectation value of various physical quantities can be easily evaluated. In particular, our algorithm allows the calculation of “off-diagonal” averages which are complicated to obtain using other numerical techniques such as Monte Carlo simulations.

Finally, one of the most appealing features of the Lanczos method is that it allows the calculation of *dynamical* properties of a given Hamiltonian. Here, we demonstrate how to evaluate spectral functions which are directly comparable to scattering experiments on related materials, such as Neutron diffraction, Raman scattering or Photoemission spectroscopy. [29]

Since in Lanczos algorithms the Hilbert space of the Hamiltonian operator grows exponentially with the cluster size, there are memory restrictions on the number of sites which can be studied given by the storage capacities of present day computers. The largest matrices which can presently be diagonalized have approximately $\sim 1,350,000$ basis states. (This is the approximate size of the reduced Hilbert space for a Hubbard model on the 4×4 square cluster at half-filling.) If an efficient procedure is implemented to read from and write to disk, then the number of basis states can be dramatically increased. Because of these restrictions on the cluster size, there are

limitations for a complete finite-size scaling analysis with this technique. Commonly, the Lanczos method is thus preferably used in the study of low-dimensional systems, like in our example of a 1D Heisenberg cluster. However, even in 2D bulk properties can be computed with reliability, in particular if the correlation lengths for a given system do not exceed the cluster size.

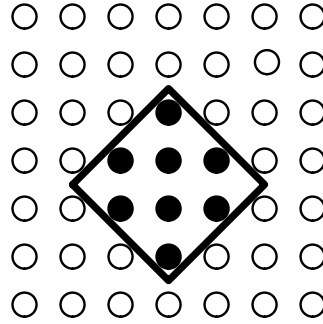


Figure 2.1: An $\sqrt{8} \times \sqrt{8}$ cluster is constructed on top of a base side defined by the vector $\mathbf{R} = 2\hat{x} + 2\hat{y}$.

It has become commonplace in the Lanczos literature to diagonalize not only 2D clusters with $M \times M$ sites, but also other square clusters, which have axes forming a nonzero angle with the lattice axes. Here we show how to construct tilted square clusters that completely cover the two dimensional square lattice. As an example let us consider the $\sqrt{8} \times \sqrt{8}$ cluster shown in Fig.2.1. As a base side a vector $\mathbf{R} = n\hat{x} + m\hat{y}$ commensurate with the square lattice is chosen. Both of the integers (n,m) have to be even or odd to guaranty for a N ($= \sqrt{N} \times \sqrt{N}$)-site cluster that $N = \mathbf{R}^2 = n^2 + m^2 = \text{even}$, e.g. $N = 2^2 + 2^2 = 8$ for the $\sqrt{8} \times \sqrt{8}$ cluster and $N = 3^2 + 1^2 = 10$ for the $\sqrt{10} \times \sqrt{10}$ cluster.[30] Then a square is constructed from the base side. The lattice sites inside the square belong to the tilted cluster.

Examples can be found in Ref.[30]. Some of the “magic” number of sites that admit a complete covering of the bulk lattice with tilted squares are $N = 8, 10, 16, 18, 20, 26, 32, \dots$

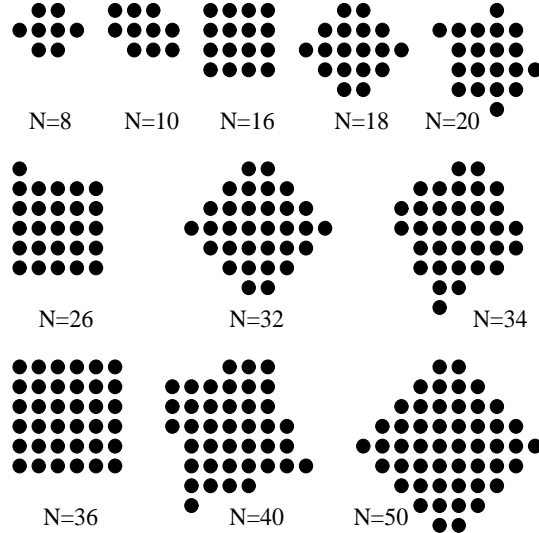


Figure 2.2: Shapes of some tilted 2D clusters used in the Lanczos literature. N is the total number of sites.

In Fig. 2.2 we explicitly provide the actual shape of some clusters which may be useful for the implementation of the Lanczos technique in 2D systems. Each of these clusters can be circumscribed by a square. Note that some of these clusters do not have all the symmetry properties of the bulk (e.g. reflections with respect to the axes are particularly subtle). The reader should not be confused by the shape of these clusters. For example, rotations in 90 degrees exist in the $N=32$ cluster and in many others, although it may not seem obvious.

2.2 Setting Up the Basis

Memory limitations impose severe restrictions on the size of the clusters that can be studied with the Lanczos method. To understand this point, note that

although the lowest energy state can be written in a tridiagonal $\{|\phi_n\rangle\}$ basis as $|\psi_0\rangle = \sum_m c_m |\phi_m\rangle$, this expression is of no practical use unless $|\phi_m\rangle$ itself is expressed in a convenient basis to which the Hamiltonian can be easily applied. For example, consider the basis for spin-1/2 models where S_z is defined at every site, schematically represented as $|n\rangle = |\uparrow\downarrow\uparrow \dots\rangle$.

When setting up the S^z -basis for a given spin-1/2 Heisenberg cluster, it is useful to represent a given S^z -basis state by a binary number, since the action of the Hamiltonian operator on these basis states can then be done using efficient logical operations which are implemented in most computers as intrinsic functions. One way of doing this is by labeling the lattice sites having an up-spin by a '0' and those with a down-spin by a '1'. For example, the two Néel states of the 4-site chain can be represented as

$$\begin{aligned} |\downarrow\uparrow\downarrow\uparrow\rangle &\equiv (1, 0, 1, 0), \\ |\uparrow\downarrow\uparrow\downarrow\rangle &\equiv (0, 1, 0, 1). \end{aligned} \tag{2.1}$$

Once the down-spins have been placed the whole configuration has been uniquely determined since the remaining lattice sites can only be occupied by up-spins. The set of binary numbers (one per site) can then be easily converted into an integer $i_{dw} \equiv \sum_{i\downarrow} 2^{i\downarrow}$ where the summation index $i\downarrow$ represents all positions in the lattice where a down-spin resides. For example :

$$\begin{aligned} (0, 1, 0, 1) &\rightarrow 2^0 + 2^2 = 5, \\ (1, 0, 1, 0) &\rightarrow 2^1 + 2^3 = 10, \end{aligned} \tag{2.2}$$

where the rightmost lattice position has been labeled as cluster point '0', the one to the left of it as '1', etc. .

Using the above convention for an integer representation of each basis state, let us systematically set up the whole S^z -basis starting with the configuration corresponding to the lowest value for the integer i_{dw} . For the $S_{\text{tot}}^z = 0$ subspace of the 4-site chain, this is given by

$$\begin{aligned}
 |\uparrow\uparrow\downarrow\downarrow\rangle &\rightarrow i_{dw}(1) = 3 \\
 |\uparrow\downarrow\uparrow\downarrow\rangle &\rightarrow i_{dw}(2) = 5 \\
 |\uparrow\downarrow\downarrow\uparrow\rangle &\rightarrow i_{dw}(3) = 6 \\
 |\downarrow\uparrow\uparrow\downarrow\rangle &\rightarrow i_{dw}(4) = 9 \\
 |\downarrow\uparrow\downarrow\uparrow\rangle &\rightarrow i_{dw}(5) = 10 \\
 |\downarrow\downarrow\uparrow\uparrow\rangle &\rightarrow i_{dw}(6) = 12.
 \end{aligned} \tag{2.3}$$

In Eq.2.3 the argument of the vector i_{dw} just runs over the whole set of states. The whole basis will be represented in a single vector i_{dw} .

In general, the number of down-spins for the $S_{\text{tot}}^z = 0$ subspace to be diagonalized is equal to the number of nested loops over the lattice sites needed to generate the basis, i.e. for the above example two loops are required (the two ‘do 20’ loops in the following routine). In the outermost loop a state with only one down-spin is created. In each of the inner loops one more down-spin is added on top of the previous configuration. The following FORTRAN routine generates the states for the above example as shown in increasing order. It can be easily modified to be applicable to larger clusters and other S_{tot}^z subspaces.

```

c          idw(np) stores the configuration of down-spins
c          ‘np’ is greater or equal to the dimension of the Hilbert space
c          ns = number of sites

```

```

c          jspdw = number of down-spins
c          'm1' is just a counter

          integer idw(10)
          ns=4
          jspdw=2
          jend1=ns
          jend2=ns
          m1=1
          do 20 l1=1,jend1
            if(jspdw.gt.1) then
              js2=lshift(1,l1-1)
              jend2=l1-1
            end if
            do 20 l2=1,jend2
              if(jspdw.gt.0) then
                js1=xor(lshift(1,l2-1),js2)
                idw(m1)=js1
                m1=m1+1
              end if
            20 continue
          stop
          end

```

If we had used 'jspdw=1' and 'jend1=1', then the basis states for the $S_{\text{tot}}^z = 1$ subspace would have been obtained. The functions 'xor' and 'lshift' are machine-specific. However, they are standard on SUN and IBM workstations (on a CRAY 'shifl' is used instead). 'lshift' shifts a given binary configuration to the left by the specified number of spacings, e.g. $\text{lshift}(3,1)=6$ corresponds to the process where the configuration "3" of Eq.2.3 is shifted by one unit to the left into the configuration "6", i.e. $|\uparrow\uparrow\downarrow\downarrow\rangle \rightarrow |\uparrow\downarrow\downarrow\uparrow\rangle$. Note that 'lshift' is not necessarily equivalent to a translation in a periodic system, since it only translates a given spin-down configuration to the left and does not provide for reentrance from the right side of the cluster once a spin-down has exited from the left side, i.e. $\text{lshift}(12,1)=8 = |\downarrow\uparrow\uparrow\uparrow\rangle$. Special care is needed for this subtle "boundary" problem.

‘xor’ is the exclusive logical ‘or’-operation which yields a ‘1’ only if one of the two binary entries which are compared is a ‘1’ and the other one a ‘0’, e.g. $\text{xor}(3,6)=(0011).\text{or.}(0110)=(0101)=5$. Later, the logical operations ‘rshift’ and ‘and’ will be used also. While ‘rshift’ is just the inverse to ‘lshift’, ‘and’ yields a ‘1’ only if both of the two binary entries which are compared are ‘1’, e.g. $\text{and}(3,6)=(0011).\text{and.}(0110)=(0010)=2$. In table 2.1 the logical operations ‘and’ and ‘or’ on the binary entries ‘i’ and ‘j’ are listed.

Table 2.1: Table for the logical operations ‘and’ and ‘or’.

i	j	and	or
0	0	0	0
0	1	0	1
1	0	0	1
1	1	1	0

With these definitions of the logical operations and the shift operations the reader can get back to the subroutine on the previous page and show that the output written into the vector ‘idw(n)’ is precisely the 6 states of Eq.2.3.

For electronic one-band models the size of the S^z -basis set grows exponentially with the system size. For example, the dimension of the Hilbert space of a Hubbard model (four states per site) on a N site cluster is in principle 4^N , which for $N = 16$ corresponds to $\sim 4.3 \times 10^9$ states. Such a memory requirement is beyond the reach of present day computers. In practice this problem can be considerably alleviated by

the use of symmetries of the Hamiltonian that reduce the matrix to a block-diagonal form. The most obvious symmetry is the number of particles in the problem which is usually conserved at least for fermionic problems. The total projection of the spin S_{tot}^z , may also be a good quantum number, e.g. the ground state for a system with an even number of fermions typically has $S_{\text{tot}}^z = 0$. For translational invariant problems, the total momentum k of the system is also conserved introducing a reduction of $\sim 1/N$ in the number of states (this does not hold for models with open boundary conditions or explicit disorder). In addition, several Hamiltonians have extra symmetries, like spin inversion. On a square lattice, rotations of $\pi/2$ about a given site, and reflections with respect to the lattice axes are good quantum numbers (although care must be taken in their implementation since some of these operations are combinations of others and thus not independent).

Here we will present as an example the implementation of translational symmetry for spin chains. When generating the S^z -basis states a subroutine is called which acts with the translational operator $\hat{T}_r(k)$ on a given state, and thus creates “classes” of states which have momentum as a good quantum number. The phase acquired by each translation of the starting state is $e^{(-ikr)}$, where $k = 2\pi n/ns$, ns is the number of lattice sites, and n ($= 0, 1, \dots, ns$) is an integer number labeling the quantization state. Only one representative per class of good momentum is kept (for example the state with the smallest integer), i.e. for the 4-site ($k=0$, $S_{\text{tot}}^z = 0$) state $\frac{1}{\sqrt{4}}[|\uparrow\uparrow\downarrow\downarrow\rangle + |\uparrow\downarrow\downarrow\uparrow\rangle + |\downarrow\downarrow\uparrow\uparrow\rangle + |\downarrow\uparrow\uparrow\downarrow\rangle]$ only the representative $|\uparrow\uparrow\downarrow\downarrow\rangle = 3$ is stored. These classes form a new translationally invariant basis. In the above routine the call for the symmetry subroutine should thus be inserted right before basis states are written to the vector ‘idw’, otherwise it is simply lost. Only if the

state 'js1' is the first representative of a translationally invariant class should it be written to the vector 'idw'. A FORTRAN example for such a symmetry subroutine is provided here.

```

c          This subroutine generates members of a
c          momentum symmetry class for a given input state js1
c          idw1(nc) stores the configurations of down-spins belonging to
c          classes generated by the symmetry operation
c          signr(nc) and signi(nc) are the real and imaginary parts of the
c          phases acquired by the symmetry operation
c          nc = number of states in a class
c          ns = number of sites
c          itouch=1 only when a new class is successfully generated from the
c          jsecth = momentum of translational operator in units of  $2\cdot\pi/ns$ 
c          input state js1, else itouch=0
c          jspdw = number of down-spins

          subroutine symlin(js1,idw1,nc,itouch,signr,signi)
          integer idw1(10),iarg(10)
          real signr(10),signi(10),snewr,snewi,diff

          ns=4
          jsecth=2
          idw1(1)=js1
          signr(1)=1.0
          signi(1)=0.0
          iarg(1)=0
          itouch=0
          nc=1
          init=1
          iend=1
          do 10 jv=1,ns-1
            do 15 iv=init,iend
              j=idw1(iv)
              i1=and(lshift(j,1),(2**ns-2))+and(rshift(j,ns-1),1)
              if(i1.lt.js1) go to 20
              snewr=cos(2.0*3.14159*(jsecth+iarg(iv))/ns)
              snewi=sin(2.0*3.14159*(jsecth+iarg(iv))/ns)
              do 16 iu=1,nc
                if(i1.eq.idw1(iu))then
                  diff=snewr-signr(iu)
                  if(abs(diff).gt.0.0001) go to 20

```

```

diff=snewi-signi(iu)
if(abs(diff).gt.0.0001) go to 20
go to 15
endif
16  continue
    nc=nc+1
    signr(nc)=snewr
    signi(nc)=snewi
    idw1(nc)=i1
    iarg(nc)=jsecth+iarg(iv)
15  continue
    init=iend+1
    iend=nc
10  continue
    itouch=itouch+1
20  return
end

```

For one given S^z -basis state 'js1' this routine produces all nc members of the class with momentum quantum number 'jsecth' (in units of $2\pi/ns$). 'nc' is in many cases equal to the number of sites but can be smaller. The number of classes, NC, in the largest momentum subspace can be estimated for spin systems from the bulk limit value : $NC = \frac{ns!}{n_{up}! \cdot n_{dw}!} \cdot \frac{1}{ns}$ as the number of sites goes to infinity ($ns \rightarrow \infty$); n_{up} and n_{dw} are the number of up-spins and down-spins respectively. This estimate for a basis set reduction by $\frac{1}{ns}$ due to translational invariance is typically a little too small for *finite* systems, e.g. for the ns=8 chain in the $S_{tot}^z = 0$ subspace $\frac{ns!}{n_{up}! \cdot n_{dw}!} \cdot \frac{1}{ns} = \frac{8!}{4! \cdot 4!} \cdot \frac{1}{8} = 8.75$, while the actual number of classes in the largest momentum subspace is 10.

The members of a class are stored in the vector 'idw1', and their respective phases in 'signr' (real part) and 'signi' (imaginary part). The subroutine given as an example in the previous page is for a 4-site cluster and momentum $k = \pi$. It can be generalized to an arbitrary size lattice and arbitrary momentum by changing 'ns' and

‘jsecth’. The action of the translational operator is contained in the statement “i1 = and(lshift(j,1),(2**ns-2)) + and(rshift(j,ns-1),1)”, e.g. the configuration ‘j’ = $|\downarrow\uparrow\uparrow\downarrow\downarrow\uparrow\rangle$ is moved to the left by one lattice spacing (i.e. $|\downarrow\uparrow\uparrow\downarrow\downarrow\uparrow\rangle \rightarrow |\uparrow\uparrow\downarrow\downarrow\uparrow\rangle$). Note that $2^{ns} - 2 = |\downarrow\downarrow\downarrow\downarrow \cdots \downarrow\uparrow\rangle$. Because of periodic boundary conditions the leftmost down-spin enters at the rightmost lattice point. This is achieved by the second ‘and’-operation in the translation. The phase acquired in this transformation is temporarily stored in ‘snewr’ and ‘snewi’.

The outer loop (‘do 10’) runs over all operations associated with the given symmetry, i.e. up to ‘ns-1’ for the translations on a linear lattice. However, for certain states the same set of configurations are already repeated after less than ‘ns-1’ operations. This would be the case, for example, when $js1 = |\uparrow\downarrow\uparrow\downarrow\rangle$ is translated into itself by $\hat{T}_{r=2}(k)$, although $ns-1=3$. Thus a cut-off has to be inserted (‘do 16’ loop) : if a previously configuration is reiterated it is not stored again in ‘idw1’, and if its phase differs from the previous one then no class of good momentum can be generated, and the routine is terminated. Let us consider the example of the state $|\uparrow\downarrow\uparrow\downarrow\rangle = 5$. In the beginning of the routine, this state will be written as a first entry to ‘idw1’ and its phase as first entries to ‘signr’ and ‘signi’ respectively, e.g. $idw1(1)=5$, $signr(1)=1.0$, $signi(1)=0.0$. In the $k=0$ subspace, the first translated state $|\downarrow\uparrow\downarrow\uparrow\rangle = 10 = idw1(2)$ has the phase ($signr(2)=1.0$, $signi(2)=0.0$). Since this state is different from the initial one the ‘do 16’ loop leaves things unchanged. However, the subsequent translation produces $idw1(3)=5$, $signr(3)=1.0$, $signi(3)=0.0$ which is equal to the entries for the initial state. Thus all members of the class corresponding to the initial state have been obtained prior to the termination of the loop over the maximum number of possible translations (‘do 10’).

Then the 'do 16' loop becomes active and forces an exit (go to 15) out of the symmetry generating loop. If the above example is considered for the $k = \pi/2$ subspace the corresponding states and phases are : (idw1(1)=5,signr(1)=1.0,signi(1)=0.0), (idw1(2)=10,signr(2)=0.0,signi(2)=1.0), (idw1(3)=5,signr(3)=-1.0,signi(3)=0.0) For this case the difference in the real part of the phase between the initial state and 'idw(3)' is diff=-2.0. Hence, no translationally invariant state with momentum $k = \pi/2$ can be generated from $|\uparrow\downarrow\uparrow\downarrow\rangle$, and the execution of the symmetry subroutine is interrupted by force using 'if(abs(diff).gt.0.0001) go to 20' which gives a negative result (itouch=0).

In the subroutine 'symlin' we have used the convention that each class is represented by the member state whose integer representation is the lowest of all member states, i.e. the state $\frac{1}{\sqrt{4}}[|\uparrow\uparrow\downarrow\downarrow\rangle + |\uparrow\downarrow\downarrow\uparrow\rangle + |\downarrow\downarrow\uparrow\uparrow\rangle + |\downarrow\uparrow\uparrow\downarrow\rangle]$ is represented by $|\uparrow\uparrow\downarrow\downarrow\rangle = 3$. Then, we want the translational operator only to act on this seed state to generate the other members of the class. If the input state 'js1' is larger than this seed state the subroutine is terminated with a negative result (itouch=0) by the statement if(i1.lt.js1) go to 20.

The variable 'itouch' signals whether a new class for the given quantum number could be generated from a given S^z -state 'js1'. Only if that is the case (itouch=1) should this state be stored as a representative in the routine which generates the basis.

Other symmetries are implemented in a similar manner. The only statement to be replaced is the one which produces the translated state 'il' and the ones related to its phase ('snewr' and 'snewi'). E.g. for spin-inversion symmetry - which is only applicable in the $S^z = 0$ subspace - the first statement is replaced by "i1 = xor(j,2**ns-

1)". Then 'i1' becomes the spin-inverted state of 'j', i.e. $|\uparrow\uparrow\downarrow\downarrow\rangle \rightarrow |\downarrow\downarrow\uparrow\uparrow\rangle$. Note that $2^{n_s} - 1 = |\downarrow\downarrow\downarrow\downarrow \cdots \downarrow\rangle$. Since spin-inversion produces classes made out of only two states, an outer loop summing over all possible operations related to the given quantum number is not necessary in this case. The two possible quantum numbers (\pm) associated with spin-inversion are contained in 'jsecsi' which only affects the real part of the phase. Thus, "snewr= jsecsi" and "snewi=0".

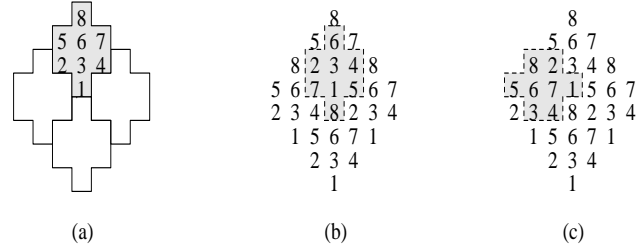


Figure 2.3: Symmetry operation on a tilted 8-site square cluster. (a) The cluster covers the complete 2D square lattice. (b) Vertical translation by one lattice spacing. (c) Anti-clockwise rotation by $\pi/2$.

The symmetry subroutine works also in two dimensions. Here translational invariance in the \hat{x} - and \hat{y} - directions can be treated separately. As mentioned above, for the 2D case there are square clusters which have axes forming a nonzero angle with the lattice axes. As an example we treat here the $\sqrt{8} \times \sqrt{8}$ cluster. As can be seen in Fig. 2.3(a) the 2D plane is completely covered by these *square* lattices. A translation by one lattice spacing in the vertical direction is depicted in Fig. 2.3(b). This operation corresponds to the statement "i1 = and(lshift(j,2),132) + and(lshift(j,3),112) + and(rshift(j,1),8) + and(rshift(j,5),2) + and(rshift(j,7),1) ", e.g. the spin originally on the lattice point '6' is moved to lattice point '8', '4' into '7', etc.. (Here the convention was used that one up-spin at lattice site 'i' contributes with the binary value $2^{(i-1)}$). Let us discuss the above statement in a little more

detail : the first term (`and(lshift(j,2),132)`) locates spins on sites 1 and 6 in their proper place. The second term locates spins on sites 2, 3 and 4. The third term fixes the spin originally at site 5, the fourth term that at site 7, and the last term fixes the spin originally at site 8. Then the outer loop in the symmetry subroutine goes through the 3 possible translations along the \hat{y} - direction, and the phases are the same as for the 1D case.

In Fig. 2.3(c) an anti-clockwise rotation by $\pi/2$ is shown. This operation corresponds to the statement “`i1 = and(lshift(j,2),24) + and(rshift(j,2),2) + and(lshift(j,3),128) + and(rshift(j,4),4) + and(rshift(j,1),64) + and(j,33)`”. Since there are 3 possible $\pi/2$ consecutive rotations until the cluster is mapped again into itself the corresponding quantum number, say ‘jsecro’, can assume 3 different values (‘jsecro=1,2,3’), and the outer loop goes through 3 iterations. The corresponding phases are then given by “`snewr = cos(2.0*3.14159*(jsecro*jv)/ns)` ” and “`snewi = sin(2.0*3.14159*(jsecro*jv)/ns)` ”.

It is clear that the use of symmetries is very important to carry out Lanczos calculations on large enough clusters. Currently, the one-band Hubbard model can be studied on clusters only slightly larger than the 4×4 lattice at least near half-filling, while at low electronic densities larger systems can be dealt with. The three band Hubbard model can be analyzed on the cluster Cu_4O_8 (2×2 cells), but not much bigger. The $t - J$ model has been studied on clusters of up to 26 sites at low hole density, and perhaps lattices of 32 sites will be reachable in the near future. Note that this model has a maximum in the dimension of its Hilbert space at an intermediate hole density.

Finally, let us turn to systems with more than two possible orientations per lattice site, e.g. the spin-1 chain (with $S^z = -1, 0, 1$), the t-J model ($|\uparrow\rangle, |\downarrow\rangle, |0\rangle$) or the Hubbard model ($|\uparrow\rangle, |\downarrow\rangle, |0\rangle, |\uparrow\downarrow\rangle$). In these cases the entire information for a given state cannot be stored in only one integer, 'idw', but we need at least two, i.e. 'iup' and 'idw'. For example, configurations for the spin-1 chain can be described by integer pairs $|S^z = -1\rangle : (0, 1), |S^z = 0\rangle : (0, 0), |S^z = 1\rangle : (1, 0)$. Then, a state of the spin-1 chain can be labeled like i.e. $|\uparrow\uparrow 0 \downarrow 0 \downarrow\rangle : i_{\text{up}} = 2^4 + 2^5 = 48, i_{\text{dw}} = 2^0 + 2^2 = 5$, where we have again followed the convention that the rightmost lattice site is labeled as cluster point '0', the one to the left of it as '1', etc. . The necessary subroutines to produce the basis states for a given spin-1 chain are a natural extension of the routines presented above and will not be discussed here.

However, for systems involving mobile fermions, like the t-J model away from half-filling or the Hubbard model, there is an additional complication due to the *fermion anticommutation relations*:

$$\begin{aligned} \{c_i^\dagger, c_j\} &= \delta_{i,j}, \\ \{c_i^\dagger, c_j^\dagger\} &= \{c_i, c_j\} = 0. \end{aligned}$$

As a consequence of these relations there is a phase difference (a minus sign) between states like $c_{0\uparrow}^\dagger c_{1\uparrow}^\dagger |\text{vac}\rangle$ and $c_{1\uparrow}^\dagger c_{0\uparrow}^\dagger |\text{vac}\rangle$, i.e. $c_{0\uparrow}^\dagger c_{1\uparrow}^\dagger |\text{vac}\rangle = -c_{1\uparrow}^\dagger c_{0\uparrow}^\dagger |\text{vac}\rangle$. Since both sides of the equation correspond to a state $|\uparrow\uparrow\rangle$, we have to choose one order - the *normal order* - of fermion operators over the other to uniquely describe this state, e.g. $|\uparrow\uparrow\rangle \equiv c_{0\uparrow}^\dagger c_{1\uparrow}^\dagger |\text{vac}\rangle$. However, due to the periodic boundary conditions, the action of the translational operator forces the reentry of a fermion which exits the left of the

chain on the right side, hence potentially destroying the normal order. To illustrate this point let us look at the action of the 1D translational operator through r lattice spacings, $\hat{T}_r(\mathbf{k}) \equiv e^{i\mathbf{k}r} \prod_{\sigma=\pm} \prod_{i_{occ}}^{n_{\sigma}} c_{i_{occ}+r,\sigma}^{\dagger} c_{i_{occ},\sigma}$, on the state $c_{1\uparrow}^{\dagger} c_{2\downarrow}^{\dagger} |\text{vac}\rangle = |0 \downarrow \uparrow 0\rangle$ in a 4-site chain. In the definition of the translational operator, the product runs over all n_{σ} occupied sites. For momentum $\mathbf{k}=0$ and translation by one lattice spacing $r=1$, we have $\hat{T}_1(\mathbf{k}=0)|0 \downarrow \uparrow 0\rangle = c_{2\uparrow}^{\dagger} c_{1\uparrow} c_{3\downarrow}^{\dagger} c_{2\downarrow} c_{1\uparrow}^{\dagger} c_{2\downarrow}^{\dagger} |\text{vac}\rangle = +c_{2\uparrow}^{\dagger} c_{3\downarrow}^{\dagger} |\text{vac}\rangle = +|\downarrow \uparrow 00\rangle$. Thus, a translation without a jump across the boundary causes a plus sign, while $\hat{T}_1(\mathbf{k}=0)|\downarrow \uparrow 00\rangle = c_{3\uparrow}^{\dagger} c_{2\uparrow} c_{0\downarrow}^{\dagger} c_{3\downarrow} c_{2\uparrow}^{\dagger} c_{3\downarrow}^{\dagger} |\text{vac}\rangle = +c_{3\uparrow}^{\dagger} c_{0\downarrow}^{\dagger} |\text{vac}\rangle = -|\uparrow 00 \downarrow\rangle$. The $\mathbf{k}=0$ state for the above example would thus be $\frac{1}{2}[+|\downarrow \uparrow 00\rangle - |\uparrow 00 \downarrow\rangle + |00 \downarrow \uparrow\rangle + |0 \downarrow \uparrow 0\rangle]$. The best place to implement this additional phase shift due to the fermion anticommutation relations is in the symmetry subroutine, i.e. ‘symlin’ which has been discussed a few pages before. If the convention of the above example is used, a phase shift occurs only when in a translation a spin jumps across the boundary, and only when there is an odd number of spins of a kind on a chain with an even number of sites.

2.3 Calculating the Matrix Elements

In this section the matrix elements for the Heisenberg Hamiltonian

$$\begin{aligned}
 H &= J \sum_{\langle ij \rangle} \mathbf{S}_i \cdot \mathbf{S}_j \\
 &= J \sum_{\langle ij \rangle} [(S_i^z S_j^z) + \frac{1}{2}(S_i^+ S_j^- + S_i^- S_j^+)]
 \end{aligned} \tag{2.4}$$

are calculated in the S^z -basis.[31] When not using a basis which is reduced by symmetries, the Ising term $(S_i^z S_j^z)$ yields only diagonal matrix elements while the fluctuation terms $\frac{1}{2}(S_i^+ S_j^- + S_i^- S_j^+)$ give strictly off-diagonal contributions to the matrix

representation. However, when symmetries are introduced the fluctuation terms can also have diagonal contributions.

The fluctuation terms cause an exchange in spin-orientation between neighbors with opposite spins, e.g. $|\uparrow\downarrow\downarrow\uparrow\rangle \rightarrow |\downarrow\uparrow\downarrow\uparrow\rangle$ and $|\uparrow\downarrow\downarrow\uparrow\rangle \rightarrow |\uparrow\downarrow\uparrow\downarrow\rangle$. The way to implement spin-flip operations of this kind on the computer is by defining so-called ‘masks’, which indicate the position of the spin-pair to be exchanged. A mask is a binary with ‘0’ everywhere but at the position of the spin-pair to be flipped, e.g. $(0, \dots, 0, 1, 1, 0, \dots, 0)$. Then the logical operation ‘xor’ can be used on the initial state and the mask state to produce the final configuration with spins flipped at the position indicated by the mask. As an example, for a 6-site chain the mask state $(0, 0, 1, 1, 0, 0) = |\uparrow\uparrow\downarrow\downarrow\uparrow\uparrow\rangle = 2^2 + 2^3 = 12$ flips the spins at sites ‘2’ and ‘3’ (starting to count from the right with site ‘0’). Acting with this mask on the state $|\uparrow\downarrow\uparrow\downarrow\uparrow\downarrow\rangle = 21$ yields $\text{xor}(21, 12) = (010101) \text{.or.} (001100) = (011001) = 25 = |\uparrow\downarrow\downarrow\uparrow\uparrow\downarrow\rangle$.

It is convenient to produce all masks needed for a given operation at a certain cluster geometry in a separate subroutine. Here we present an example for a simple routine which gives all masks, here denoted as ‘ibond1’, for spin-flip operations on a linear lattice with periodic conditions.

```

c          ni < nj label the two sites for a given bond
c          ibond1(nb) : stores the mask configuration for
c          two nearest neighbor down-spins
c          ns : number of sites
c          nb : number of bonds
c
c          subroutine bonlin(ni,nj,ibond1)
c
c          integer ni(8),nj(8),ibond1(8)
c
c          ns=4
c          nb=2*ns
c          do 10 in=1,ns-1
```

```

      ni(in)=in
      nj(in)=in+1
10  continue
      ni(ns)=1
      nj(ns)=ns
      do 15 id=1,nb
          n1=ni(id)-1
          n2=nj(id)-1
          ibond1(id)=2**n1+2**n2
15  continue
      return
      end

```

In this routine all possible neighbor pairs (ni,nj) are constructed. The corresponding mask state is then simply the binary ‘ibond1’ corresponding to two spin-downs at (ni,nj). For more complicated cluster geometries, like 2D tilted clusters, the only change that has to be introduced in this routine is the entries for the pairs (ni,nj) as is shown in Fig.2.4.

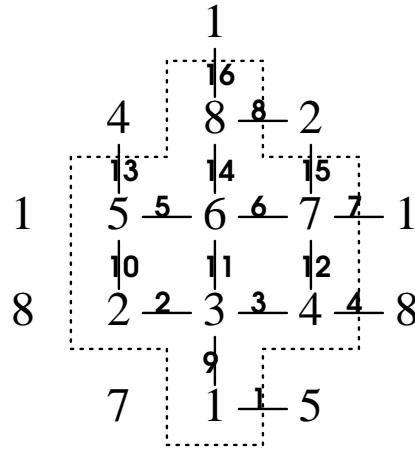


Figure 2.4: Labeling of sites and bonds on a periodic $\sqrt{8} \times \sqrt{8}$ cluster.

The entries for ‘ni’ and ‘nj’ in the above subroutine for an $\sqrt{8} \times \sqrt{8}$ cluster would thus be : ni(1)=1,nj(1)=5, ni(2)=2,nj(2)=3, , ni(9)=1,nj(9)=3,ni(10)=2,nj(10)=5, Similarly for next nearest neighbor interactions a mask ‘ibond2’ can be defined

which involves pairs of next nearest neighbor sites. E.g. for the $\sqrt{8} \times \sqrt{8}$ cluster those would be : $ni(1)=1,nj(1)=4,ni(2)=2,nj(2)=6, \dots, ni(9)=1,nj(9)=2, \dots$

Now all off-diagonal elements can be constructed using the masks for the given cluster. Since typically electronic Hamiltonian matrices (e.g. for Heisenberg, Hubbard or t-J models) are sparse, it is convenient to store only the non-zero off-diagonal matrix elements, say 'hj', and their position in the matrix. Furthermore, since the matrix representation of any quantum mechanical Hamiltonian is hermitian, only the upper right triangle of the matrix has to be stored. The size of the vector for the *diagonal* elements, say 'sdiag', requires less memory, and thus even the 'zero-entries' can be stored. In Fig.2.5 the structure of the Hamiltonian matrix representation is visualized.

$$\begin{bmatrix} \text{sdiag}(1) & 0 & \dots & 0 & \text{hj}(1) & 0 & \dots & 0 & \text{hj}(2) & 0 & \dots \\ & \text{sdiag}(2) & 0 & \dots & & 0 & \text{hj}(3) & 0 & \dots & & \\ & & \text{sdiag}(3) & & & & & & \dots & & \\ & & & \ddots & & & & & & \ddots & \\ & & & & \ddots & & & & & & \ddots \end{bmatrix}$$

Figure 2.5: Schematic matrix representation for a Hamiltonian with diagonal elements 'sdiag' and off-diagonal elements 'hj'.

To get a notion of the memory requirements, consider the 16-site Heisenberg chain. In the $S_{\text{tot}}^z = 0$ subspace there are $NC = \frac{16!}{8!8!} = 12,870$ states when no symmetries are used. This is the linear size of the corresponding matrix representation, and also equal to the number of diagonal matrix elements. Thus naively a

$12,870 \times 12,870$ matrix would have to be stored. However, since only the upper right triangle of the matrix needs to be considered, this reduces to approximately $\frac{NC \cdot NC}{2} = \frac{12,870 \cdot 12,870}{2} = 82,818,450$ states. If only the non-zero off-diagonal elements are stored this number can be reduced dramatically. For the spin-1/2 chain the size of the vector corresponding to the non-zero off-diagonal matrix elements can be estimated by considering the number of possible spin-flips generated from a given configuration. The maximum number of spin-flips is obtained from the Néel configurations $|\uparrow\downarrow\uparrow\downarrow \dots\rangle$ and $|\downarrow\uparrow\downarrow\uparrow \dots\rangle$, e.g. these configurations have matrix elements with N other states for a N -site cluster. Thus an upper boundary for the number of non-zero off-diagonal elements is given by $\frac{NC \cdot NC}{2} \cdot \frac{N}{NC} = \frac{NC \cdot N}{2}$, i.e. $\frac{12,870 \cdot 16}{2} = 102,960$ for the above example. However, the typical number of transitions for a given configuration due to spin fluctuations is considerably lower, i.e. the two states with the least number of spin-flips (only two) are the ‘phase separated’ states $|\downarrow\downarrow \dots \downarrow\downarrow\uparrow\uparrow \dots \uparrow\uparrow\rangle$ and $|\uparrow\uparrow \dots \uparrow\uparrow\downarrow\downarrow \dots \downarrow\downarrow\rangle$.

Before we turn to an example of a subroutine which produces matrix elements for the Heisenberg chain, let us discuss how to store the position of the non-zero off-diagonal matrix elements ‘hj’ in an efficient manner. A standard way of storing sparse matrices is to write the horizontal position of non-vanishing elements above the diagonal in the Hamiltonian matrix to an integer vector, say ‘icolmj’, and the number of non-zero elements per column to another integer vector, say ‘knon0j’. Let us for example consider the Hamiltonian matrix for a 4-site Heisenberg chain in

the $S_{\text{tot}}^z = 0$ subspace [31]

$$H = J \begin{pmatrix} 0 & 1/2 & 0 & 0 & 1/2 & 0 \\ 1/2 & -1 & 1/2 & 1/2 & 0 & 1/2 \\ 0 & 1/2 & 0 & 0 & 1/2 & 0 \\ 0 & 1/2 & 0 & 0 & 1/2 & 0 \\ 1/2 & 0 & 1/2 & 1/2 & -1 & 1/2 \\ 0 & 1/2 & 0 & 0 & 1/2 & 0 \end{pmatrix}. \quad (2.5)$$

Using the above convention the entries for ‘icolmj’ are (2,5,3,4,6,5,5,6), while for ‘knon0j’ we get (2,3,1,1,1), storing only the upper right triangle of the matrix.

In the subroutine ‘smatel’ (shown below) the diagonal and off-diagonal matrix elements for a 4-site Heisenberg chain are evaluated. The only change which needs to be introduced to generalize this routine to arbitrary cluster sizes and shapes is done by adjusting the number of lattice sites ‘ns’. Appended to this routine is another subroutine ‘search’ which finds the label ‘my’ for a binary input state ‘jx’. This routine is called to determine the horizontal position of an off-diagonal matrix element $\langle \text{jketdw} | H | \text{jx} \rangle$, where ‘jketdw’ is the initial configuration and ‘jx’ is generated from ‘jketdw’ by a spin-flip operation as discussed above.

```

c      idw0(nclass) stores representatives for the nclass classes
c      created by symmetry operations
c      icount is the number of non-zero off-diagonal matrix
c      elements ‘hj’ created in this routine
c      ‘icolmj’ stores the number of the column where each non-zero
c      off-diagonal matrix element resides
c      ‘knon0j’ is the number of non-zero off-diagonal matrix
c      elements in a given column
c      The diagonal matrix elements are stored in sdiag(nclass)
c      ‘sclass’ stores the square root of the number of states
c      for a given class

```

```

c      subroutine 'bonlin' defines the mask
c      configurations (explained before)
c      subroutine 'symlin' generates representatives
c      of the classes (explained before)

      subroutine smatel(idw0,nclass,icount,hj,icolmj,knon0j,
1  sdiag,sclass)

      integer ni(8),nj(8),ibond1(8)
      complex hj(10)
      real zr(10),zi(10),sdiag(10),sclass(10)
      integer nmy(10)
      real signr(10),signi(10)
      integer idw1(10),idw0(10)
      integer icolmj(10),knon0j(10)
      integer nsr(8)

      ns=4
      nb=ns*2
      nmax=2**ns-1
      icount=0
      call bonlin(ni,nj,ibond1)

      do 41 m1=1,nclass

c
c      diagonal contributions
c
      jketdw=idw0(m1)

c
c      'nsr(is)' stores the spin (0 or 1) at site 'is'
c
      nm1my=0
      do 15 is=1,ns
         i1=is-1
         nsu=and(rshift(jketdw,i1),1)
15      nsr(is)=nsu
      zrm1=0.0

c
c      'zrm1' accumulates the diagonal contributions from  $\sum_{i,j} S_i^z S_j^z$ 
c      'ni(n)' and 'nj(n)' are the sites at the end of bond 'n'
c
      do 20 n=1,nb
         nbi=ni(n)
         nbj=nj(n)
         ir=nsr(nbi)+nsr(nbj)
         if(ir.eq.1)then

```

```

        zrm1=zrm1-0.25
    else
        zrm1=zrm1+0.25
    endif
20    continue

c
c    off-diagonal contributions
c

    call symmlin(jketdw,idw1,no,itouch,signr,signi)
do 37 lc=1,no
    jbradw=idw1(lc)
    do 25 j2=1,nb
        ibd1=ibond1(j2)
        jtypdw=and(jbradw,ibd1)
        if(jtypdw.eq.ibd1)go to 25
        if(jtypdw.gt.0)then
            jy=xor(jbradw,ibd1)
            call search(jy,idw0,nclass,itouch,my)
            if(itouch.eq.1)then
                if(my.gt.m1)then
                    nm1my=nm1my+1
                    nmy(nm1my)=my
                    zr(nm1my)=0.5*signr(lc)
                    zi(nm1my)=0.5*signi(lc)
                else if(my.eq.m1)then
                    zrm1=zrm1+0.5*signr(lc)
                endif
            endif
        endif
    endif
25    continue
37    continue
    sdiag(m1)=zrm1
    den = 1.0/sclass(m1)
    do 38 i=1,nm1my
        ind=nmy(i)
        ip=i+icount
        icolmj(ip)=ind
        hj(ip)=cmplx(zr(i),zi(i))*sclass(ind)*den
38    continue
    icount=icount+nm1my
    knon0j(m1)=nm1my
41 continue
    return

```

```

                                end
c*****
c                                This routine finds whether the input state 'jx' is
c                                a representative of a class (i.e. the state in a class
c                                with the minimum integer representation). If yes, itouch=1
c                                Also, it finds the label 'my' of the state, which will
c                                be the number of the matrix column where the
c                                corresponding matrix element is placed
                                subroutine search(jx,idw0,nclass,itouch,my)
                                integer idw0(10)
                                itouch=0
                                n2=nclass
                                n1=1
34 if(n1.gt.n2) go to 50
                                my=(n1+n2)/2
                                if(jx.gt.idw0(my)) go to 35
                                if(jx.eq.idw0(my)) go to 36
                                n2=my-1
                                go to 34
35 n1=my+1
                                go to 34
36 itouch=1
50 continue
                                return
                                end

```

After the subroutine 'bonlin' has been called to set up the geometry of the cluster a loop over all classes which make up the basis is started ('do 41'). The diagonal matrix elements for a given representative 'jketdw' are obtained by subsequently testing pairs of neighboring spins for their relative orientation ('do 20' loop). If they are equal they contribute $J/4$ to the corresponding matrix element, else it is $-J/4$. The preliminary diagonal element is then stored in 'zrm1'. Information about the spin orientation at a given site 'is' is obtained from the operation $\text{and}(\text{rshift}(\text{jketdw}, \text{is}-1), 1)$. If this quantity is equal to '1' there is a down-spin at site 'is', else it is an up-spin.

The off-diagonal elements are obtained in the 'do 25' loop. If symmetries are used they depend on the relative phase acquired by the symmetry operation(s), thus the symmetry subroutine 'symlin' has to be called before the off-diagonal elements can be calculated. Then an additional loop over the members of the class represented by 'jketdw' ('do 37') has to be added since a given initial state might have a non-vanishing transition into another class but not necessarily into its representative.

In the 'do 25' loop a spin-flipped state $jy = \text{xor}(jbradw, ibond1(j2))$ is constructed from an initial configuration 'jbradw' using the mask 'ibond1' if the two spins located at the positions indicated by 'ibond1' have opposite orientation. Then, the subroutine 'search' is called to determine whether 'jy' is a representative. If yes (itouch = 1) the label 'my' of the new state is obtained. 'my' indicates the column to where the matrix element under construction will be written. Each contribution from a spin-flipped pair at two neighboring sites corresponding to the mask 'ibond1' is stored in zr (real part) and zi (imaginary part). The energy contribution is $J/2$ (plus the phase acquired by symmetry operations) per flipped pair. If the spin-flip transition maps the initial state 'jbradw' into itself (this can only be the case when symmetries are used) the contribution of $J/2$ (plus phase) goes to the corresponding diagonal matrix element 'zrm1'. Once this loop is completed all contributions to the diagonal elements are written to 'sdiag' and the ones to the off-diagonal elements are stored in 'hj'.

In the 'do 38' loop, the Hamiltonian matrix is set up as visualized in Fig.2.5, e.g. the number of the column where the off-diagonal Hamiltonian matrix element 'hj' is stored is written to the integer vector 'icolmj', etc.. Later, the number of entries

for a given column 'n' are stored in the vector 'knon0j(n)'. The factors going into 'hj' are :

1. a factor $\frac{1}{2}$ which stems from the prefactor of the fluctuation term $(S_i^+ S_j^- + S_i^- S_j^+)$ (enters in 'zr' and 'zi'),
2. phases associated with the momentum of the subspace which also enter 'zr' and 'zi',
3. factors associated with the number of states per class, 'sclass'.

As an example, we discuss the off-diagonal matrix element between the $k=0$ states of a 4-sites chain (see also Appendix B). The only two states in the $k=0$ subspace are $|a\rangle = \frac{1}{\sqrt{4}}[|\uparrow\uparrow\downarrow\downarrow\rangle + |\uparrow\downarrow\downarrow\uparrow\rangle + |\downarrow\downarrow\uparrow\uparrow\rangle + |\downarrow\uparrow\uparrow\downarrow\rangle]$ and $|b\rangle = \frac{1}{\sqrt{2}}[|\uparrow\downarrow\uparrow\downarrow\rangle + |\downarrow\uparrow\downarrow\uparrow\rangle]$. Then, $\langle b | \frac{1}{2} \sum_{\langle i,j \rangle} (S_i^+ S_j^- + S_i^- S_j^+) | a \rangle = [(\langle \uparrow\downarrow\uparrow\downarrow | + \langle \downarrow\uparrow\downarrow\uparrow |) \frac{1}{\sqrt{2}} \frac{1}{2} 4 \frac{1}{\sqrt{4}} (|\uparrow\downarrow\uparrow\downarrow\rangle + |\downarrow\uparrow\downarrow\uparrow\rangle)] = \sqrt{2}$. Here, 'sclass' for state $|a\rangle$ is ' $\sqrt{4}$ ', and for state $|b\rangle$ it is ' $\sqrt{2}$ '. The ratio of these factors enters 'hj' as 'sclass(ind)*den' in the 'do 38' loop, where 'ind' indicates the number of the column associated with state $|a\rangle$.

The subroutine 'search' determines for a given input state 'jx' whether it is a representative of a class, and if it is, then finds the corresponding label 'my' for that state. The search is done by iterative comparison of the input state with all representatives stored in 'idw0'. The search result is positive (itouch=1) when the input state can be matched with one of the representatives (see the line : 'if(jx.eq.idw0(my)) go to 36'). Then also the associated label 'my' of the input state is returned. This label indicates the column corresponding to 'jx' in the Hamiltonian matrix.

Both subroutines, 'smatel' and 'search', are quite general and apply to spin systems of any size or shape. It is a good idea to keep the geometry dependent operations in separate routines (such as 'symlin' and 'bonlin'). Then changes in the code can be implemented only at a few problem dependent locations in the program.

Finally, for the case of systems with mobile fermions, such as the t-J and the Hubbard model, there is a hopping contribution of the form $H_t = -t \sum_{\langle ij \rangle, \sigma} [c_{i,\sigma}^\dagger c_{j,\sigma} + \text{h.c.}]$ to the Hamiltonian. (For the case of the t-J model this term acts only in the restricted space where no double occupancy at a single site is allowed.) The evaluation of matrix elements for this term is analogous to the the procedure in 'smatel'. However, care has to be taken because of the *fermion anticommutation relations* (Eq. 2.4) which were mentioned at the end of the preceeding section.

Let us first focuss on an example to illustrate the problem. The following matrix element of the hopping Hamiltonian yields a negative contribution : $\langle \downarrow 0 \uparrow 0 | H_t | \downarrow \uparrow 00 \rangle = \langle \text{vac} | c_{3\downarrow} c_{1\uparrow} (-t c_{1\uparrow}^\dagger c_{2\uparrow}) c_{2\uparrow}^\dagger c_{3\downarrow}^\dagger | \text{vac} \rangle = -t$. On the other hand, the following matrix element gives a contribution with the opposite sign : $\langle 0 \uparrow 0 \downarrow | H_t | \downarrow \uparrow 00 \rangle = \langle \text{vac} | c_{2\uparrow} c_{0\downarrow} (-t c_{0\downarrow}^\dagger c_{3\downarrow}) c_{2\uparrow}^\dagger c_{3\downarrow}^\dagger | \text{vac} \rangle = t$. The difference in sign between the two matrix elements is associated with the jump of a spin across the periodic chain boundary, i.e. in the second example the hopping term, $-t c_{0\downarrow}^\dagger c_{3\downarrow}$, forces such a jump. Then, the anticommutation relations between the fermion operators yield a minus sign for this transition. In analogy to the discussion of normal ordering in the set-up of translational invariant basis states, the occurrence of a phase due to fermion anticommutation relations depends on the number of spins of a kind in the state which is acted upon with the hopping operator, i.e. an odd number of

up- or down-spins in a chain with an even number of sites is a prerequisite for such a phase change.

In 2D systems the phases due to anticommutation can appear even if no fermions are crossed at the boundary. For example, if we have the following configuration on a ladder

$$\left| \begin{array}{cccc} \uparrow & 0 & 0 & 0 \\ \downarrow & 0 & \uparrow & 0 \end{array} \right\rangle$$

where the sites are labelled as

$$\left| \begin{array}{cccc} 7 & 6 & 5 & 4 \\ 3 & 2 & 1 & 0 \end{array} \right\rangle$$

then moving the spin from ‘1’ to ‘5’ gives a minus-sign.

2.4 The Lanczos Procedure

In this section the actual Lanczos procedure is discussed, i.e. a matrix representation in which the given Hamiltonian is tridiagonal is found iteratively. After this step is carried out, the evaluation of the lowest eigenvalue and its corresponding eigenvector can be done using standard routines (e.g. ‘Numerical Recipes’ or ‘Eispack’ provide such routines).[27]

The Lanczos method can be described as follows : first, it is necessary to select an arbitrary vector $|\phi_0\rangle$ in the Hilbert space of the model being studied. The overlap between the actual ground state $|\psi_0\rangle$, and the initial state $|\phi_0\rangle$ should be nonzero. If no “a priori” information about the ground state is known, this requirement is usually easily satisfied by selecting an initial state with *randomly* chosen coefficients

in the working basis that is being used. If some other information on the ground state is known, like its total momentum and spin, then it is convenient to initiate the iterations with a state already belonging to the subspace having those quantum numbers (and still with random coefficients within this subspace).

After $|\phi_0\rangle$ is selected, define a new vector by applying the Hamiltonian \hat{H} to the initial state. Subtracting the projection over $|\phi_0\rangle$, we obtain

$$|\phi_1\rangle = \hat{H}|\phi_0\rangle - \frac{\langle\phi_0|\hat{H}|\phi_0\rangle}{\langle\phi_0|\phi_0\rangle}|\phi_0\rangle, \quad (2.6)$$

that satisfies $\langle\phi_0|\phi_1\rangle = 0$. Now, we can construct a new state that is orthogonal to the previous two as,

$$|\phi_2\rangle = \hat{H}|\phi_1\rangle - \frac{\langle\phi_1|\hat{H}|\phi_1\rangle}{\langle\phi_1|\phi_1\rangle}|\phi_1\rangle - \frac{\langle\phi_1|\phi_1\rangle}{\langle\phi_0|\phi_0\rangle}|\phi_0\rangle. \quad (2.7)$$

It can be easily checked that $\langle\phi_0|\phi_2\rangle = \langle\phi_1|\phi_2\rangle = 0$. The procedure can be generalized by defining an orthogonal basis recursively as,

$$|\phi_{n+1}\rangle = \hat{H}|\phi_n\rangle - \alpha_n|\phi_n\rangle - \beta_n^2|\phi_{n-1}\rangle, \quad (2.8)$$

where $n = 0, 1, 2, \dots$, and the coefficients are given by

$$\alpha_n = \frac{\langle\phi_n|\hat{H}|\phi_n\rangle}{\langle\phi_n|\phi_n\rangle}, \quad \beta_n^2 = \frac{\langle\phi_n|\phi_n\rangle}{\langle\phi_{n-1}|\phi_{n-1}\rangle}, \quad (2.9)$$

supplemented by $\beta_0 = 0$, $|\phi_{-1}\rangle = 0$. In this basis, it can be shown that the Hamiltonian matrix becomes,

$$H = \begin{pmatrix} \alpha_0 & \beta_1 & 0 & 0 & \dots \\ \beta_1 & \alpha_1 & \beta_2 & 0 & \dots \\ 0 & \beta_2 & \alpha_2 & \beta_3 & \dots \\ 0 & 0 & \beta_3 & \alpha_3 & \dots \\ \vdots & \vdots & \vdots & \vdots & \ddots \end{pmatrix} \quad (2.10)$$

i.e. it is tridiagonal as expected. Once in this form the matrix can be diagonalized easily using standard library subroutines, for example the routine ‘TQLI’ provided in ‘Numerical Recipes’. However, note that to diagonalize completely the model being studied on a finite cluster a number of iterations equal to the size of the Hilbert space (or of the subspace under consideration) is needed. In practice this would demand a considerable amount of CPU time. However, one of the advantages of this technique is that accurate enough information about the ground state of the problem can be obtained after a small number of iterations (typically of the order of ~ 100 or less). Thus the method is suitable for the analysis of low temperature properties of models of correlated electrons.

Here we provide an example for a routine which iteratively sets up the tridiagonal representation of a given Hamiltonian as discussed above. The main part of the Lanczos routine (‘lanczs’) is written in a model independent way and can be used for arbitrary systems. The model dependence is contained entirely in the subroutine ‘atimex’ in which the Hamiltonian matrix is applied to a given input vector $|\phi_n\rangle$. At each iteration step, the subroutine ‘TQLI0’ is called to obtain the lowest eigenvalue for the tridiagonal representation under construction. The routine ‘TQLI0’ which only finds the lowest eigenvalue but not the corresponding vector is a slightly modified version of ‘TQLI’ provided in ‘Numerical Recipes’. As outlined there a considerable amount of computing time can be saved when only the eigenvalue is needed. Thus, in our code, the ground state eigenvector is only computed once the eigenvalue has converged up to the specified accuracy, marked ‘tol’. The lines to be omitted from ‘TQLI’ when the ground state vector is not needed are highlighted in ‘Numerical Recipes’ and will not be discussed here.

```

c      In each step of the Lanczos algorithm the values of  $\alpha$ 
c      and  $\beta$  are computed. These are the non-zero elements
c      of the tridiagonal matrix  $T(j)$ . 'ev' is the eigenvalue
c      calculated up to an accuracy specified by 'tol'. 'x' is
c      the input vector, 'xf' is the ground state vector; both
c      have dimension 'np'. 'hj','icolmj','knon0j' and 'sdiag'
c      have been defined and calculated in 'smatel'. The dimensions
c      in this subroutine have been set up for 6 classes and
c      50 Lanczos iterations

      subroutine lanczs(ev,xf,x,hj,icolmj,knon0j,sdiag)

      real sdiag(6),tol
      integer icolmj(10),knon0j(10)
      complex hj(10)
      complex x(6), q(6), y(6), xf(6)
      complex qold
      real alfa(50), beta(50), vectri(50)
      real apro(50),bprov(50),z(50,50)

      itm=50
      itmax=50
      np=6
      nhj=8
      nclass=6
      tol=1.e-10
      il = 1

c
c      just initialize some vectors
c
      25 do i = 1,nclass
         q(i) = cmplx(0.0,0.0)
         y(i) = cmplx(0.0,0.0)
      end do
      if(il.eq.1)then
         do i = 1,nclass
            xf(i) = x(i)
         end do
      else
         do i = 1,nclass
            x(i) = xf(i)
            xf(i) = cmplx(0.0,0.0)
         end do
      endif

c
c      start main loop
c

      evmin0 = 100.0
      do 11 its = 1, itm

```

```

anorm2=0.0
do i = 1,nclass
    anorm2 = anorm2 + x(i)*conjg(x(i))
end do
beta(its) = sqrt(anorm2)
do i = 1,nclass
    qold = q(i)
    q(i) = x(i) / beta(its)
    x(i) = qold
end do

```

C
C
C

C
C
C
C

```

alfa(its) = 0.0
do i = 1,nclass
    x(i) = y(i) - x(i) * beta(its)
    alfa(its) = alfa(its) + real(q(i) * conjg(x(i)))
end do
do i = 1,nclass
    x(i) = x(i) - q(i) * alfa(its)
end do
if (il.eq.1)then
    its0 = its
    do in=1,its0
        aprovl(in)=alfa(in)
        bprovl(in)=beta(in)
    end do

```

C
C
C

```

call tqli0(aprov,bprov,its0,itmax)
ev = 1.0e5
do in=1,its0
    if(aprov(in).lt.ev)then
        e2 = ev
        ev = aprov(in)
        min = in
    endif
end do
if(min.eq.1)then
    do in=2,its0

```

```

diff = abs(aprov(in)-ev)
if(diff.gt.1.0e-6)then
    if(aprov(in).lt.e2)e2 = aprov(in)
endif
end do
endif

c
c      test of accuracy. if satisfied the iterations are terminated
c
    if(its.gt.30.and.abs(ev-evmin0).lt.tol)go to 12
    evmin0 = ev
    else
    do i = 1,nclass
        xf(i) = xf(i) + q(i) * vectri(its)
    end do
    endif
11 continue

c
c      Main loop now finished
c
12 if (il.eq.1)then
    il=2
    itm = its0
    do in=1,its0
        aprov(in)=alfa(in)
        bprov(in)=beta(in)
    end do
    do 40 in=1,its0
        do 41 jn=1,its0
            z(in,jn)=0.0
41      continue
            z(in,in)=1.0
40      continue

c
c      ground state vector of Tm
c
        call tqli(aprov,bprov,its0,itmax,z)
        do in=1,its0
            vectri(in) = z(in,min)
        end do
        go to 25
    else
        anorm=0.0
        do i = 1,nclass
            anorm = anorm + xf(i)*conjg(xf(i))
        end do
        sqnorm = sqrt(anorm)
        do i = 1,nclass
            xf(i) = xf(i) /sqnorm
        end do

```

```

endif
return
end
c*****
c      program to compute  $H|q\rangle = |y\rangle$ 
c      nh: total number of nonzero elements
c      knon0(m1): number of nonzero elements in row m1=1,nclass
c      icolmn(i): column corresponding to the ith nonzero value
c
c      subroutine atimex(q,y,np,nclass,nhj,hj,icolmj,knon0j,sdiag)
c
c      complex hj(nhj)
c      complex q(np),y(np)
c      real sdiag(np)
c      integer icolmj(nhj),knon0j(np)
c      AJ=1.0
c      icounj=0
c
c      do 11 m1=1,nclass
c          y(m1)=AJ*sdiag(m1)*q(m1)
11  continue
c
c      do 21 m1=1,nclass
c          do 25 ic=1,knon0j(m1)
c              icounj=icounj+1
c              jcol=icolmj(icounj)
c              y(m1)=y(m1)+AJ*hj(icounj)*q(jcol)
c              y(jcol)=y(jcol)+AJ*conjg(hj(icounj))*q(m1)
25  continue
21  continue
c
c      return
c      end

```

In the main loop of 'lanczs' ('do 11') a tridiagonal representation of the Hamiltonian is obtained iteratively, and at each iteration step 'its' the eigenvalue 'ev' for the corresponding 'its by its'-matrix is found. The loop runs up to a maximum number of iterations ('itm') specified by the user, only if the eigenvalue has not converged up to an accuracy 'tol' before 'itm' has been reached. As a convergence criterion the eigenvalue at a given iteration 'its' is compared with the one obtained in the previous one ('its-1'). If the difference between these two quantities is smaller than 'tol' the main loop is exited (if(its.gt.30.and.abs(ev-evmin0).lt.tol)go to 12).(The first condition if(its.gt.30 ...) is there to ensure that the Lanczos routine does not get

trapped in a metastable state in the first couple of iterations.) If the eigenvalue does not converge within 'itm' iterations up to the desired accuracy the loop is exited anyway. In that case it is advisable either to repeat the run with more Lanczos iterations 'itm' or to lower the convergence criterion 'tol'.

After the main loop is exited the ground state vector is calculated for the tridiagonal matrix representation of length 'its0', which is equal to the number of iterations needed to converge to the eigenvalue (or 'its0' = 'itm' in case it did not converge). Then the main loop is entered one more time, since the ground state vector obtained in the tridiagonal representation needs to be transformed into the S^z -basis to be useful for taking ground state averages and for the evaluation of dynamical quantities. Since in these last 'its0' runs through the main loop the only step is the transformation of the ground state vector from the basis in which the Hamiltonian is tridiagonal into the S^z -basis, calls for the subroutine 'TQLI0' are unnecessary and are omitted. This is done by defining a variable 'il' which is set to be '1' for the first time the main loop is entered, and '2' for the second time. Using if-statements (if (il.eq.1)then) the call for 'TQLI0' is omitted for the second run-through.

Now let us take a closer look at the technicalities in 'lanczs'. Before the main loop is entered, the complex vectors 'x', 'xf', 'y' and 'q' are initialized. 'q' and 'y' are only temporary vectors, while 'x' and 'xf' are the initial (usually randomly chosen) and final state vectors respectively. When the main loop is entered for the second time to evaluate the ground state vector in the S^z -basis, the initial vector is set equal to the final vector of the last Lanczos iteration before the main loop was exited.

In the main loop ('do 11'), the input vector 'x' is normalized first. The normalization yields the temporary vector 'q' on which the Hamiltonian acts in the

subroutine ‘atimex’. The square root of the normalization constant gives the off-diagonal elements $\beta(\text{its})$ for the given Lanczos iteration ‘its’. Naturally, $\beta(1)$ does not contain any information about the Hamiltonian since it is just the normalization of a randomly chosen seed state. Thus $\beta(1)=\beta_0$ does not appear in the tridiagonal representation (Eq. (2.10)). While the β ’s are off-diagonal contributions from the components of $H|q\rangle$ which do not have a projection on $|q\rangle$ itself, the α ’s measure the projection of the Hamiltonian on the input state ‘q’. In Fig.2.6 one Lanczos iteration step is visualized.

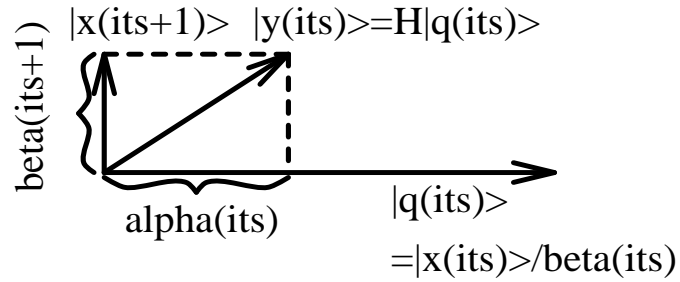


Figure 2.6: Schematic representation of a Lanczos iteration step.

Let us shortly discuss the matrix multiplication performed in the subroutine ‘atimex’. In this routine the Hamiltonian matrix is applied to the normalized input state ‘q’. ‘atimex’ is dependent on the physical system under consideration in two ways : it contains the diagonal (‘sdiag’) and off-diagonal (‘hj’) elements of the Hamiltonian representation (including their positions contained in ‘icolmj’ and ‘knon0j’ as discussed above), but also the coupling constants (here the exchange coupling ‘AJ’) of the Hamiltonian.

In the ‘do 11’ loop the diagonal contributions of the Hamiltonian are applied to the input vector. This is a simple scalar multiplication. The more complicated step of applying the off-diagonal contributions to the input state is performed in two nested loops (‘do 21’ and ‘do 25’). While the outer loop goes through all rows of the matrix, the inner one goes through all ‘knon0j(m1)’ non-zero off-diagonal elements per row ‘m1’. It is instructive to have Fig.2.5 in mind when reading this subroutine. Since only the upper-right triangle of the Hamiltonian matrix is stored there have to be two multiplications, one yielding the contributions from the upper-right triangle ($y(m1)=y(m1)+AJ*hj(icounj)*q(jcol)$) and the ones from the hermitian lower-left triangle ($y(jcol)=y(jcol)+AJ*conjg(hj(icounj))*q(m1)$).

To understand the rapid convergence to the ground state which is obtained using the Lanczos algorithm, it is convenient to consider a variation of this technique known as the “modified” Lanczos method.[28] In this method, the diagonalization proceeds using “ 2×2 steps” i.e. first the Hamiltonian in the basis $|\phi_0\rangle$ and $|\phi_1\rangle$ (defined above) is diagonalized. The lowest energy state is always a better approximation to the actual ground state than $|\phi_0\rangle$. This new improved state can be used as the initial state of another 2×2 iteration, and the procedure is repeated as many times as needed, until enough accuracy has been reached. Then, it is clear that the modified Lanczos method, or the original Lanczos, can be described as a systematic way to improve a given variational state that is used to represent the ground state of the system, and thus it is not surprising that ground state properties can be obtained accurately well before the rest of the matrix eigenvalues are evaluated.

In the modified Lanczos method the ground state is always explicitly at hand. While this technique converges more slowly to the ground state than the standard

Lanczos method, the latter needs to be run twice to get the ground state explicitly. Thus, in some cases it is easier to use the modified Lanczos approach which is somewhat simpler to program. An even more pedestrian technique is the power method which consists of applying the Hamiltonian n -times to the initial state until all excited states are filtered out. For very simple problems this method may be sufficient, and it is easy to program.

2.5 Calculating Expectation Values

The strength of the Lanczos method lies not only in the arbitrarily precise numerical evaluation of the energy levels for a given physical system but also their corresponding eigenstates. This enables us to evaluate the expectation value for any operator of interest, in particular off-diagonal correlation functions which are often not accessible to Quantum Monte Carlo simulations due to statistical errors intrinsic to the method.

At this point we want to caution the reader about the convergence of the Lanczos method presented in the previous sections. In general, the coefficients of the eigenstates converge roughly 2-3 orders of magnitude more slowly than the corresponding eigenvalues. Thus, if a certain minimum difference in energy eigenvalues between two Lanczos steps, say $\Delta(E_{i+1} - E_i) \simeq 10^{-12}$, is chosen as a cut-off criterion for the Lanczos procedure, the corresponding eigenstate has not converged to an equivalent precision, e.g. $\Delta(c_{i+1}^\alpha - c_i^\alpha) \simeq 10^{-9}$ where $|\Psi_i\rangle = \sum_\alpha c_i^\alpha |\alpha\rangle$ and the index 'i' denotes the respective Lanczos iteration step.

Averages of interest are typically spin-spin correlations (e.g. $\langle S_i^z S_j^z \rangle$), charge-density correlations (e.g. $\langle n_i n_j \rangle$) and combinations thereof. Unfortunately, for

finite systems with an intrinsic continuous symmetry, such as for the Heisenberg, the XY, and the t-J Hamiltonian, the expectation value of the order parameter - e.g. the staggered magnetization at a given site $\langle S_j^z \rangle$ - vanishes, although this is not true for the bulk limit ($N \rightarrow \infty$) if an external staggered field h is used and if the limit $h \rightarrow \infty$ is taken after $N \rightarrow \infty$. In these cases, where the order parameter cannot be determined directly, one needs to study the finite scaling behavior of the corresponding correlation function ($\langle S_i^z S_j^z \rangle$) to extract the correlation length and the ordered moment.

Taking diagonal averages, which determine the projection of an operator on a state, is a very easy procedure once the ground state is obtained, since it only exploits computational concepts which have been already discussed. On the other hand, off-diagonal averages which connect different states of the same subspace (e.g. $\langle c_i^\dagger c_j \rangle$ where i and j are site indices) are more delicate since they require searching. They will be discussed in the next section.

In the following, we will discuss a short routine which calculates the diagonal spin-spin correlation function 'avspincorrel' for a system with 'ns' sites and ground state vector 'xf'. The 'nclass' representatives 'idw0' are also input parameters. The correlations are measured with respect to an arbitrarily chosen site, here : icentr=1. The spin-autocorrelation 'avspincorrel(1)' gives the on-site correlation at site 'icentr=1', the nearest-neighbor correlations 'avspincorrel(2)' and 'avspincorrel(ns)' (the later one comes in through periodicity for the linear case) give the average relative spin orientation between sites '1' and '2' ('1' and 'ns'), etc. . The important sequence which determines whether there is a spin-down or a spin-up at site 'il' for a given basis state idw1(kt) is given by the logical operation

`nsd=and(rshift(idw1(kt),i1),1)`. 'nsd' will be '1' if there is a spin-down at site 'i1' and zero if the spin is down.

A small additional complication enters this routine since it is written for the general case where symmetries are exploited. Thus for each representative 'idw0' the corresponding 'nclassmember' members of the class represented by 'idw0' have to be found first. (This happens in the call for the subroutine 'symlin'.) Then, in an inner loop ('do 26') each individual basis state 'idw1' is acted upon by the correlation operator as discussed above.

```

c      This subroutine calculates diagonal spin-spin correlation functions
c      ns : cluster size, nclass : number of classes
c      xf : coefficients of the ground state vector, idw0 : representatives of the
c      basis states
c      avspincorrel : averaged spin-spin correlation functions
c      The dimensions chosen here are for a 4-site lattice
c      with less than 10 states

      subroutine averag(ns,nclass,xf,avspincorrel,idw0)

      complex xf(10)
      real avspincorrel(4),spincorrel(4)
      integer idw1(10),idw0(10),nsv(4)

      icentr=1
      do jv=1,ns
        avspincorrel(jv)=0.0
      end do

c
c      loop over classes
c
      do 25 ks=1,nclass
        xfsquared=xf(ks)*conjg(xf(ks))
        jdww=idw0(ks)
        call symlin(jdww,idw1,nclassmember,itouch,signr,signi)
        do js=1,ns
          spincorrel(js)=0.0
        end do
      end do
c

```

```

c          loop over members of each class
c
          do 26 kt=1,nclassmember
            do jv=1,ns
              il=jv-1
              nsd=and(rshift(idw1(kt),il),1)
              nsv(jv)=2*nsd-1
            end do
            do jv=1,ns
              spincorrel(jv)=spincorrel(jv)+nsv(jv)*nsv(icentr)
            end do
26      continue
          xfsquared=xfsquared/nclassmember
          do jv=1,ns
            avspincorrel(jv)=avspincorrel(jv)+spincorrel(jv)*xfsquared
          end do
25 continue
        return
      end

```

The two major loops in this short routine are an outer loop over the class representatives ('do 25') and an inner loop over all the members of a given class ('do 26'). In the inner loop, the spin orientations for each site of a given basis state 'idw1' are temporarily tabulated in the variable 'nsv(jv)' where 'jv' is an index which refers to the distance relative to the reference site centered at 'icentr'. 'nsv(jv)' can assume the values '1' or '-1' corresponding to a spin-down or a spin-up at distance 'jv' from 'icentr'. The contribution to the 'jv -1'th-neighbor spin-spin correlation function from a given basis state 'idw1' is then added to a temporary vector 'spincorrel' in the line : `spincorrel(jv)=spincorrel(jv)+nsv(jv)*nsv(icentr)`. The weight associated with each of these contributions is determined by the square of the corresponding coefficient 'xf(ks)' for each basis element 'idw1(kt)' in the ground state. This can be

visualised by using the variables of the above example in writing the ground state :

$$\begin{aligned}
 |\Psi_{gs}\rangle &= \sum_{ks=1}^{n_{\text{class}}} \text{xf}(ks) |\text{idw0}(ks)\rangle \quad (\rightarrow \text{do 25 loop}) \\
 |\text{idw0}(ks)\rangle &= \frac{1}{n_{\text{classmember}}} \sum_{kt=1}^{n_{\text{classmember}}} |\text{idw1}(kt)\rangle \quad (\rightarrow \text{do 26 loop}). \quad (2.11)
 \end{aligned}$$

The spin-spin operator $S_i^z S_j^z$ acts on each $|\text{idw1}(kt)\rangle$ within the inner loop, and its contributions are temporarily stored in 'spincorrel'. The respective weight of the contribution of each individual basis state to the overall average is provided by multiplying 'spincorrel' by the quantity 'xfsquared' ($= \text{xf}(ks) * \text{conjg}(\text{xf}(ks)) / n_{\text{classmember}}$), e.g.

$$\begin{aligned}
 \langle \Psi_{gs} | S_i^z S_j^z | \Psi_{gs} \rangle &= \sum_{ks=1}^{n_{\text{class}}} \sum_{kt=1}^{n_{\text{classmember}}} \frac{\text{xf}(ks) * \text{conjg}(\text{xf}(ks))}{n_{\text{classmember}}} \\
 &* \langle \text{idw1}(kt) | S_i^z S_j^z | \text{idw1}(kt) \rangle. \quad (2.12)
 \end{aligned}$$

The overall normalization in the above subroutine was chosen such that the autocorrelations (i.e. $i=j$) are equal to one. However, for real spin-1/2 operators there should be an overall factor of 1/4 multiplying the correlation functions produced in this routine.

The above procedure can be easily modified for any diagonal averages, e.g. density-density correlations. This particular correlation is of interest for systems with mobile particles, like e.g. the Hubbard or the t-J model. The only essential ingredient to change in this case, is to create a hole-density operator instead of a spin-density operator (here : $\text{nsv}(jv)=2*\text{nsd}-1$). In a system of moving spin-1/2 particles there can be 4 possible states per site : spin-up, spin-down, both a spin-up and a spin-down, or a hole. However, in the t-J model, the double occupied state is discarded since it costs too much energy. To create a hole-density operator, we

need to know the spin configuration at each site, i.e. there should be two lines (i.e. $nsu = \text{and}(\text{rshift}(\text{jup}, i1), 1)$, $nsd = \text{and}(\text{rshift}(\text{jdw}, i1), 1)$) probing the up and down configurations respectively. Then, for the t-J model the hole-density operator probing a given site is given by : $1 - (nsu - nsd)^2$.

Finally, for the isotropic Heisenberg model there is a good test to check whether the spin-spin correlation functions have been computed correctly using the equality

$$E_{gs} = \langle J \sum_{\langle ij \rangle} \mathbf{S}_i \cdot \mathbf{S}_j \rangle = 3JNl \langle S_i^z S_j^z \rangle, \quad (2.13)$$

where i and j denote nearest neighbor sites, and Nl is the number of links or bonds. Thus, the ground state energy of the system is proportional to the nearest neighbor correlations in this particular case. This correlation must be translationally invariant, i.e. it should only depend on the distance between i and j rather than on the actual value of i .

2.6 Dynamical Properties

The greatest advantage of the Lanczos method over other numerical approaches is the accurate determination of dynamical correlation functions for a given finite system.[29] The Quantum Monte Carlo technique is, unfortunately, not suitable to extract this information since the simulations are carried out in imaginary time. Then, currently the Lanczos approach is the only reliable technique to evaluate dynamical responses in a controlled way (of course, with the restriction of working on small clusters). Finally, we will set-up the main formalism. In general, we are interested in calculating quantities like,

$$I(\mathbf{q}, \omega) = -\frac{1}{\pi} \text{Im}[\langle \psi_0(\mathbf{k}) | \hat{O}_{-\mathbf{q}}^\dagger \frac{1}{\omega + E_0 + i\epsilon - \hat{H}} \hat{O}_{\mathbf{q}} | \psi_0(\mathbf{k}) \rangle], \quad (2.14)$$

where $\hat{O}_{\mathbf{q}}$ is the momentum-dependent operator that we are analyzing (which depends on the actual experimental set up under consideration), $|\psi_0(\mathbf{k})\rangle$ is the ground state of the Hamiltonian \hat{H} whose ground state energy is E_0 , its momentum is \mathbf{k} (although in most cases of interest $\mathbf{k} = 0$), ω is the frequency, and ϵ is a small (real) number introduced in the calculation to shift the poles of the Green's function into the complex plane. Introducing a complete basis, $\sum_n |\psi_n\rangle\langle\psi_n| = 1$, and using the identity $\frac{1}{x+i\epsilon} = P(\frac{1}{x}) - i\pi\delta(x)$, which is valid when $\epsilon \rightarrow 0$ (where x is real, and P denotes the principal part), we arrive to

$$I(\mathbf{q}, \omega) = \sum_n |\langle\psi_n(\mathbf{k} + \mathbf{q})|\hat{O}_{\mathbf{q}}|\psi_0(\mathbf{k})\rangle|^2 \delta(\omega - (E_n - E_0)), \quad (2.15)$$

which is the standard way to express the spectral decomposition of a given operator in terms of squared matrix elements multiplying the pole structure contained in the delta-functions. $|\psi_n(\mathbf{k} + \mathbf{q})\rangle$ can be selected as eigenvectors of the Hamiltonian with eigenvalues E_n and momentum $(\mathbf{k} + \mathbf{q})$. In practice, the δ -functions are smeared by a finite ϵ i.e. they are replaced by Lorentzians according to $\delta(x) \rightarrow \frac{1}{\pi} \frac{\epsilon}{x^2 + \epsilon^2}$.

In order to evaluate numerically Eq. (2.15), it is convenient to write the Hamiltonian matrix in a special basis. As before, we will apply the Lanczos method to write \hat{H} in a tridiagonal form but instead of starting the iterations with a random state, we choose

$$|\phi_0(\mathbf{k} + \mathbf{q})\rangle = \frac{\hat{O}_{\mathbf{q}}|\psi_0(\mathbf{k})\rangle}{\sqrt{\langle\psi_0(\mathbf{k})|\hat{O}_{-\mathbf{q}}^\dagger\hat{O}_{\mathbf{q}}|\psi_0(\mathbf{k})\rangle}}, \quad (2.16)$$

as the initial configuration for reasons that will become clear soon. Following Fulde (1991), consider the matrix $(z - \hat{H})$ and the identity $(z - \hat{H})(z - \hat{H})^{-1} = I$, where $z = \omega + E_0 + i\epsilon$. Decomposed in the basis $|\phi_n\rangle$ which is generated recursively from $|\phi_0\rangle$ via $|\phi_{n+1}\rangle = \hat{H}|\phi_n\rangle - \alpha_n|\phi_n\rangle - \beta_n^2|\phi_{n-1}\rangle$ with coefficients $\alpha_n = \frac{\langle\phi_n|\hat{H}|\phi_n\rangle}{\langle\phi_n|\phi_n\rangle}$, $\beta_n^2 =$

$\frac{\langle \phi_n | \phi_n \rangle}{\langle \phi_{n-1} | \phi_{n-1} \rangle}$, we arrive to $\sum_n (z - \hat{H})_{mn} (z - \hat{H})_{np}^{-1} = \delta_{mp}$. For the special case $p = 0$ we obtain, $\sum_n (z - \hat{H})_{mn} x_n = \delta_{m0}$, where $x_n = (z - \hat{H})_{n0}^{-1}$. This represents a system of equations for the unknown x_0 . The particular case of $n = 0$ corresponds to $\langle \phi_0 | \frac{1}{z - \hat{H}} | \phi_0 \rangle$ which is the quantity we want to study. Then, we need to solve this linear system of equations.

For this purpose we use Cramer's rule i.e. $x_0 = \frac{\det B_0}{\det(z - \hat{H})}$, where the matrices in the $\{|\phi_n\rangle\}$ basis are given by,

$$z - \hat{H} = \begin{pmatrix} z - a_0 & -b_1 & 0 & 0 & \dots \\ -b_1 & z - a_1 & -b_2 & 0 & \dots \\ 0 & -b_2 & z - a_2 & -b_3 & \dots \\ 0 & 0 & -b_3 & z - a_3 & \dots \\ \vdots & \vdots & \vdots & \vdots & \ddots \end{pmatrix}, \quad (2.17)$$

and

$$B_0 = \begin{pmatrix} 1 & -b_1 & 0 & 0 & \dots \\ 0 & z - a_1 & -b_2 & 0 & \dots \\ 0 & -b_2 & z - a_2 & -b_3 & \dots \\ 0 & 0 & -b_3 & z - a_3 & \dots \\ \vdots & \vdots & \vdots & \vdots & \ddots \end{pmatrix}, \quad (2.18)$$

where the coefficients a_n, b_n were defined above in the text. The determinants of these matrices are expanded as $\det(z - \hat{H}) = (z - a_0)\det D_1 - b_1^2 \det D_2$, and $\det B_0 = \det D_1$, where in general the matrix D_n is obtained from Eq.(2.17) by removing the first n rows and columns. Now, it can be easily shown that

$$x_0 = \frac{1}{z - a_0 - b_1^2 \frac{\det D_2}{\det D_1}}. \quad (2.19)$$

The ratio of determinants on the right hand side of Eq.(2.19) can also be expanded as

$$\frac{\det D_2}{\det D_1} = \frac{1}{z - a_1 - b_2^2 \frac{\det D_3}{\det D_2}}, \quad (2.20)$$

and the procedure can be repeated until a full continued fraction is constructed. Recalling the definition of the spectral intensity $I(\mathbf{q}, \omega)$, it can finally be shown that

$$I(\mathbf{q}, \omega) = -\frac{1}{\pi} \text{Im} \left[\frac{\langle \psi_0(\mathbf{k}) | \hat{O}_{-\mathbf{q}}^\dagger \hat{O}_{\mathbf{q}} | \psi_0(\mathbf{k}) \rangle}{z - a_0 - \frac{b_1^2}{z - a_1 - \frac{b_2^2}{z - a_2 - \dots}}} \right], \quad (2.21)$$

which establishes the relation between Eq.(2.14) and a continued fraction expansion. Recalling that $z = \omega + E_0 + i\epsilon$, we can then obtain the spectral function for any value of the frequency ω , the width ϵ , and knowing the ground state energy and momentum of the system. From the eigenvalues of the Hamiltonian in the special Lanczos basis obtained by iterating with the initial state Eq.(2.16) we can get very accurately the positions of the poles in the spectral function.

In practice, the best way to proceed in order to get the dynamical response of a finite cluster is in two steps. First, run the Lanczos subroutine using $|\phi_0(\mathbf{k} + \mathbf{q})\rangle$ as the initial state. It is clear that with this procedure we are testing the subspace of the Hilbert space in which we are interested, and thus all the states found in the Lanczos step will contribute to the spectral function (there will be as many poles as iterations are carried out, assuming that this number is smaller than the total size of the subspace being explored). Secondly, in order to find the intensity of each pole it is useful to recall that any energy *eigenvector* $|\psi_n(\mathbf{k})\rangle$ of the tridiagonal representation

of the Hamiltonian can be written as $|\psi_n(\mathbf{k})\rangle = \sum_m c_m^n |\phi_m(\mathbf{k})\rangle$, where $|\phi_m(\mathbf{k})\rangle$ are the orthonormalized vectors defined in the Lanczos procedure, with $|\phi_0(\mathbf{k})\rangle$ given by Eq.(2.16). Then, it can be easily shown that

$$|\langle \psi_n(\mathbf{k} + \mathbf{q}) | \hat{O}_{\mathbf{q}} | \psi_0(\mathbf{k}) \rangle|^2 = |c_o^n|^2 \langle \psi_0(\mathbf{k}) | \hat{O}_{-\mathbf{q}}^\dagger \hat{O}_{\mathbf{q}} | \psi_0(\mathbf{k}) \rangle, \quad (2.22)$$

and thus the intensity can be written in terms of the first component of each eigenvector obtained when the tridiagonal Hamiltonian matrix is diagonalized. In summary, the whole process simply amounts to a Lanczos run with a very particular initial state. To test the convergence of the procedure it is generally enough to plot the spectral function with a particular ϵ , and test by eye how the results evolve with the number of iterations. In addition, more sophisticated methods to terminate the iterations using terminating functions to approximate the asymptotic behavior of the coefficients a_n and b_n can be implemented to smoothen the spectral function.

Here, we present a subroutine ('inisp') which produces the seed state $|\phi_0(\mathbf{k} + \mathbf{q})\rangle = \sum_j \exp(i\mathbf{q} \cdot \mathbf{r}_j) S_{\mathbf{r}_j}^z |\psi_0(\mathbf{k})\rangle$, where $|\psi_0(\mathbf{k})\rangle$ is the ground state of the system obtained in a previous Lanczos run. The state $|\phi_0(\mathbf{k} + \mathbf{q})\rangle$ will be subsequently used as the input state for the Lanczos subroutine which yields the moments a_n and b_n . Later, we will also show a very simple routine which converts the a_n 's and b_n 's ($n=0, \dots, N$) into an N-pole dynamical correlation function.

We suggest for the computation of the dynamical correlation functions to create a program separate from the one which produces the ground state energy and wave function of the system under consideration. E.g. the coefficients of the ground state vector as well as the representatives of the basis classes should be written to files, say 'groundstate' and 'classes'. Then, in the program which determines the system dynamics these quantities are read in and acted upon N times with the

operator under consideration, here $S^z_{\mathbf{q}}$. The resulting vector is then passed to the Lanczos subroutine, where it is acted upon with the Hamiltonian. The components of the Hamiltonian matrix should be set up in the dynamics program using the same procedure (sequence of subroutines) as in the initial Lanczos program. Since the elements of the Hamiltonian matrix act on $|\phi_0(\mathbf{k} + \mathbf{q})\rangle$, here the matrix needs to be represented in a subspace corresponding to the quantum numbers of $|\phi_0(\mathbf{k} + \mathbf{q})\rangle$, i.e. the classes should have momentum $\mathbf{k} + \mathbf{q}$. Also, for operators different than $S^z_{\mathbf{q}}$, the state $|\phi_0(\mathbf{k} + \mathbf{q})\rangle$ may have a total spin and a total number of particles different from $|\psi_0(\mathbf{k})\rangle$, and the corresponding basis states have to be constructed accordingly.

The subroutines ‘search’ and ‘symlin’ called in the routine which is presented below have already been discussed in previous sections. However, we have here taken the liberty to modify ‘symlin’ slightly by making the translational wavenumber ‘jscth0’ (where $k = \frac{2\pi \cdot \text{jscth0}}{\text{ns}}$) an argument of the call instead of fixing it within the subroutine ‘symlin’.

```

c      In this subroutine the spin operator is applied to the ground state vector
c      ns : number of sites
c      nclas0 : number of classes in the basis of the ground state
c      nclas1 : number of classes in the basis of the final state, phi0 : final state
c      jscth1 : wave number of the spin operator, sclas1 : normalization for each
c      set of states in the basis of the final state
c      jscth0 : momentum of the ground state vector

      subroutine inispi(ns,nclas0,nclas1,phi0,jscth1,sclas1,jscth0)
      complex phi0(10),psi0
      real sclas1(10),signr(256),signi(256)
      integer idw1(256)

      open(unit=25,status='old',file='groundstate')
      open(unit=30,status='old',file='classes')
      pi = acos(-1.0)

```

```

do m1=1,nclas1
  phi0(m1) = cmplx(0.0,0.0)
end do

c
c      loop over classes of |psi0>
c
      do 20 m1=1,nclas0
        read(25,*)psi0
        read(30,*)idw0
        call symlin(jscth0,idw0,idw1,nclassmember,itouch,signr,signi)
        psi0 = psi0 / sqrt(float(nclassmember))

c
c      loop over members of a given class
c
        do 30 lc=1,nclassmember
          jbradw=idw1(lc)

c
c      acting with Sz on site j3
c
          do 40 j3=1,ns
            call search(jbradw,idw0,nclas1,itouch,my)
            if(itouch.ne.0)then
              nspin=2*and(rshift(jbradw,j3-1),1)-1
              phase = - 2.0 * pi * (j3-1) * jscth1 / ns
              preal = cos(phase)
              pimag = sin(phase)
              phi0(my) = phi0(my) +
1              cmplx(preal,pimag) * nspin * psi0 *
1              cmplx(signr(lc),signi(lc))
            endif
          40      continue
        30      continue
      20      continue

      do i=1,nclas1
        phi0(i)=phi0(i)*sclas1(i)
      end do

      close(unit=25)
      close(unit=30)

      return
      end

```

The above routine is written in a rather generic way such that it can be modified easily if there is interest in, e.g., the charge dynamics of the system. Again, we would like first to highlight the central logical operation, which here is the S^z_q operator acting on the basis state 'jbradw' : $nspin=2*\text{and}(\text{rshift}(\text{jbradw},j3-1),1)-1$, where 'j3' ($= 1,ns$) is a site index. For the particular case of spin-dynamics, this corresponding logical operation does not lead out of the subspace of $S^z_{tot} = 0$ and does not change the number of particles of the ground state 'psi0' when it acts on it. However, the number of class representatives of $|\psi_0(k)\rangle$ is not equal to the one for $|\phi_0(k + q)\rangle$ ($nclas1 \neq nclas0$), e.g. this quantity is momentum dependent.

In the case of hole dynamics, the corresponding logical operation is given by : $jnew=\text{xor}(\text{jbradw},2^{*(j3-1)})$. (This statement needs to be inserted right before the call for the searching subroutine, and 'jnew' replaces 'jbradw' as the input state for the search.) In contrast to the spin dynamics, this operation leads out of the subspace of $S^z_{tot} = 0$ into $|S^z_{tot}| = 1/2$ and decreases the number of particles by one. Then, $|\phi_0(k + q)\rangle$ can be only represented in a basis whose member states belong to the subspace of $|\phi_0(k + q)\rangle$ different from the basis for the initial state. Hence, the Hamiltonian matrix, which will be applied to $|\phi_0(k + q)\rangle$ in the subsequent Lanczos run to produce the dynamical moments also has to be represented in this new basis.

Let us now discuss the subroutine 'inisp' in detail. The only output variable is 'phi0' corresponding to the coefficients of the seed state $|\phi_0(k + q)\rangle$. Input variables are the number of sites ('ns') of the cluster, the number of classes of the subspace of $|\psi_0(k)\rangle$ ('nclas0'), the number of classes of the subspace of $|\phi_0(k + q)\rangle$ ('nclas1'), the momentum q of the operator S^z_q ('jscth1'), the square root of the number of

members for each class in the subspace of $|\phi_0(\mathbf{k} + \mathbf{q})\rangle$ ('sclas1'), and the momentum of the initial state $|\psi_0(\mathbf{k})\rangle$ ('jscth0'). The parameters 'nclas1' and 'sclas1' can be obtained by running the subroutine 'initl' for the subspace of $|\phi_0(\mathbf{k} + \mathbf{q})\rangle$ first. This subroutine is also a prerequisite to set up the Hamiltonian matrix in the basis of $|\phi_0(\mathbf{k} + \mathbf{q})\rangle$ which is done in 'smatel'.

There are three nested loops in the subroutine 'inispi' corresponding to the sum over classes of $\psi_0(\mathbf{k})$ ('do 20'), the sum over all 'nclassmember' members for a given class ('do 30'), and to the Fourier transform of the spatial S^z operator with momentum \mathbf{q} ('do 40'). After a class representative 'idw0' and its coefficient 'psi0' for the ground state vector $\psi_0(\mathbf{k})$ are read in from file, the corresponding members for the class represented by 'idw0' are generated along with their respective phases 'isignr' and 'isigni' in the subroutine 'symlin'. Since the S^z operator is applied to each basis state individually there is a loop over all 'nclassmember' states represented by 'idw0'. Finally, in the innermost loop the S^z operator acts on each site resulting in $n_{\text{spin}} = \pm 1$ depending on the spin orientation at site 'j3-1'. It also picks up a 'phase' $(= -2.0 * \pi * (j3-1) * \text{jscth})$ corresponding to the position of the spin in the cluster. Since $S^z_{\mathbf{q}}$ is a diagonal operator, the state it acts on ('jbradw') stays unchanged. Then, 'jbradw' enters the call for the search routine which allows only representatives of a given class in the new subspace of $|\phi_0(\mathbf{k} + \mathbf{q})\rangle$ to contribute to the coefficients of $|\phi_0(\mathbf{k} + \mathbf{q})\rangle$ ('phi0'). However, for off-diagonal operators, such as the hole operator discussed above or spin operators S^{\pm} , the basis state which is acted upon is changed into another one. That new state is then the one which enters the call for the search subroutine instead of 'jbradw'. The if-statement following the call for the search routine guaranties that only the 'nclas1' contributions to $|\phi_0(\mathbf{k} + \mathbf{q})\rangle$ corresponding

to the actions of the operator on the initial state are included in the coefficients ‘phi0(my)’. Here ‘my’ is the output index of the search routine labeling the position of the class representative which is multiplied by the coefficient ‘phi0(my)’.

Again, it might be helpful to write the loops which occur in ‘inispi’ as three separate sums in terms of the symbols used in this subroutine, e.g.

$$\begin{aligned}
 |\text{phi0}\rangle &= \sum_{m1=1}^{\text{nclas0}} \frac{\text{psi0}_{m1}}{\text{nclassmember}} \sum_{lc=1}^{\text{nclassmember}} \sum_{j3=1}^{\text{ns}} \exp(i \cdot 2 \cdot \pi \cdot \text{jscth1} \cdot (j3 - 1) / \text{ns}) \times \\
 &\times S_{j3-1}^z |\text{idw1}(lc)\rangle,
 \end{aligned} \tag{2.23}$$

where psi0_{m1} is the state ‘psi0’ corresponding to class ‘m1’, and

$$\sum_{m1=1}^{\text{nclas0}} (\rightarrow \text{do } 20), \quad \sum_{lc=1}^{\text{nclassmember}} (\rightarrow \text{do } 30), \quad \sum_{j3=1}^{\text{ns}} (\rightarrow \text{do } 40). \tag{2.24}$$

As a final comment on the subroutine ‘inispi’ we want to indicate that it is suitable to produce off-diagonal static averages for a given operator which leads out of the subspace of $\psi_0(\mathbf{k})$, i.e. $\langle S_i^+ S_j^- + S_i^- S_j^+ \rangle$ or $\langle c_i^\dagger c_j \rangle$. The modification which needs to be applied to the above subroutine is to store the contributions to ‘phi0’ from different pairs $\langle i, j \rangle$ separately, e.g. ‘phi0(my)’ \rightarrow ‘phi0(j3,my)’. Once all ‘phi0(j3,my)’ have been obtained the corresponding off-diagonal correlations can be generated by adding three nested loops at the end of the routine, e.g.

```

do 32 l1 = 1,ns
do 32 l2 = 1,ns
do 31 m1 = 1,nclas1
corr(l1,l2) = corr(l1,l2) + phi0(l1,m1)*conjg(phi0(l2,m1))
31 continue
32 continue

```

Now, we turn to the final subroutine ‘strucfac’ which converts the moments a_n and b_n into dynamical correlation functions using Eq. (2.21). It is here assumed that these moments have been produced by applying Lanczos iterations to the seed state

$|\phi_0(\mathbf{k} + \mathbf{q})\rangle$ as discussed above. In 'strucfac' the Green's function 'green', $G(\mathbf{q}, \omega)$, is constructed recursively from the a_n 's and b_n 's. Then, the imaginary part is taken to produce the corresponding dynamical observable. This program is absolutely generic and independent of what dynamical quantity is calculated.

The only output parameter of this routine is the frequency dependent dynamical correlation function 'dyncorrel'. Input parameters are the number of cluster sites 'ns', the ground state energy 'gsenergy' of the system obtained in the initial Lanczos run, the moments a_n and b_n (here : 'an' and 'bn'), and the number of Lanczos iterations 'itm' which have been applied to the seed state in the Lanczos subroutine of the dynamics program.

```

c      This subroutine converts the moments 'an' and 'bn' into a frequency dependent
c      correlation function
c      ns : number of sites, dyncorrel : dynamic correlation function
c      gsenergy : ground state energy, an,bn : moments produced in 'lancsz'
c      itm : number of poles, omega : energy transfer

      subroutine strucfac(ns,dyncorrel,gsenergy,an,bn,itm)
      real dyncorrel(800),an(250),bn(250)
      complex x,green

      epsilon=0.1
      omega=-4.0
      pi=acos(-1.0)
      do 20 i=1,800
        x=-omega+cmplx(0.,1.)*epsilon +gsenergy
        green=1/(x-an(itm))
        do j=(itm-1),1,-1
          green=1.0/(x-an(j)-green*((bn(j+1))**2))
        end do
        dyncorrel(i)=bn(1)*bn(1)*dimag(green)/(ns*pi)
        omega=omega+0.01
20    continue

      return
      end

```

Here, frequencies are measured with respect to the ground state energy ‘gsenergy’ which resembles the experimental situation (e.g. Neutron scattering in the case of spin dynamics) where the energies measured are actually energy differences, or better *energy transfers*, between the ground state and excited states to which the operator (here $S^z_{\mathbf{q}}$) couples. The same holds for the momenta: \mathbf{q} is the *momentum transfer* between the ground state (with momentum \mathbf{k}) and all excited states (with momentum $\mathbf{k} + \mathbf{q}$). The excited states with momentum $\mathbf{k} + \mathbf{q}$ are not necessarily degenerate, since they may differ in various other quantum numbers, like e.g. spin-rotation, spin-inversion, spatial parity

Let us shortly discuss the details of the subroutine ‘strucfac’. The poles in the Green’s function (Eq. (2.15)) are replaced by Lorentzians of the form $\delta(\omega) \rightarrow \frac{1}{\pi} \frac{\epsilon}{\omega^2 + \epsilon^2}$ with a half-width given by ‘epsilon’. ‘epsilon’ can be adjusted to make the spectrum sharper or smoother. Typically, a broadening of 10 – 25% of the unit of energy (e.g. t or J in the t - J model) is used. In this context it is important to keep the frequency steps ($\omega = \omega + 0.01$) about an order of magnitude smaller than ‘epsilon’ to guaranty that no precision is lost in ω -space.

There are two nested loops in ‘strucfac’. The outer loop (‘do 20’) goes through the arbitrarily closely spaced frequency steps. Here, we have chosen steps of ‘0.01J’. In principle, there is no limit in this method to the resolution in ω -space. The “coarseness” of the discretization in ω should be chosen in balance with the ‘epsilon’ value as discussed in the previous paragraph. In the inner loop, the $a_n - b_n$ representation of the Green’s function (Eq. (2.21)) for a given frequency is built up iteratively starting with the highest pole and going backwards ($\text{green} = 1.0 / (x - a_n(j) - \text{green} * ((b_n(j+1))^{**2}))$). Then, the imaginary part of this function is taken

subsequently in the outer loop, and weighted with the factor $\text{bn}(1)^*\text{bn}(1)$ which corresponds to the numerator in Eq. (2.21). This procedure is repeated for each ω -step.

Sometimes it is necessary to calculate moments of the distribution $I(\mathbf{q}, \omega)$. This can be done very easily. For example, the integral over frequency of the spectral function gives,

$$\int_0^\infty d\omega I(\mathbf{q}, \omega) = \sum_n |\langle \psi_n(\mathbf{k} + \mathbf{q}) | \hat{O}_{\mathbf{q}} | \psi_0(\mathbf{k}) \rangle|^2 = \langle \psi_0(\mathbf{k}) | \hat{O}_{-\mathbf{q}}^\dagger \hat{O}_{\mathbf{q}} | \psi_0(\mathbf{k}) \rangle, \quad (2.25)$$

where we have assumed that the eigenvectors of the Hamiltonian are normalized to one, i.e. $\sum_n |c_0^n|^2 = 1$. Eq.(2.25) is a generic expression for some of the “sum-rules” frequently mentioned in the literature for various operators $\hat{O}_{\mathbf{q}}$. Let us for example consider the sum-rules for the spin operator $\hat{O}_{\mathbf{q}} = S^z(\mathbf{q}) = \sum_j \exp(-i\mathbf{q} \cdot \mathbf{r}_j) S^z_{\mathbf{r}_j}$:

$$\int S^{\alpha\alpha}(\mathbf{q}, \omega) d\omega = \pi \langle S^\alpha(\mathbf{q}) S^\alpha(-\mathbf{q}) \rangle, \quad (2.26)$$

$$\int S^{\alpha\alpha}(\mathbf{q}, \omega) \omega^{-1} d\omega = \frac{\pi}{2} \chi(\mathbf{q}), \quad (2.27)$$

$$\int S^{\alpha\alpha}(\mathbf{q}, \omega) \omega d\omega = \pi \langle [S^\alpha(\mathbf{q}), H] S^\alpha(-\mathbf{q}) \rangle, \quad (2.28)$$

where the $\alpha=x,y,z$ refers to the spin components, and $S^{\alpha\alpha}(\mathbf{q}, \omega)$ represents $I(\mathbf{q}, \omega)$ for the special case of the spin operator..

These sum-rules serve as a nontrivial check to verify whether the dynamic correlation functions have been obtained correctly. E.g. for the Heisenberg chain the sum-rule for the static spin-spin correlation functions gives $S^{zz}(\mathbf{q}) = \sum_{j=1}^N \exp(i\pi \mathbf{r}_j) \langle S_0^z S_{\mathbf{r}_j}^z \rangle = \frac{1}{\pi} \int S^{zz}(\mathbf{q}, \omega) d\omega$ as we will verify below for a finite cluster. Naturally, there are very similar sum-rules associated with every dynamic correlation function of interest such as the optical conductivity or the spectral function.

Let us now consider the example of a 16-site spin-1/2 Heisenberg chain with periodic boundary conditions ($S_{N+1} = S_1$) to illustrate the use of the routines presented above and to show that the sum-rule for the spin structure factor works. In Fig. 2.7 we show (a) the real-space spin-spin correlations, (b) the Fourier transform of this quantity, which is the static spin structure factor, and finally (c) the dynamical spin-structure factor for this particular cluster.

In Fig. 2.7(a), we observe spin correlations that are typical for an antiferromagnetically ordered phase, i.e. with sign changes as a function of distance indicating a tendency towards $|\uparrow\downarrow\uparrow\downarrow\uparrow\downarrow \dots\rangle$ -ordering. Notice, however, that we do not have the strict Néel order ($\langle S_i^z S_j^z \rangle = \frac{1}{4}(-1)^{i-j}$) observed for the Ising model, but rather a power-law decay of the form $\langle S_i^z S_j^z \rangle \propto (-1)^{i-j}/|i-j|$ (actually there are small logarithmic corrections to this behavior).

In Fig. 2.7(b), the Fourier transform of the real-space spin-spin correlations is shown. It is clearly peaked at $q = \pi$ which is the antiferromagnetic wave vector in one dimension. This peak at $q = \pi$ indicates the dominant presence of ‘backscattering’ processes which give rise to antiferromagnetic instabilities.

Finally, in Fig. 2.7(c) we show the dynamical structure factor for the 16-site chain. This quantity is momentum and frequency dependent. In the continued fraction expansion, $S(q, \omega)$ has been given a finite frequency broadening of $\delta = 0.1J$. As can be seen from this figure, there are always a finite number of discrete peaks for a finite lattice, even if in the bulk limit a continuous density of states is expected as is the case for the spin-1/2 Heisenberg chain. Thus, only by looking at the dynamical structure factor on lattices of increasing length (finite scaling analysis) we can tell whether there should be a continuum in frequency space in the thermodynamic limit.

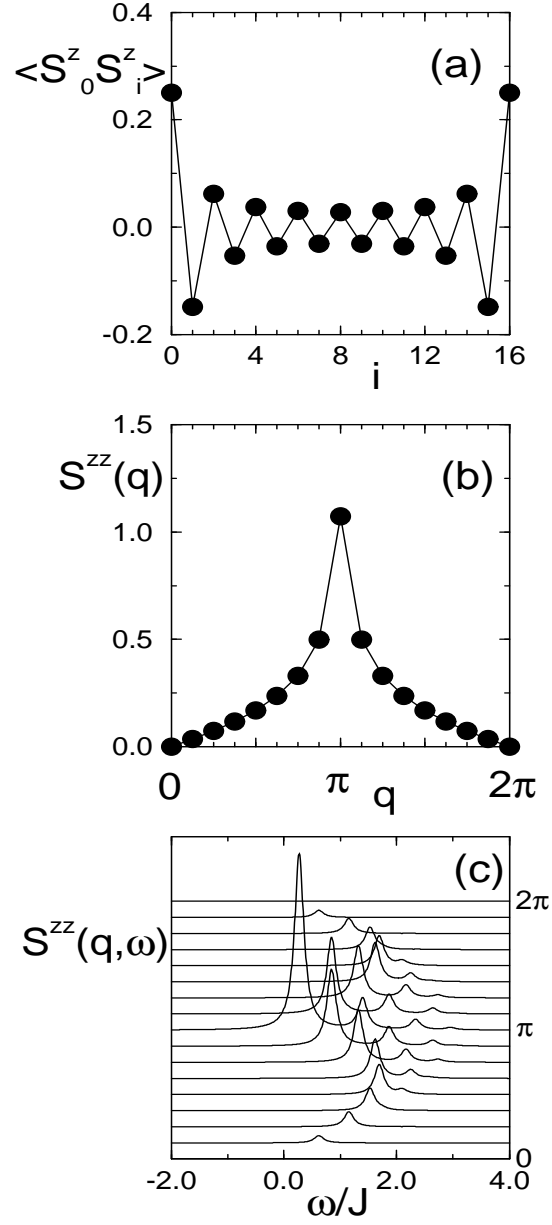


Figure 2.7: Spin correlation functions for the 16-site spin-1/2 Heisenberg chain. (a) z-component of the real-space spin-spin correlation function, (b) static spin structure factor in momentum space, (c) dynamical spin-structure factor.

Indeed, for the spin-1/2 Heisenberg chain we found that, e.g. in $S^{zz}(q = \pi, \omega)$, there are $N/4$ dominant poles for an N -site chain. Thus, in the bulk ($N \rightarrow \infty$) there will be an infinite number of infinitesimally narrow spaced poles for this quantity.

Table 2.2: Real-space spin-spin correlation functions and their Fourier transforms for the 16-site spin-1/2 Heisenberg chain

i	$\langle S_0^z S_i^z \rangle$	q	$S^{zz}(q) = \frac{1}{\pi} \int S^{zz}(q, \omega) d\omega$
0	0.25	0	0
1	-0.149	$\pi/8$	0.036
2	0.062	$\pi/4$	0.075
3	-0.053	$3\pi/8$	0.118
4	0.038	$\pi/2$	0.17
5	-0.036	$5\pi/8$	0.236
6	0.03	$3\pi/4$	0.331
7	-0.031	$7\pi/8$	0.498
8	0.028	π	1.073

The reader is cautioned that for one-dimensional systems with a continuous symmetry - like the plain Heisenberg model - there is no long-range order in the strict sense, since all correlation functions *decay* to zero. However, in this particular case they decay very slowly (as a power law with distance), and thus we can speak of *quasi long-range order*. In table 2.2 we list the numerical values for the spin-spin correlation functions and their Fourier transforms. As can be seen by integrating

the dynamical structure factor shown in Fig. 2.7(c) over all ω -space, the sum-rules given in Eq. 2.26 are satisfied.

Another useful check to determine whether the dynamic correlations have been generated accurately is the position of the first excited state in ω -space, e.g. the position of the first peak in the spectrum (Fig. 2.7(c)). The ω -value of the lowest peak should be located precisely at the difference between the lowest energy eigenvalue at momentum $\mathbf{k} + \mathbf{q}$ and the ground state energy, i.e. $\omega = E_{\mathbf{k}+\mathbf{q}}^0 - E_{\mathbf{k}}^0$, where \mathbf{k} is the ground state momentum, and \mathbf{q} is the momentum of the dynamic operator.

Due to the finite size of the clusters which can be studied numerically, there is always a gap at the bottom of the spectrum for a finite cluster. It then becomes crucial to study the scaling of this gap with system size in order to determine whether there is a finite correlation length associated with the system.

If higher moments of the distribution are needed, the following relation holds,

$$\int_0^\infty d\omega \omega^p I(\mathbf{q}, \omega) = \langle \psi_0(\mathbf{k}) | \hat{O}_{-\mathbf{q}}^\dagger \hat{O}_{\mathbf{q}} | \psi_0(\mathbf{k}) \rangle \sum_n |c_0^n|^2 (E_n - E_0)^p, \quad (2.29)$$

where all the necessary information to calculate it was obtained before when the spectral function was evaluated (poles and intensities) .

2.7 Conclusions

To end this section about the Lanczos method, we will describe a recent attempt to increase the size of the clusters that this technique can reach. The idea is that for some particular cases it may occur that the wave function of the ground state expanded in some working basis that is selected for the problem (schematically $|\psi_0(\mathbf{k})\rangle = \sum_m c_m |m\rangle$), may contain states with very small weight c_m . Then, it could

be possible to neglect those states in the basis, and still get accurate enough results for the ground state properties. These types of ideas (that we call “truncation” method) have been recently used in Quantum Chemistry by Wenzel and Wilson[32] and in the context of correlated electrons by Riera and Dagotto[33]. For the particular case of the $t - J_z$ model the approach works very well, and clusters of 50 sites can be easily studied keeping only a few hundred thousand states in the basis (which is a negligible percentage of the total basis set size). However, when the method is applied to the $t - J$ model its convergence to the ground state energy becomes slow (logarithmic) as the size of the basis is increased. To describe properly the strong quantum fluctuations of the spin background most of the S^z -basis is needed. Then, the truncation technique is very accurate for particular Hamiltonians while for others it only provides a rough estimation of the ground state properties. This approach should be seriously considered every time a new problem that needs computational work appears. In particular, it seems suitable for problems with gaps in the spectrum (like a spin-gap).

CHAPTER 3

ANTIFERROMAGNETICALLY INDUCED PHOTOEMISSION

BAND IN THE CUPRATES

A consequence of strong antiferromagnetic (AF) correlations in models of high critical temperature (high- T_c) cuprates is the appearance of quasiparticle-like features in photoemission (PES) calculations above the Fermi momentum p_F which would correspond to weakly interacting electrons. This effect, discussed before by Kampf and Schrieffer (Phys. Rev. B 41, 6399 (1990)) using diagrammatic techniques, is analyzed in this chapter using computational techniques in the strong coupling regime. It is concluded that weight above p_F should be observable in experimental PES ($\omega < 0$) data for underdoped high- T_c cuprates, while in the overdoped regime it will be likely hidden in the experimental background. In the intermediate doping region the signal is weak and at the verge of observability. The order of magnitude of our results is thus compatible with recent experimental data by Aebi et al. (Phys. Rev. Lett. 72, 2757 (1994)) for Bi2212 at optimal doping. The results described in this section have been published by S. Haas, A. Moreo, and E. Dagotto in Phys. Rev. Lett. 74, 4281 (1995).

3.1 Magnetic Correlations in High- T_c Compounds

The importance of AF correlations in the normal and superconducting states of the high- T_c cuprate materials is under much discussion. While recently most

of the debate has concentrated on the symmetry of the superconducting order parameter, studies of the strength of the AF correlation length, ξ_{AF} , in the normal state are still crucial to test these ideas. A key issue is how large ξ_{AF} should be to produce observable effects in experiments for the high-Tc compounds. NMR studies in the normal state of optimally doped $\text{YBa}_2\text{Cu}_3\text{O}_{6.94}$ (YBCO) suggest $\xi_{AF} \sim 2a$ (where a is the lattice spacing).[34] Naively, this correlation seems too small to be of relevance. On the other hand, recent PES experimental results by Aebi et al.[35] on $\text{Bi}_2\text{Sr}_2\text{CaCu}_2\text{O}_8$ (Bi2212) at $T_c=85\text{K}$, using sequential angle-scanning data acquisition to obtain PES intensities within a narrow energy window near the Fermi energy E_F , have been reported to provide evidence for antiferromagnetically induced spectral weight above p_F ($\omega < 0$). Are these two results compatible?

To analyze Aebi et al.'s interpretation of their PES data, let us recall the intuitive physics involved. At half-filling, the magnetic unit cell of the CuO_2 planes is enlarged by the long range AF order in the ground state. This effective reduction in the size of the Brillouin zone (BZ) has interesting implications for PES experiments, as was discussed by Kampf and Schrieffer as part of their “shadow band” scenario.[56] For example, along the diagonal $p_x = p_y = p$, and assuming long-range order, the quasiparticle-like peaks at the top of the valence band and at momenta $\mathbf{p}_1 = (p, p)$ and $\mathbf{p}_2 = (\pi - p, \pi - p)$ should appear at the same energy location, for any value of p . The coherent PES peaks observed *above* p_F are induced by strong correlations and do not exist for weakly interacting fermions.[56]

How does this antiferromagnetically induced PES signal evolve as ξ_{AF} is made finite by the effect of hole doping? It is likely that its intensity will smoothly diminish when the system is doped away from half-filling. Since in optimally doped Bi2212

the AF correlation length in the CuO_2 planes should be similar to that of optimally doped YBCO (because they should have the same in-plane hole density), a natural question arises: can a small correlation length ($\sim 2a$) produce observable weight in PES experiments above p_F comparable to those reported by Aebi et al.[35]? On one hand, recent calculations[37] carried out in an AF background, which reproduced the flat band features near $\mathbf{p} = (\pi, 0)$ observed in Bi2212, suggest that a short ξ_{AF} can appreciably influence some experimental quantities. On the other hand, since the actual experimental PES signal for Bi2212 (Fig. 3.1) is weak, concerns may arise about the interpretation of the data. Thus, a theoretical *quantitative* calculation in strong coupling is needed to compare PES spectra and ξ_{AF} with experiments, and to decide whether Aebi et al.'s PES data are compatible with models of correlated electrons having PES weight above p_F .

3.2 $A(\mathbf{p}, \omega)$ for the Hubbard Model

Here, this issue is explicitly addressed. PES spectra and spin correlations are calculated for electronic models expected to describe the CuO_2 planes. Consider first the standard two dimensional (2D) one band Hubbard model

$$H = -t \sum_{\langle \mathbf{i}, \mathbf{j} \rangle \sigma} (c_{\mathbf{i}\sigma}^\dagger c_{\mathbf{j}\sigma} + \text{h.c.}) + U \sum_{\mathbf{i}} n_{\mathbf{i}\uparrow} n_{\mathbf{i}\downarrow}, \quad (3.1)$$

in the standard notation.

We simulated this model numerically using Quantum Monte Carlo (QMC) techniques. In order to extract the dynamical spectral function $A(\mathbf{p}, \omega)$ corresponding to the removal or addition of an electron with momentum \mathbf{p} to the system, the maximum entropy (ME) technique was used.[39] We remark that using this low-resolution

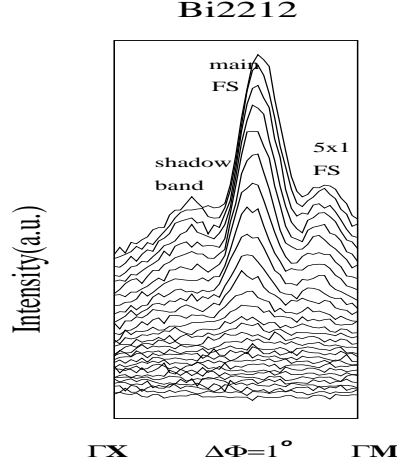


Figure 3.1: PES intensity in Bi2212, as reported by Osterwalder et al. (Ref.[35]). Their method produces PES intensity at constant energy for all momenta, while conventional methods provide complete PES energy distribution curves at a few locations in the BZ. Each solid line corresponds to a fixed energy scan starting at the bottom at 0.3 eV above E_F , and arriving at the last top line at E_F . The spectra were measured at a polar angle of 39° , and for azimuthal angles spaced 1° apart beginning near the ΓM line and ending near the ΓX line. The “ 5×1 ” band is explained in the original text Ref.[35] and it is of no concern to us. We thank P. Aebi and J. Osterwalder for providing us with these unpublished data.

method we will not be able to distinguish between sharp quasiparticle-like peaks located at the top of the valence band, from the robust incoherent contribution to $A(\mathbf{p}, \omega)$. Thus, in this discussion of the 2D Hubbard model only the strength of the spin correlations, and their influence on the integrated PES signal will be addressed. This signal is calculated from the percentage of spectral weight below the chemical potential μ at momenta along the diagonal $p_x = p_y$ in the BZ with respect to the total intensity (adding PES and inverse PES) which for the Hubbard model satisfies the sum rule $\int_{-\infty}^{+\infty} d\omega A(\mathbf{p}, \omega) = 1$ at all dopings. It will be shown that the momentum dependence is crucial in our analysis.

Before describing the computational results, let us define when a theoretically calculated PES signal can be predicted to be “observable” in an experiment. PES

spectra have large backgrounds, whose origin and shape are a matter of discussion, superimposed on the actual relevant signal. This background depends on the momentum, and also changes from sample to sample with fluctuations as large as 50%. Since the background is convex, the natural requirement for a PES theoretically calculated signal to be observable is that the combination background-signal produces a local maximum (i.e. a peak in the measured intensity).[40] From the data obtained on the insulating compound $\text{Sr}_2\text{CuO}_2\text{Cl}_2$, and the intensity of the signal at the last point where the dispersion is observed i.e. $\mathbf{p} = (0.7\pi, 0.7\pi)$, it is concluded that a peak with an intensity of roughly 10% of the largest signal (located at $\mathbf{p} = (0.5\pi, 0.5\pi)$) would be at the verge of being detected.[40] This is the criterion followed here to label a result as “observable”.

The choice of coupling is important in our search for PES weight above \mathbf{p}_F . For example, we observed that working on an 8×8 cluster, at $U/t = 4$, half-filling and temperature $T = t/4$, the percentage of PES spectral weight at $\mathbf{p} = (3\pi/4, 3\pi/4)$, i.e. the next available momentum after $(\pi/2, \pi/2)$ on this cluster, is very small (less than 5% of the total), even though the spin correlations show clear indications of long-range order. Then, the actual value of the local moments is as important as the AF correlation length for the effect we are investigating. Since evidence has recently been given that another feature induced by antiferromagnetism,[41] namely the “hole” pockets, may be washed out by temperature effects in QMC simulations at $U/t = 4$, we consider this coupling to be too small for our purposes. Thus, here the analysis was restricted to $U/t = 8$.

In Fig. 3.2, $A(\mathbf{p}, \omega)$ at $T = t/2$ is shown.[42] It is difficult to reduce T due to sign problems, but nevertheless this temperature allows us to study the PES signal

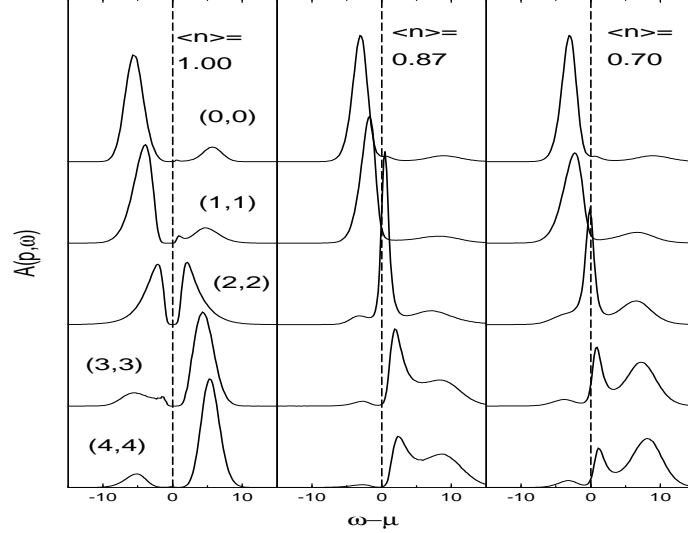


Figure 3.2: $A(\mathbf{p}, \omega)$, evaluated using QMC and ME techniques, for the 2D Hubbard model at $U/t = 8$, $T = t/2$ on an 8×8 cluster, at several densities $\langle n \rangle$. The momentum label varies along the diagonal in the BZ in units of $\pi/4$, and the percentages correspond to the integrated PES part of the spectral weight with respect to the total intensity ($=1$). The energy is in units of t .

above \mathbf{p}_F at different correlation lengths as the density is changed, which is the main purpose of this study. At half-filling, $\langle n \rangle = 1$, μ is located in the gap. The percentage of total PES spectral weight is shown for each momentum. A nonzero PES signal above the non-interacting Fermi momentum is clearly visible, and at $\mathbf{p} = (3\pi/4, 3\pi/4)$ it carries $\sim 23\%$ of the total weight. This result is very similar if the temperature is reduced to $T = t/4$. Note that for a pure spin-1/2 antiferromagnet the weight at $\mathbf{p} = (\pi/4, \pi/4)$ and $\mathbf{p} = (3\pi/4, 3\pi/4)$ should be identical at this density, but for a Hubbard model at finite U/t spin-density-wave mean-field approximations[65] show a reduction of the intensity of the PES signal above \mathbf{p}_F with respect to the Heisenberg limit.[44] Away from half-filling, at $\langle n \rangle = 0.87$, the amount of weight at $\mathbf{p} = (3\pi/4, 3\pi/4)$ is reduced to $\sim 10\%$, which is still visible in

the scale of the figure, although it is rather weak. The height of the peak, as a percentage of the peak height at $\mathbf{p} = (\pi/2, \pi/2)$ and half-filling, is about 15%.

At this point, it can be argued naively that the effect reported in Fig. 3.2 may only be evidence for the presence of the lower Hubbard band instead of antiferromagnetism. Actually, if the summation over momenta is carried out in Fig. 3.2 to construct the density of states at each doping level, it can be shown that aside from an expected redistribution of weight as the density changes, the two large bands in the spectrum are not much affected by doping. Thus, even at very low electronic densities where antiferromagnetism has clearly vanished, there is spectral weight below μ forming the lower Hubbard band. However, for $\langle n \rangle \sim 1$, i.e. with antiferromagnetism in the ground state, the weight below μ tends to be distributed evenly below and above \mathbf{p}_F , while for the case of $\langle n \rangle \sim 0.70$ when antiferromagnetism has virtually vanished the situation is drastically different with almost all of the PES weight located below \mathbf{p}_F . *Thus, the momentum dependence of $A(\mathbf{p}, \omega)$ is the key point to distinguish between an effect induced by AF correlations and an effect merely caused by the lower Hubbard band.*

To relate these results with experiments, and to provide further support for our interpretation, in Fig. 3.3(a) we show the numerically calculated spin correlations. At $\langle n \rangle = 1$, the correlation is robust (although it decays slowly to zero due to temperature effects), while at $\langle n \rangle = 0.70$ it is clearly very small. At an intermediate density $\langle n \rangle = 0.87$, ξ_{AF} is between one and two lattice spacings, resembling the experimental situation in YBCO, and presumably also in Bi2212, since both are at optimal doping.[45] Comparing Figs. 3.2 and 3.3 it is clear that the QMC PES signal *above* \mathbf{p}_F is *correlated* with the presence of antiferromagnetism in the spin correla-

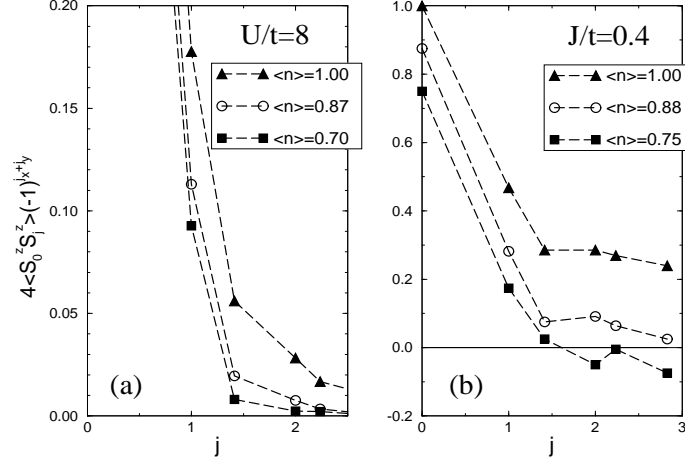


Figure 3.3: (a) Spin-spin correlation $4\langle S_i^z S_{i+j}^z \rangle (-1)^{|j|}$ vs distance, $j = |j|$, for the 2D Hubbard model calculated using QMC at $T = t/2$, $U/t = 8$, and several densities on an 8×8 cluster; (b) Spin-spin correlations as defined in Fig. 3.3(a), for the 2D t-J model calculated using exact diagonalization techniques on a 4×4 cluster with two holes, at several couplings.

tions. Again, the momentum dependence of the spectral weight is crucial for our interpretation of the data. For this particular calculation we conclude that a doping of 25% holes makes the weight induced by antiferromagnetism almost negligible, while at 12% doping the effect is still observable. Note that it is *not* necessary to have a large spin correlation length for the observation of weight above p_F . $\xi_{AF} \sim 2a$ seems to be enough.

3.3 $A(p, \omega)$ for the t-J Model

Thus far, our QMC analysis of the Hubbard model does not allow us to separate the actual sharp quasiparticle-like peak at the top of the valence band (which forms the band discussed in Ref.[56,35]) from the rest of the incoherent contribution at larger binding energies. To clarify this situation we need to study strongly correlated electrons with a technique that provides more accurate dynamical information than

ME. For this purpose, here we consider Exact Diagonalization (ED) techniques applied to the well-known 2D $t - J$ Hamiltonian[46] defined by

$$H_{tJ} = -t \sum_{\langle i,j \rangle \sigma} (\tilde{c}_{i\sigma}^\dagger \tilde{c}_{j\sigma} + \text{h.c.}) + J \sum_{\langle i,j \rangle} (\mathbf{S}_i \cdot \mathbf{S}_j - \frac{1}{4} n_i n_j), \quad (3.2)$$

in the standard notation.

The restriction of the Exact Diagonalization method to small clusters should not be a major problem in calculations where ξ_{AF} is very small. To increase the momentum resolution along the diagonal in the BZ, we combined the results for the 16 site cluster (providing momenta $(0,0), (\pi/2, \pi/2), (\pi, \pi)$) and the 18 site cluster (containing $(\pi/3, \pi/3), (2\pi/3, 2\pi/3)$).[47] The geometry of tilted square clusters, such as the $\sqrt{18} \times \sqrt{18}$ lattice, is discussed in the introduction of chapter 2.

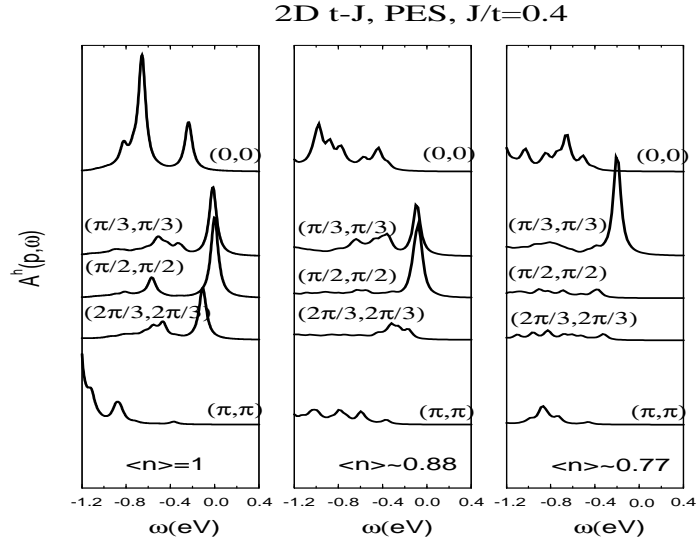


Figure 3.4: PES $A(\mathbf{p}, \omega)$ evaluated using exact diagonalization techniques for the 2D t - J model, at $J/t = 0.4$ on 4×4 and $\sqrt{18} \times \sqrt{18}$ clusters. The densities are shown in the figure. We assumed $t = 0.4\text{eV}$, and provided a width $\delta = 0.1t$ to the peaks. The momenta are indicated, and the relevant peaks are shaded.

In Fig. 3.4, the PES $A(\mathbf{p}, \omega)$ spectrum is shown for the t - J model. $J/t = 0.4$ was selected to model the cuprates,[46] but we checked that the results are similar in

the range between $J/t = 0.2$ and $J/t = 0.8$. As expected, at half-filling the largest peak near the chemical potential (quasiparticle) is obtained at $\mathbf{p} = (\pi/2, \pi/2)$. Increasing the diagonal momenta away from it, a considerable amount of spectral weight induced by ξ_{AF} exists as was observed in early studies of the t-J model.[48] Moving away from half-filling into the subspace of two holes (close to $\langle n \rangle \sim 0.88$) the dominant peak remains at $\mathbf{p} = (\pi/2, \pi/2)$ within our momentum resolution. At $(\pi/3, \pi/3)$ the quasiparticle strength is still large and coherent. At $\mathbf{p} = (2\pi/3, 2\pi/3)$ the peak seems now broader in the scale used, although its integrated spectral weight remains close to that of $\mathbf{p} = (\pi/3, \pi/3)$. The height of the peak at $\mathbf{p} = (2\pi/3, 2\pi/3)$ as a percentage of the largest peak located at $\mathbf{p} = (\pi/2, \pi/2)$ is 15-20% i.e. within the “observable” region defined before. Finally, at density $\langle n \rangle = 0.77$, the result resembles that of a weakly interacting system with a Fermi momentum close to $\mathbf{p} = (\pi/3, \pi/3)$, above which the signal is too weak to be observable in PES experiments. Then, we believe that weight above \mathbf{p}_F can be observed at $\langle n \rangle \sim 0.88$ but no longer at density $\langle n \rangle \sim 0.77$. To make contact with experiments it is again necessary to consider the corresponding spin correlations shown in Fig. 3.3(b). At half-filling, ξ_{AF} is clearly larger than the lattice size. At $\langle n \rangle \sim 0.88$, a crude exponential fit of the spin correlation vs. distance gives $\xi_{AF} \sim 1.5a$ (similar to that of YBCO and Bi2212 at optimal doping), while at $\langle n \rangle \sim 0.77$, ξ_{AF} is less than one lattice spacing. Then, we arrive to the conclusion that for a real material with $\xi_{AF} \sim 2a$ the antiferromagnetically generated PES weight, although weak, may still be observable above the background.

In Fig. 3.5, $A(\mathbf{p}, \omega)$ is shown at $\langle n \rangle \sim 0.88$ using an enlarged energy scale. The dispersion of the sharp peak (I) discussed before in Fig. 3.4, has a bandwidth

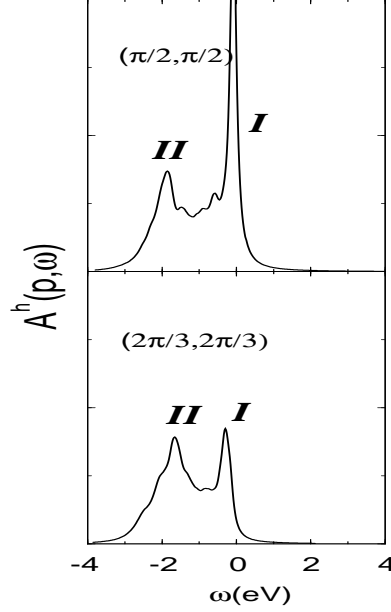


Figure 3.5: PES $A(\mathbf{p}, \omega)$ for the t-J model at $\langle n \rangle \sim 0.88$, $J/t = 0.4$, clusters of 16 and 18 sites, and expanding the energy scale to observe the two peak structure. We use $\delta = 0.25t$ and $t = 0.4\text{eV}$.

of order J , while at higher energies a considerable amount of spectral weight is found contributing to the bulk of the valence band (II). Peak (I) may be smoothly connected to the bands discussed by Kampf and Schrieffer in the weak coupling limit.[56]

3.4 Conclusions

Summarizing, in this section an analysis of the PES spectra in the 2D Hubbard and t-J models at several densities was reported. If these models reproduce the physics of the high- T_c compounds, then we conclude that antiferromagnetically induced photoemission weight should be observable even for materials with spin correlations lengths of only a couple of lattice spacings, as in Bi2212 at optimal doping. This is *compatible* with the experimental results of Fig. 3.1. However, we

found that this regime is at the verge of observability and thus our results, based on rough models and order-of-magnitude estimations, cannot uniquely establish the validity of Aebi et al.'s interpretation of their experimental data. We have only shown that the strength of their signal and ours are similar and thus there is compatibility between theory and experiments. We expect that the PES signal above p_F should no longer be visible above the large experimental background at dopings larger than optimal ($\sim 15\%$). To gather further evidence that the experimental signal is indeed caused by antiferromagnetism we believe that it is necessary to carry out PES experiments as a function of hole doping. We predict that the strength of the signal above p_F should increase as the system moves away from the optimal doping level towards half-filling. A possible candidate for such a study is YBCO with a critical temperature of about 60K. Another alternative within the Bi2212 family would be to consider $\text{Bi}_2\text{Sr}_2\text{Ca}_{1-x}\text{Lu}_x\text{Cu}_2\text{O}_{8+\delta}$ and $\text{Bi}_2\text{Sr}_{2-x}\text{La}_x\text{CaCu}_2\text{O}_{8+\delta}$ which are underdoped.[49]

CHAPTER 4

QUASIPARTICLE DISPERSION OF ONE-BAND ELECTRONIC MODELS

In this chapter, the spectral weight $A(\mathbf{p}, \omega)$ of the two dimensional $t - J$ and Hubbard models is calculated using exact diagonalization and quantum Monte Carlo techniques, at several electron densities $0.5 \leq \langle n \rangle \leq 1.0$. The photoemission ($\omega < 0$) region contains two dominant distinct features, namely a low-energy quasiparticle peak with bandwidth of order J , and a broad valence band peak at energies of order t . This behavior *persists* away from half-filling, as long as the antiferromagnetic (AF) correlations are robust. The results give support to theories of the copper oxide materials based on the behavior of holes in antiferromagnets, and also provide theoretical guidance for the interpretation of experimental photoemission data for the cuprates. The results presented in this chapter have been published by A. Moreo, S. Haas, and E. Dagotto in Phys. Rev. B **51**, 12045 (1995).

4.1 Introduction

Angle resolved photoemission (ARPES) techniques applied to the high temperature superconductors have produced interesting data that introduces important constraints on theories for the copper oxide planes. Recently, it has been shown[50] that the hole-doped compounds $\text{Bi}_2\text{Sr}_2\text{CaCu}_2\text{O}_8$, $\text{Bi}_2\text{Sr}_2\text{CuO}_8$, $\text{YBa}_2\text{Cu}_3\text{O}_7$, and

$\text{YBa}_2\text{Cu}_4\text{O}_8$ exhibit universal properties likely induced by the behavior of carriers in their common CuO_2 planes. In particular, it has been reported that the quasiparticle dispersion has a small bandwidth governed by an energy scale of the order of the exchange J of the Heisenberg model ($\sim 0.15\text{eV}$). In addition, in the vicinity of momenta $Y = (0, \pi)$ and $X = (\pi, 0)$, the dispersion is anomalously flat. These results give support to theoretical ideas based on strongly correlated electrons, since (i) it is well-established[51] that at half-filling the spectral function of a hole in an antiferromagnet contains a sharp quasiparticle peak at the top of the valence band spectra with a bandwidth of order J , and (ii) careful studies of the fine details of the hole dispersion in one band models have revealed the presence of flat regions near the X and Y points in momentum space.[52–55] The existence of these two features is a direct consequence of the presence of strong correlations and antiferromagnetism in the cuprates.

It is reasonable to assume that the behavior of holes in systems with long-range antiferromagnetic order will not change qualitatively as the density of holes is increased away from half-filling, as long as the antiferromagnetic correlation length ξ_{AF} remains large. Theories based on this assumption have been proposed.[56,57] In particular, in Refs.[52,57] it was shown that it is possible to reproduce many of the anomalous properties of the cuprates, including the presence of a d-wave superconducting state and the existence of an optimal doping, with the economical assumption that the sharp quasiparticle peak observed at half-filling at the top of the valence band remains robust as the electronic density decreases to phenomenologically realistic values. This assumption (i.e. approximate rigidity of the quasiparticle dispersion with doping) received support from recent calculations ad-

addressing the presence of “shadow bands” in the cuprates.[58] This work has been discussed in the previous chapter. The rigid band hypothesis has also been studied by other authors.[75] On the experimental side, recent ARPES results by Aebi et al.[60] have shown that features induced by the AF correlations at half-filling are also present at optimal doping. Since the closest structure to the Fermi level in $A(\mathbf{p}, \omega)$ is likely to dominate the low temperature properties of the model, then it is important to establish theoretically whether the quasiparticle peaks observed at half-filling survive in the presence of a finite density of holes.

4.2 Photoemission Spectra in the t-J and Hubbard Models at Half-Filling

In this chapter we discuss our analysis of the spectral weight for both the 2D $t - J$ and Hubbard models using exact diagonalization (ED) and quantum Monte Carlo (QMC) methods, supplemented by Maximum Entropy (ME)) techniques, and carried out at several densities. $A(\mathbf{p}, \omega)$ is shown to contain a two-peak structure, with dispersing features near the top of the valence band dominated by the scale of antiferromagnetism J , while a secondary broad structure appears at energies of order t . We discuss the range in parameter space where this behavior is to be expected, and its influence on the physics of carriers in the cuprates. However, note that recent QMC results have reported the presence of only *one* PES peak for the Hubbard model at both half-filling[61] and finite hole density.[54] We found that the disagreement with our present results is avoided once the influence of finite temperature effects is considered, and a more sophisticated ME method is used.

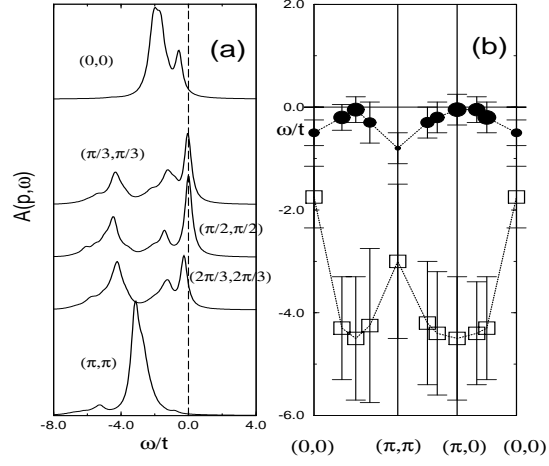


Figure 4.1: (a) Spectral weight $A(\mathbf{p}, \omega)$ of the 2D $t - J$ model at $J/t = 0.4$ using clusters of 16 and 18 sites along the diagonal in momentum space. The δ -functions have been given a width $\epsilon = 0.25t$ in the plots; (b) position of the two dominant peaks in $A(\mathbf{p}, \omega)$ as a function of momentum. The area of the circles is proportional to the intensity of the quasiparticle peak they represent. The error bars denote the width of the peak as observed in Fig. 4.1(a) (sometimes to a given broad peak several poles contribute appreciably). The full squares at $\omega \sim -4t$ represent the center of the broad valence band weight, and the area of the squares is *not* proportional to their intensity.

The technical details of the present computational study, as well as the Hamiltonians of the Hubbard and $t - J$ models, are the standard ones, unless otherwise stated. In Fig. 4.1(a), $A(\mathbf{p}, \omega)$ is shown for the $t - J$ model at *half-filling* and $J/t = 0.4$ using the ED technique applied to 2D clusters with 16 and 18 sites. The combination of these clusters allows enough resolution in momentum space to quantitatively analyze the dispersion of the main features in the spectral weight. The present results have been obtained using approximately 100 iterations in the standard continued fraction expansion (CFE) method to obtain dynamical properties using the Lanczos technique.[51] This technique has been discussed extensively in chapter 2.6 of this thesis. However, the figure shows that only a small number of poles are dominant. It is clear that near the Fermi energy, ($\omega = 0$), there is a robust

peak that weakly disperses in the scale of the figure. Remnants of this low-energy peak exist at momenta $(0, 0)$ and (π, π) , in the latter barely visible to the eye (but its intensity and position can be easily studied with the CFE approach mentioned above). In Fig. 4.1(b), the position of the low-energy peak is shown with full dots, with the convention that the area of the dot is proportional to the intensity of the peak. The bandwidth of this sharp quasiparticle-like peak is $\sim 0.8t = 2J$, in excellent agreement with our expectations based on previous ED[51] and Born approximation[53] calculations. The flat region near $(\pi, 0)$ is also visible in the figure. From Fig. 4.1(a) it is clear that additional PES spectral weight in $A(\mathbf{p}, \omega)$ is located at higher energies $|\omega|$. As discussed before in the literature, the strong correlation effects force the hole quasiparticle to carry only a fraction of the integrated weight,[62] and thus the presence of considerable incoherent intensity deep in energy is reasonable. A rough estimation of their position is shown in Fig. 4.1(b) (open squares).[63] This feature is not relevant for the low temperature behavior of the model which is dominated by the quasiparticle peak at the top of the valence band.

Before describing the density dependence of our results, let us clarify the importance of finite size effects in Fig. 4.1, as well as the differences between our results and those of previous QMC simulations.[54,61] To address both issues simultaneously, we have carried out an extensive QMC simulation of the 2D Hubbard model. The results reported here correspond to $U/t = 10$ (i.e. the strong coupling regime where the model should behave similarly to the $t - J$ model), temperature $T = t/4$, and using $\sim 10^5$ sweeps over the entire lattice to reduce the statistical errors. Here we use the “classic” ME technique.[64] This method gives a closer fit to the Monte Carlo data than the variant used in Ref.[54,61] and therefore resolves

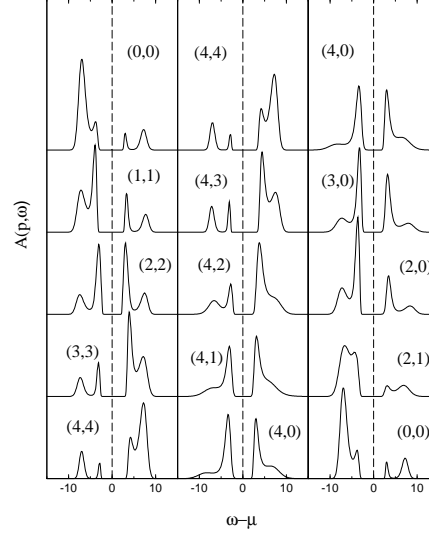


Figure 4.2: Spectral weight $A(\mathbf{p}, \omega)$ of the 2D Hubbard model obtained with the QMC method supplemented by Maximum-Entropy, on an 8×8 cluster, $U/t = 10$, and $T = t/4$.

more structure. The analytically-continued $A(\mathbf{p}, \omega)$ obtained at half-filling on an 8×8 cluster is shown in Fig. 4.2 at several momenta. The results are both qualitatively and quantitatively similar to those obtained for the $t - J$ model in Fig. 4.1, and also in good agreement with ED studies for the Hubbard model.[65] Two peaks in the PES region are clearly identified for all momenta. The peak structure resolved in this figure is a clear improvement with respect to Fig. 3.2 due to the lower temperature ($T=t/4$) used here. From their position it can be shown that the bandwidth of the peak at the top of the valence band is of order J , in excellent agreement with our previous discussion. The second broader feature observed in the ED study of the $t - J$ model is also present in the QMC simulation results. Studies at larger U/t couplings in the Hubbard model and in the region $0.2 \leq J/t \leq 0.8$ of the $t - J$ model show basically the same features. Then, here it is concluded that the qualitative physics of both models is very similar in the strong coupling region,

where a $A(\mathbf{p}, \omega < 0)$ with a double-peak structure is observed, as properly assumed in previous analytical studies.[56,52,66]

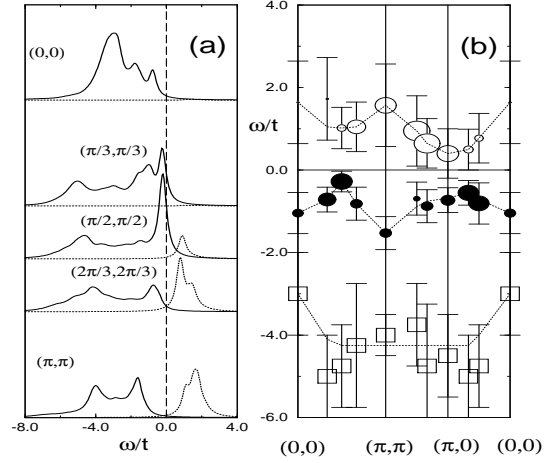


Figure 4.3: Same as Fig. 4.1 but for density $\langle n \rangle \approx 0.88$ (i.e. two holes on the 16 and 18 sites clusters). In (a) the PES intensity is shown with a solid line, while the IPES intensity is given by a dotted line. The chemical potential is located at $\omega = 0$. In (b) the full and open circles represent the PES and IPES intensities, respectively, of the peaks the closest to the Fermi energy. Their area is proportional to the intensity.

4.3 Photoemission Spectra in the t-J Model away from Half-Filling

Let us now discuss our results away from half-filling. In the relevant regime of density for the high-Tc superconductors, namely in the vicinity of “optimal doping” $\langle n \rangle \approx 0.85$, the QMC+ME method at large U/t produces stable results only at temperature $T = t/2$ which is too high to resolve the two peak structure even at half-filling. Thus, in this density regime only the ED results are reliable. In Fig. 4.3, ED data at density $\langle n \rangle \approx 0.88$ are shown (two holes in the 16 and 18 sites clusters). In this case ξ_{AF} is approximately two lattice spacings.[58] The PES results along the diagonal in momentum space present structure very similar to that discussed at

half-filling. The low energy peak is well-defined at all momenta, even those above the naive non-interacting Fermi momentum located near $(\pi/2, \pi/2)$, and still it disperses with a bandwidth of order J . The large accumulation of weight at higher energies $|\omega|$ remains localized at $\omega \sim 4t$. Then, to the extent that the one band models reproduce the physics of the high-Tc cuprates, it is reasonable to expect that PES experiments carried out at half-filling *and* near the optimal doping, should produce dispersive features of similar intensity and bandwidth. The clear similarity between the experimental bandwidth of the Bi2212 PES data, and recent results for the *insulating* $\text{Sr}_2\text{CuO}_2\text{Cl}_2$ compound,[67] provides more evidence for the validity of strongly correlated one band models for the cuprates. However, it is important to remark that while the concrete prediction of our calculations is that the bandwidth of the hole carriers is of order J , the particular details of the dispersion may *differ* from compound to compound. For example, it has been recently remarked that to reproduce the data for $\text{Sr}_2\text{CuO}_2\text{Cl}_2$, the addition of a small t' -term to the 2D $t - J$ model is necessary.[68] Thus, care must be taken when the fine details of different compounds at different dopings are compared.

Now consider the inverse photoemission (IPES) ($\omega > 0$) intensity in Fig. 4.3. The observed spectral weight in the vicinity of (π, π) somewhat resembles the distribution for a non-interacting Fermi system. In principle, this effect does not seem reproduced by a rigid band filling of the states at half-filling. However, recently Eder and Ohta[73] have shown that if proper *quasiparticle* operators[62] are used in the calculation of the spectral weight (i.e. operators dressed by spin fluctuations, instead of bare electronic operators), then the intensity of the IPES region is much reduced and the quality of the rigid band description of the $t - J$ model appears

more clearly. This is an important point not much emphasized in the literature, namely that the robustness of the rigid band picture in a given model *cannot* be tested by analyzing the removal of “bare” electrons (sudden approximation) as produced by a PES experiment, but instead “dressed” carriers must be used. Thus, PES and transport experiments may differ in their predictions if holes are heavily renormalized as in the cuprates.

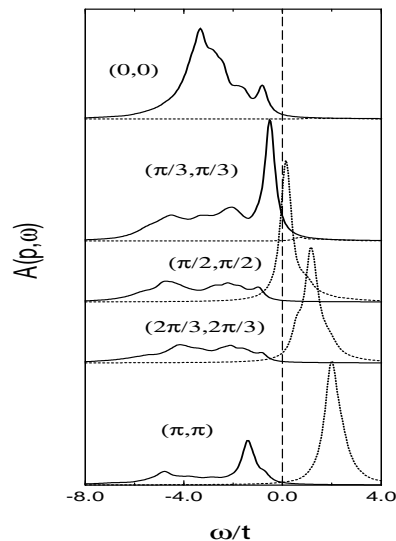


Figure 4.4: Same as Fig. 4.3(a) but for density $\langle n \rangle \approx 0.75$ i.e. 4 holes on the 16 and 18 sites clusters.

Figs. 4.4 and 4.5 show ED results for $A(\mathbf{p}, \omega)$ using the same clusters and coupling as at half-filling, but now reducing further the density to $\langle n \rangle \approx 0.75$ and 0.50 (i.e. 4 and 8 holes in the 16 and 18 sites clusters). In this case, through the spin correlations we observed that ξ_{AF} is less than one lattice spacing and thus the influence of AF fluctuations should be small at these densities. Indeed the two-peak structure discussed before at higher densities is now difficult to identify. While the broad valence-band feature at $\omega \sim 4t$ remains, only remnants of the AF-induced intensity above the naive Fermi momentum can be observed. The IPES signal

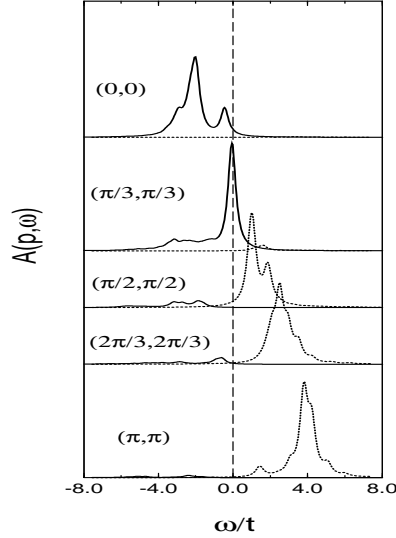


Figure 4.5: Same as Fig. 4.3(a) but for density $\langle n \rangle \approx 0.50$ i.e. 8 holes on the 16 and 18 sites clusters.

increased its intensity and now $A(\mathbf{p}, \omega)$ resembles the behavior of a non-interacting “ $\cos p_x + \cos p_y$ ” band.

An interesting detail of Figs. 4.1(a), 4.3(a) and 4.4, is that the intensity of PES weight at $\mathbf{p} = (\pi, \pi)$ changes appreciably as the density is varied. This is to be expected since $\mathbf{p} = (\pi, \pi)$ is the momentum the most sensitive to the presence of AF correlations. In particular, when $\xi_{AF} \rightarrow 0$, we expect that the PES weight at $\mathbf{p} = (\pi, \pi)$ will be mostly transferred to the IPES regime. The presence of PES weight at (π, π) and $\langle n \rangle = 1$ is a direct consequence of the AF correlations, and for a paramagnetic background $A((\pi, \pi), \omega < 0)$ should be negligible.

4.4 Conclusions

Summarizing, in this chapter the quasiparticle dispersion of the 2D $t - J$ and Hubbard models was analyzed as a function of the electronic density. At half-filling, $A(\mathbf{p}, \omega < 0)$ has a sharp quasiparticle-like peak at the top of the valence

band with a bandwidth of order J . This structure is the relevant one for the low temperature behavior of the models. A second broad feature deeper in energy was also identified. As the electronic density decreases, the “two peak” structure remains clearly visible as long as the antiferromagnetic correlation length ξ_{AF} is robust. When the AF fluctuations become negligible a crossover exists into a dispersion for the quasiparticles which resembles a weakly interacting system. For realistic values of the coupling, namely $U/t = 10$, this crossover from an antiferromagnetic metal to a paramagnetic ground state occurs between $\langle n \rangle = 0.88$ and 0.75 . Then, in the interesting regime for the copper oxide materials the AF correlations govern the behavior of the spectral weight. The present results give strong support to theories of the cuprates based on the behavior of carriers in an antiferromagnet,[56,57] and provides information about the crossover from a half-filled to a doped system that can guide the analysis of ARPES data.

CHAPTER 5

ON THE FERMI SURFACE OF STRONGLY CORRELATED ELECTRONIC MODELS

In this chapter, the evolution of the Fermi surface upon hole-doping is studied in the t-J model by exact diagonalization of chains and planes. In one dimension and at low hole doping, the momentum distribution function $n(k)$ indicates the presence of pockets at the (noninteracting) Fermi momentum, while increasing the density of holes a large Fermi surface is observed. Although the results in two dimensions are consistent with this picture, conclusive evidence for the existence of hole pockets cannot be provided in the present study of 4×4 and $\sqrt{18} \times \sqrt{18}$ square lattices. In order to improve the resolution in momentum space, twisted boundary conditions are used for the two-dimensional clusters. The results of this chapter have been published by S. Haas in Phys. Rev. B **51**, 11748 (1995).

5.1 Introduction

The shape of the Fermi surface in models of strongly correlated electrons has recently been a controversial issue.[72,73] It is known that long-range antiferromagnetic order in two spatial dimensions is only established at half-filling and $T = 0$. However, some theories for the formation of superconducting pairs at finite hole density have been guided by this limit, supplemented by the observation of robust

short-range antiferromagnetic correlations in the high- T_c compounds.[74–76] Some unusual normal state properties, like the linear temperature dependence of the resistivity and the change of sign in the Hall coefficient, can be accounted for in terms of strong antiferromagnetic correlations in these materials.[75,76]

The nature of quasiparticles in these systems is intimately related with the topology of the Fermi surface : do all electrons participate in the response to external fields, which would imply a large Fermi surface Γ Or is it possible to understand the low-energy properties in terms of a dilute gas of dressed holes occupying preferred points in momentum space on bands whose particular shape is produced by strong correlations Γ

At half-filling, models of strongly correlated electrons are known to be unstable towards the formation of a spin-density wave commensurate with the lattice. They are antiferromagnetic insulators because of strong on-site repulsion, and their Fermi surfaces have perfect nesting properties with nesting vector $\mathbf{Q} = (\pi, \pi)$ in 2D, or $Q = \pi$ in the one-dimensional analogue. How does the shape of the Fermi surface change upon hole doping Γ

There are two competing scenarios depicted in Fig.5.1. Approximations based on holon-spinon decoupling [77] and high-temperature expansions[78] suggest a large Fermi surface compatible with Luttinger's theorem and similar to the non-interacting case (Fig.5.1a). However, meanfield calculations based on spin-density fluctuations [74] and unbiased computational techniques[73,79–81] suggest the presence of hole pockets at low doping and low temperatures. The latter scenario does not necessarily contradict the apparent large Fermi surface observed by early photoemission experiments in the cuprates, [82] since thermal effects can easily

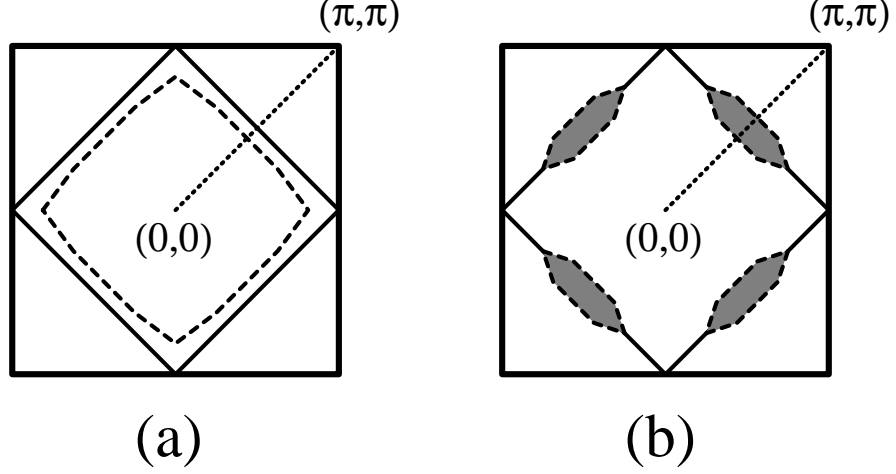


Figure 5.1: Schematic plot of the Fermi surface in strongly correlated electronic systems at low hole-doping ($\approx 10\%$). The solid line denotes the non-interacting case. (a) Scenario 1 : large Fermi surface; (b) Scenario 2 : hole pockets.

“wash out” and topologically connect the pockets producing a “large” surface (Fig.5.1(b)).[75,76,80,83] Recently, Aebi et al. used a novel photoemission technique that allows the mapping of the entire Fermi surface.[84] These authors show data which indicate the existence of hole pockets for Bi2212.

5.2 Momentum Distribution Function in 1D

In our study, we will discuss the momentum distribution function

$$n_{\sigma}(\mathbf{k}) = \frac{1}{N} \sum_{m,n} \langle \tilde{c}_{m\sigma}^{\dagger} \tilde{c}_{n\sigma} \rangle \exp(i\mathbf{k} \cdot (\mathbf{r}_m - \mathbf{r}_n)), \quad (5.1)$$

where $\tilde{c}_{n\sigma}$ creates a hole at site n . In clusters with an even number of holes, we have $n_{\uparrow}(\mathbf{k}) = n_{\downarrow}(\mathbf{k}) \equiv n(\mathbf{k})$. If there are indeed hole pockets constituting a pocket-like Fermi surface, a “dip” in $n(\mathbf{k})$ should be seen at momenta close to the Fermi surface of the half-filled system. Previous calculations[73–75,79,80] suggest that these minima are centered around $(\pi/2, \pi/2)$ and its rotational symmetry points as

indicated in Fig.5.1(b). In our study, we will explore $n_\sigma(\mathbf{k})$ along the diagonal in the Brillouin zone (indicated by the dotted line in Fig.5.1). This is a convenient choice, since the dip should be most dramatic along this line. Also, results for the one-dimensional analogue correspond to this cut of the Brillouin zone from the ferromagnetic ($\mathbf{k} = (0, 0)$) to the antiferromagnetic ($\mathbf{k} = (\pi, \pi)$) wave vector. Exact diagonalization of chains allows to access many more momenta along this line than in the two-dimensional analogue. The analysis of one-dimensional systems will be a guide to the intuition for the square lattice.

With our method, we will not be able to address the nature of the discontinuities which appear in $n_\sigma(\mathbf{k})$, especially not in the two-dimensional case where the resolution of the momentum distribution function is very coarse. The focus of this chapter is on the existence (or non-existence) of hole-rich areas in the vicinity of what would be the naive Fermi-surface obtained e.g. in a tight-binding calculation ($\mathbf{k} \simeq (\pi/2, \pi/2)$ in 2D close to half-filling).

Now, we will consider the t-J model which is assumed to capture the low-energy behavior of the cuprates. Its Hamiltonian is given by

$$H_{tJ} = -t \sum_{\langle i,j \rangle \sigma} (\tilde{c}_{i\sigma}^\dagger \tilde{c}_{j\sigma} + h.c.) + J \sum_{\langle i,j \rangle} (\mathbf{S}_i \cdot \mathbf{S}_j - \frac{1}{4} n_i n_j), \quad (5.2)$$

where the \tilde{c} -operators are hole operators acting on non-doubly occupied states, J is the exchange integral, and t is the hopping amplitude. In our study of the above system, we numerically diagonalize chains of up to 16 sites with closed shell boundary conditions, and 4×4 and $\sqrt{18} \times \sqrt{18}$ planes with mixed boundary conditions using a Lanczos algorithm (see chapter 2).

In one spatial dimension, the spin and charge degrees of freedom decouple. Hence the algebraic decay laws associated with spin, charge and superconducting correla-

tions are given in terms of two independent coefficients, k_ρ and k_σ . [85] When there is no spin gap, k_σ remains constant, and the low energy fluctuations depend only on k_ρ . [85] When $k_\rho < 1$, spin-density fluctuations ($\propto 1/r^{k_\sigma+k_\rho}$) dominate, while singlet superconducting fluctuations ($\propto 1/r^{k_\sigma+1/k_\rho}$) decay the slowest for $k_\rho > 1$. As $J/t \gg 1$, the holes tend to cluster together, and the system becomes phase separated. The phase diagram for the one dimensional t-J model is shown in Fig. 5.2. [86]

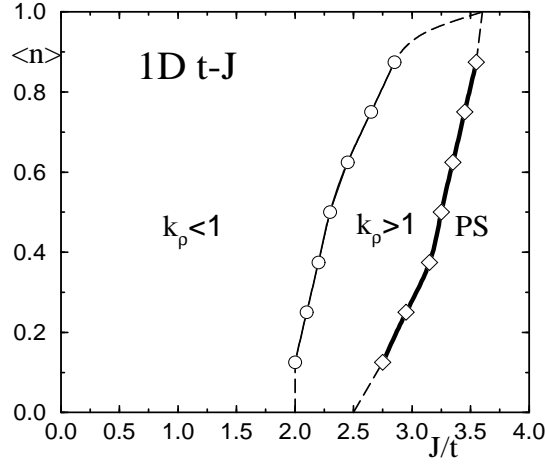


Figure 5.2: Phase diagram of the 1D t-J model as a function of the electronic density $\langle n \rangle$ and J/t from Ref. [86]. PS denotes “phase separation”, $k_\rho > 1$ ($k_\rho < 1$) implies that singlet superconducting (spin and charge) correlations decay the slowest in the ground state

Experiments in the cuprates suggest $J \approx 1450K$ and $J/t \approx 0.4$. However, compared to the 2D phase diagram (shown later in Fig. 5.5), the region around $J/t = 0.4$ in 1D is much further away from the strip of superconductivity ($k_\rho > 1$). Hence, it is reasonable to explore also the regime close to the onset of superconductivity in 1D in analogy to the 2D case.

In Fig. 5.3(a), the momentum distribution function on a linear 16-site cluster is shown at various fillings and $J/t = 0.4$. At half-filling, the momentum distribution

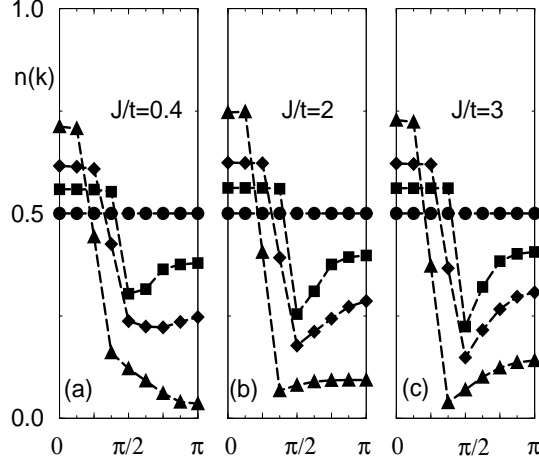


Figure 5.3: (a) Momentum distribution function $n(k)$ for a 16-site chain at $J/t = 0.4$. Circles correspond to the half-filled case ($\langle n \rangle = 1$), squares : 2 holes ($\langle n \rangle = 0.875$), diamonds : 4 holes ($\langle n \rangle = 0.75$), and triangles : 8 holes ($\langle n \rangle = 0.5$); (b) and (c) same as (a) but at $J/t = 2$ and 3, respectively.

function is constant ($n(k) = 0.5$), since the hopping term is not active. As the system is doped with holes, the Fermi momentum moves to lower values ($k_F < \pi/2$), and hole pockets can be seen around $k = \pi/2$ at fillings $\langle n \rangle = 14/16$ and $\langle n \rangle = 12/16$. Closer to the dilute limit, $\langle n \rangle \leq 8/16$, values for $n(k)$ similar to the non-interacting case are recovered. The depth of the pockets is maximum around $\langle n \rangle = 0.875$, which is in nice agreement with the results reported in Ref. [80].

Increasing the exchange coupling (Figs.5.3(b) and (c)), the pockets persist even beyond quarter-filling. However, the maximum pocket depth remains at $\langle n \rangle = 0.875$. The enhanced clustering of quasiparticles around $k = \pi/2$ can be understood in terms of an effective attraction among holes due to the exchange term as $J/t \gg 1$. [87] This mechanism ultimately leads to phase separation for $J/t > 3.5$, as shown in Fig.5.1(a).

Let us compare the results for the 1D t-J model with the one-band Hubbard model, which is known to have common low-energy properties in the limit $U/t \gg 1$. Its Hamiltonian is given by

$$H_{Hub} = -t \sum_{\langle ij \rangle, \sigma} (c_{i,\sigma}^\dagger c_{j,\sigma} + h.c.) + U \sum_i n_{i\uparrow} n_{i\downarrow}, \quad (5.3)$$

where $c_{i,\sigma}^\dagger$ creates an electron at site i with spin projection σ , $n_{i,\sigma}$ is the number operator, and the sum $\langle ij \rangle$ runs over pairs of nearest neighbor lattice sites. U is the on site coulombic repulsion, and t is the hopping amplitude.

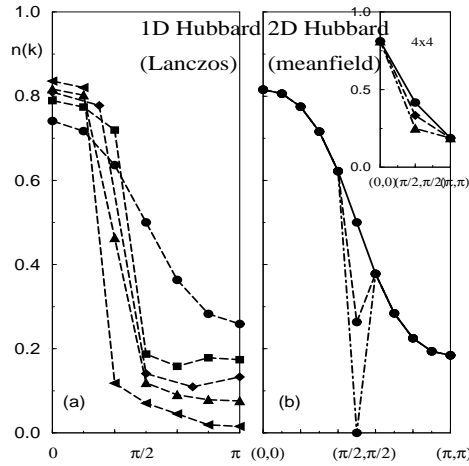


Figure 5.4: Momentum distribution function $n(k)$ for the Hubbard model at $U/t = 10$. (a) One-dimensional case obtained by exact diagonalization of $N=8$ and 12 clusters. Circles : $\langle n \rangle = 1$, squares : $\langle n \rangle = 0.833$, diamonds : $\langle n \rangle = 0.75$, upright triangle : $\langle n \rangle = 0.666$, and tilted triangle : $\langle n \rangle = 0.5$; (b) Two-dimensional case obtained by a meanfield calculation from Ref. [74,80]. The results for a 20×20 lattice are shown. The solid line corresponds to $\langle n \rangle = 1$, dashed line : $\langle n \rangle = 0.95$, and dot-dashed : $\langle n \rangle = 0.9$. The inset shows meanfield results for $n(k)$ in the 4×4 cluster for 1 hole (circles), 2 holes (diamonds), and 3 holes (triangles).

Since in the Hubbard model double occupancy is not forbidden at a given site, the size of the Hilbert space for a given cluster is much larger than for the t-J model. Thus we restrict ourselves to linear clusters of $N=8$ and 12 atoms. Closed

shell boundary conditions are used. In Fig.5.4 we show results for $n(\mathbf{k})$ at $U/t = 10$ (corresponding to $4t/U \simeq J/t = 0.4$). Our exact diagonalization results for the 1D case (Fig.5.4(a)) are in excellent agreement with the more elaborate Bethe-Ansatz calculations in the $U/t \rightarrow \infty$ limit by Ogata and Shiba.[86]

For the half-filled case, the Fermi momentum is exactly $k_F = \pi/2$. Similar to the t-J model, indications for the precursors of pocket formation around $k = \pi/2$ are seen at fillings $\langle n \rangle = 10/12$ and $\langle n \rangle = 6/8$. This is consistent with Monte Carlo results on 2D clusters which find pockets at electron densities > 0.75 , and a maximum effect at $\langle n \rangle = 0.9$. At fillings below $\langle n \rangle = 0.75$, in $n(\mathbf{k})$ we recover the topology of a dilute gas similar to the non-interacting case.

5.3 Momentum Distribution Function in 2D

In Fig.5.4(b), we show the result of a simple mean-field calculation in 2D following Ref. [74]. In this approximation, the antiferromagnetic state effectively produces a 2x2 unit cell. The mean-field Hamiltonian is diagonalized producing conduction and valence bands separated by an antiferromagnetic gap. The energy levels are given by $E_k = \pm \sqrt{\epsilon_k^2 + \Delta^2}$, where $\epsilon_k = -2t(\cos k_x + \cos k_y)$, and Δ is found using a self-consistent equation. At half-filling, the valence band is filled. Upon doping, quasiparticles are removed from the top of the valence band to mimic the presence of doping. Now, $n(\mathbf{k})$ is given by

$$n(\mathbf{k}) = \frac{1}{2} \left(1 - \frac{\epsilon_{\mathbf{k}}}{E_{\mathbf{k}}} \right), \quad (5.4)$$

where the chemical potential is chosen such that the density is $\langle n \rangle$.

Since this approach expands about a spin-density wave state which becomes stable at half-filling, we consider it to be valid only at high electronic fillings.[80]

In Fig.5.4(b), $n(\mathbf{k})$ along the $k = k_x = k_y$ direction calculated from this mean-field approximation is shown for a 20x20 lattice with $U/t = 10$ and $\langle n \rangle = 1.0, 0.95$ and 0.9 . There is a clear pocket-like feature at $(\frac{\pi}{2}, \frac{\pi}{2})$. The inset of Fig.5.4(b) shows $n(\mathbf{k})$ for the 4x4 cluster with one, two and three holes at $U/t = 10$. Although indents are observed at $(\frac{\pi}{2}, \frac{\pi}{2})$, the small size of the cluster prevents the formation of pockets. This is the same kind of finite size effect we will have to deal with when performing Lanczos calculations in 2D, and it probably also explains the absence of hole pockets reported in Ref. [72].

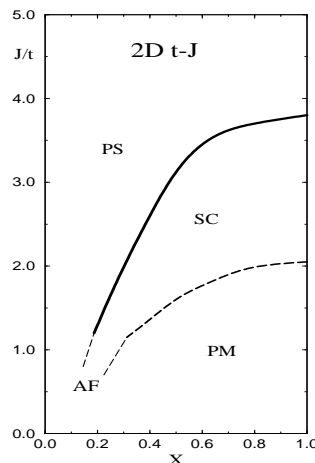


Figure 5.5: Schematic phase diagram of the 2D t-J model taken Ref.[76]. The notation is similar to Fig.5.2 with $x = 1 - \langle n \rangle$, “SC” denoting a mostly d-wave superconducting region (although close to $X=1.0$ it becomes s-wave), “PM” a paramagnetic region, and “AF” antiferromagnetism

Finally, let us turn to the t-J model in two dimensions. In previous studies, Dagotto et al. [76,88] have found a phase diagram that is similar to the 1D case in some respects (Fig.5.5). At large values for J/t , the effective attraction between holes, mediated by the exchange term, leads to phase separation of electron-rich and hole-rich regions. Close to the onset of phase separation enhanced superconducting

pairing correlations were reported. At $J/t \leq 1$, a paramagnetic phase with strong antiferromagnetic correlations is observed.

Evidence for hole pockets based on exact diagonalizations of small clusters remains controversial. 4×4 and $\sqrt{18} \times \sqrt{18}$ clusters provide a very low resolution in momentum space to study the topology of the Fermi surface.

In the present study of the 4×4 cluster, twisted boundary conditions are used to increase the resolution in momentum space.[89] A flux (ϕ_x, ϕ_y) is introduced into the hopping term which effectively shifts the ground state momentum by $\kappa = 2\pi[(\phi_x/L_x)\hat{x} + (\phi_y/L_y)\hat{y}]$, where $L_x = L_y = 4$ are the lengths of the sides of the lattice. Then, the hopping term in the Hamiltonian acquires a phase : $H_t = -t \sum_{i,\sigma} [\tilde{c}_{i,\sigma}^\dagger e^{i\phi_x} \tilde{c}_{i+x,\sigma} + \tilde{c}_{i,\sigma}^\dagger e^{i\phi_y} \tilde{c}_{i+y,\sigma} + \text{h.c.}]$. Along the diagonal ($k_x = k_y$) the total momenta are translated into $\mathbf{k} = \mathbf{k}_{old} + N_h \kappa$, where N_h is the number of holes and \mathbf{k}_{old} is the ground state momentum of the cluster with periodic boundary conditions. To obtain the momentum distribution function at $\mathbf{k}_1 = (\pi/4, \pi/4)$ and $\mathbf{k}_2 = (3\pi/4, 3\pi/4)$, we calculate $n(\mathbf{k}_1)$ and $n(\mathbf{k}_2)$ for twisted clusters, and average over the boundary conditions.

In Figs.5.6(a)-(c), we show the electronic momentum distribution for the 4×4 cluster along the line $(\Gamma - M - X - \Gamma)$ at various fillings and $J/t = 0.4$. While for the 2-hole case $n_\uparrow(\mathbf{k}) = n_\downarrow(\mathbf{k})$ is valid, for odd numbers of holes this is not true in general. Thus, we consider the quantity $n(\mathbf{k}) \equiv [n_\uparrow(\mathbf{k}) + n_\downarrow(\mathbf{k})]/2$. As can be seen in Fig.5.6(a), one hole in the 4×4 lattice has a momentum close to $(\pi/2, \pi/2)$. However, $n(\mathbf{k})$ for two and three holes (Figs.5.6(c) and (d)), does not show pocket formation, but only a small indent at $(\pi/2, \pi/2)$. For larger values of J/t , the size of the indents

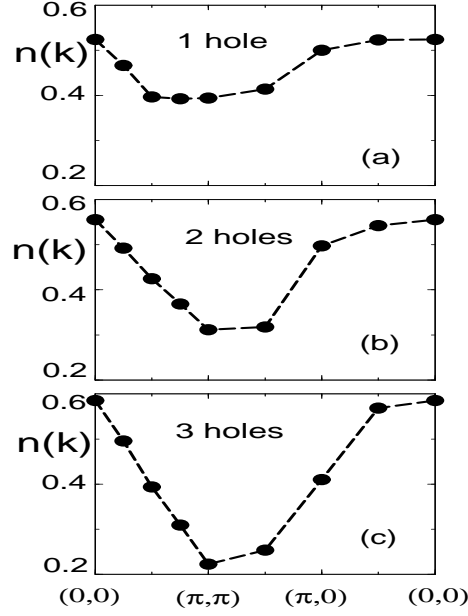


Figure 5.6: (a)-(c) Momentum distribution function for the t-J model in a 4x4 cluster at $J/t=0.4$ with one, two and three holes. The path through the first Brillouin zone is chosen along $\Gamma - M - X - \Gamma$. Twisted boundary conditions have been used to obtain $n(k)$ at $(\pi/4, \pi/4)$ and $(3\pi/4, 3\pi/4)$.

becomes more dramatic linking this effect to antiferromagnetic correlations in the system.

Although the observed $n(k)$ does not seem to support the hole pocket scenario at first glance, we would like to point out that this might be due to finite size effects in the cluster. The inset of Fig. 5.4(b) shows $n(k)$ for the 4x4 Hubbard system at $U/t = 10$ and the same fillings as in Figs.5.6(a)-(c). Although dips at $(\pi/2, \pi/2)$ are clearly observed in larger clusters, only indents comparable with our Lanczos results can be seen in the 4x4 lattice. Thus, the results shown in Figs.5.6(a)-(c) are at least compatible with the hole pocket picture.

Although our calculations are in good agreement with previous exact diagonalization studies of this system,[73,90,93,94] we would like to point out some of the

differences.[91] For the case of two holes on a 4x4 cluster, there is a degeneracy between $(0,0)$, $(\pi,0)$ and $(0,\pi)$. Guided by the reasonable assumption that two holes in an infinite lattice will produce a ground state with momentum $(0,0)$, previous authors have chosen this to be the ground state for their calculations in the 16-site square lattice.[90] However, since the $(0,0)$ state does not form a closed shell for this particular system, there is no apparent reason to prefer it over the $(\pi,0)$ and $(0,\pi)$ states. In particular, the present calculation is based on an average of the $(\pi,0)$ and $(0,\pi)$ states since in this case we find $n(\pi/2,\pi/2) < n(\pi,0) = n(0,\pi)$, consistent with the one-hole and three-hole behavior as well as with high temperature expansion calculations.[78,92] The opposite is found starting from the $(0,0)$ state.[90] Also, when a small negative next-nearest-neighbor hopping term is added to the Hamiltonian - a realistic assumption with regard to the hole-doped cuprates - the ground state momentum becomes $\mathbf{k} = (\pi,0) = (0,\pi)$.[79,95]

5.4 Conclusions

In summary, our results are compatible with the existence of hole pockets in models of strongly correlated electrons. In one dimension at low hole-doping, holes tend to cluster around certain momenta close to the Fermi surface, while at higher hole fillings the picture of a noninteracting gas of electrons becomes appropriate. We also find indications for a clustering of holes around $(\pi/2,\pi/2)$ in two dimensions. However, no conclusive evidence for the existence of hole pockets can be provided here. It has been argued that this might be due to finite size effects which also occur for spin-density wave mean-field calculations on small clusters. Our findings are in good agreement with recent numerical calculations[80] which support the picture of

hole pockets as has been brought forward in Ref. [74,75]. These findings are also consistent with recent photoemission experiments.[84] Our calculations can be made compatible with high temperature expansion results if the thermal wash-out effect is taken into account. [80,83] It is necessary to work at very low temperatures to observe hole pockets in these systems.

CHAPTER 6

INFLUENCE OF LONG-RANGE INTERACTIONS ON SUPERCONDUCTIVITY AND PHASE SEPARATION

In this chapter, the t-J model is studied including a long-range $1/r$ repulsive interaction. It is observed that *charge – density – wave* states become stable as the strength of the $1/r$ term, V_{coul} , is increased. Due to this effect, the domain of stability of the superconducting phase that appears near phase separation at $V_{\text{coul}} = 0$ is not enlarged by a $1/r$ interaction as naively expected. Nevertheless, superconductivity exists in a finite region of parameter space, even if phase separation is suppressed. Some of the results presented in this chapter have been published by S. Haas, E. Dagotto, A. Nazarenko, and J. Riera in Phys. Rev. B **51**, 5989 (1995).

6.1 Introduction

The presence of charge modulations and phase separation in the high- T_c compounds has recently attracted considerable attention.[96,97] In the present study of the t-J model, we observe that even in the presence of mobile carriers, CDW phases are stabilized by the $1/r$ term in a large region of parameter space, reducing the potential domain of stability of the superconducting phase. Nevertheless, we also notice that superconductivity is not strongly suppressed either (unless V_{coul} crosses some threshold).

The Hamiltonian for the $t - J$ model with $1/r$ interactions has the form

$$H = -t \sum_{\langle i,j \rangle \sigma} (\tilde{c}_{i\sigma}^\dagger \tilde{c}_{j\sigma} + \text{h.c.}) + J \sum_{\langle i,j \rangle} (\mathbf{S}_i \cdot \mathbf{S}_j - \frac{1}{4} n_i n_j) + V_{\text{coul}} \sum_{ij} \frac{n_i n_j}{r_{ij}}, \quad (6.1)$$

where the \tilde{c} -operators are hole operators acting on non-doubly occupied states, and r_{ij} is the shortest distance between sites i and j .

To analyze the ground state properties of this Hamiltonian Lanczos techniques are used (see chapter 2). Charge, spin and pairing correlations are monitored as a function of J/t , V_{coul}/t , and $\langle n \rangle$. In 1D, the conformal field theory parameter k_ρ is also studied.[97] If $k_\rho > 1$, the singlet pairing correlations decay the slowest against distance, and thus are dominant in the ground state. To discuss the results in both the 1D and 2D t - J model, for simplicity we will use the quarter filling density, $\langle n \rangle = 1/2$, where signals of superconductivity are clear even in small 2D clusters. The smooth connection between quarter-filling and half-filling at $V_{\text{coul}} = 0$, leads us to believe that the conclusions of this chapter are valid in the realistic regime of small hole density as well, where the relevant values of J/t are small in the 2D case.

6.2 The t - J - $1/r$ Model in 1D

It is helpful to first consider the atomic limit $V_{\text{coul}}, J \gg t$, where intuition can be gained about the states that will compete with superconductivity and phase separation. Several CDW phases were observed in the ground state as a function of J/V_{coul} after the $1/r$ interaction makes the phase separated regime unstable. These CDW phases have an increasing number of electrons in each microscopic cluster as J/V_{coul} grows, since J favors the formation of large spin structures to gain antiferromagnetic energy. Monitoring the density-density correlation functions, we observed that

the CDW states are stable even for a finite hopping t , and their rough domain of stability is shown in Fig. 6.1. Phase I is a standard Wigner crystal. Phase II is a Wigner crystal of pairs i.e. a regular distribution of charge $2e$ spin-singlets, similar to those observed in the t -J-V model.[98] This state is stable since the pairs take advantage of the short range effective attractive force produced by J . Phase III has clusters with four electrons, and as J increases the size of these microscopic clusters also increases smoothly producing a cascade of CDW phases. In the limit where J is the only relevant scale, phase separation is recovered.

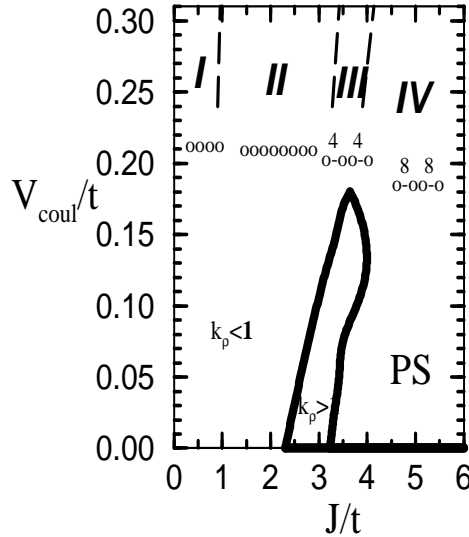


Figure 6.1: Phase diagram of the 1D t -J model with long-range $1/r$ interactions at density $\langle n \rangle = 1/2$ obtained from the analysis of a chain with 16 sites. The region $k_p > 1$ is where superconductivity dominates in the ground state. At large values of V_{coul} , or to the right of the superconducting region, the ground state is dominated by CDW order (states I, II, III, ... having different charge modulations). The open (full) circles denote holes (electrons). The size of each microscopic cluster in the CDW state increases as J/t increases, and the many CDW phases after IV are not shown. Phase separation (PS) is only stable at $V_{\text{coul}} = 0$ in the bulk limit.

When the hopping amplitude t is nonzero, intermediate values of J , and a small coupling V_{coul} , a regime of superconductivity exists (i.e. $k_p > 1$) on a finite region of parameter space, while in the bulk limit phase separation exists only along the

$V_{\text{coul}} = 0$ line in Fig. 6.1. In the pure t-J model, the compressibility diverges at the boundary of phase separation. On the other hand, at finite V_{coul} , k_ρ is a smooth function of J/t , it becomes larger than one on a small region, and then it smoothly converges to zero at large J/t . To gain more intuition about the physical behavior of the system, we also studied pairing correlations observing that in the regime where $k_\rho > 1$, these correlations are indeed very strong in the ground state and they continue having a large value, beyond the apparent stability regime signaled by k_ρ . This curious effect shows that short distance superconducting fluctuations may be relevant in a wide region of parameter space, even if their asymptotic power-law decay is not the dominant one.

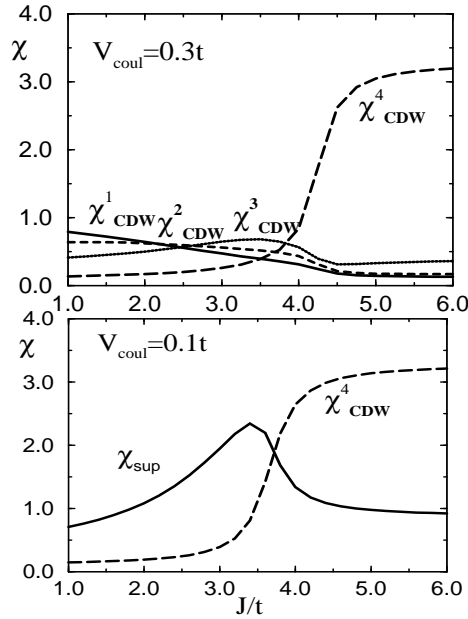


Figure 6.2: CDW and SC susceptibilities in the 1D t-J-1/r model. The superscripts for the CDW susceptibilities correspond to the various CDW modulations depicted in Fig. 6.1.

To illustrate the crossover between different modulations of charge-density-waves and superconductivity, in Fig. 6.2 we show the susceptibilities corresponding to

CDW and SC correlations as a function of the parameters J/t and V_{coul}/t . These susceptibilities are related to the real space correlation functions by

$$\begin{aligned}\chi_{sup} &= \frac{1}{N} \sum_{i,j} \langle \Delta_i \Delta_j \rangle, \\ \chi_{CDW} &= \frac{1}{N} \sum_{i,j} \langle n_i n_j \rangle e^{i\phi(r_i - r_j)},\end{aligned}\tag{6.2}$$

where ϕ controls the modulation of the charge-density-wave. As is seen in this figure, superconductivity dominates in a region $2.4 \leq J/t \leq 3.2$ at small values for the parameter V_{coul}/t which controls the Coulomb tail. At $V_{\text{coul}}/t = 0.3$ the superconducting susceptibility is very weak (not shown for this case), and various CDW phases dominate.

6.3 The t-J-1/r Model in 2D

In 2D we have carried out an analysis using 4×4 clusters, In the atomic limit, which can be explored on larger clusters, the set of stable CDW phases is qualitatively different from the 1D case. Here, striped phases (holes ordered in one dimensional chains along the x or y axis) are dominant in most of parameter space. As J increases, the number of contiguous chains of electrons in the striped phases smoothly increases. [99]

Away from the atomic limit, a numerical analysis of the pairing correlations similar to that carried out for the pure 2D t-J model suggests that superconductivity is robust in a region of parameter space analogous in shape to that observed in 1D. The analysis of the other phases is more complicated due to the weakness of the density-density correlations, and thus in this sense the actual boundaries be-

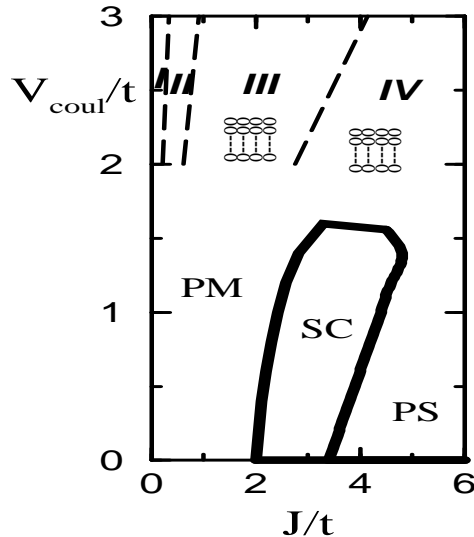


Figure 6.3: Phase diagram of the 2D t - J model at density $\langle n \rangle = 1/2$ obtained using a 16 sites square cluster. SC is (d-wave) superconductivity, PM a paramagnetic region, PS phase separation, I is the standard Wigner crystal, II a Wigner crystal of pairs, and III and IV are shown in the figure.

tween the various CDW phases in Fig. 6.3 should be considered only as qualitative. Nevertheless the trends are clear from the numerics, and similar to those in 1D.

6.4 Conclusions

Our study suggests that although phase separation is destabilized by the $1/r$ correlation, the region left empty is mostly replaced by CDW phases. The modulation of the various CDW phases depends strongly on the interaction strength, J/t , between the electrons. Nevertheless the superconducting phase survives in the presence of the Coulomb interaction as long as its strength is not too large. In a more complete study, we have shown that this scenario holds for other models of correlated electrons, i.e. for the Hubbard model with long-range Coulomb interactions.[100] Also, a similar competition between various CDW phases has been observed in a related spin-1 Ising system. [99]

CHAPTER 7

DYNAMICAL PROPERTIES OF ANTIFERROMAGNETIC HEISENBERG SPIN CHAINS

In this chapter, the dynamical properties of spin-1 and spin-1/2 Antiferromagnetic Heisenberg Chains (AHC's) are studied by exactly diagonalizing clusters of up to 18 and 26 sites, respectively. It is shown that the spin-1 AHC has a quasi-single-mode spectrum for momenta $k \geq 0.3\pi$, while the low energy edge of the spin-1/2 AHC is dominated by a spin-wave continuum. The dispersion curve obtained for the spin-1 chain is in excellent agreement with recent experiments on NENP. The size dependence of the low energy spectral weight is also analyzed. The results of this chapter have been published by S. Haas, J. Riera, and E. Dagotto in Phys. Rev. B 48, 3281 (1993).

7.1 Introduction

The Quantum Heisenberg Antiferromagnet is one of the simplest nontrivial models of strongly correlated electrons. However, its ground state properties are not entirely understood. In particular, the one-dimensional Antiferromagnetic Heisenberg Chain (AHC) has recently been given much attention both theoretically [101–109] and experimentally [110–113]. This interest is mainly due to Haldane's [106] prediction of a finite gap in the excitation spectrum of integer-spin AHC's leading to

finite magnetic correlations, to be compared with the spectrum of half-odd-integer spin chains which is presumed to be gapless. Previous numerical studies for the isotropic spin-1 AHC have indeed confirmed the presence of a spin gap $\Delta_\pi \simeq 0.41J$ at $k = \pi$ and $\Delta_0 \simeq 2\Delta_\pi$ at $k = 0$, where J is the Heisenberg exchange integral. [107] However, not much theoretical information on *dynamical* properties of spin-1 chains is available. Carrying out such a calculation became particularly important after the recent experiments by Ma et al.[110] on the spin-1 AHC $Ni(C_2H_8N_2)_2NO_2ClO_4$ (NENP) which have provided strong evidence of a long-lived single-mode picture in the interval $0.3\pi \leq k \leq \pi$ (the region $k \leq 0.3\pi$ is experimentally difficult to access due to the small magnetic scattering cross section in this regime). In contrast to the half-odd-integer spin chains, the dispersion curve was found to be asymmetrically displaced about $k = \pi/2$ and presents gaps for all momentum transfers. [110] The integrated energy intensity drastically decreases for momentum $k < \pi/2$. Can these results be reproduced by a simple spin-1 Heisenberg model on a chain?

In this chapter, the dynamical behavior of AHC's with and without spin-gaps is analyzed and compared with experiments. We will study the excitation spectrum contained in the zero-temperature dynamical structure factor $S(k, \omega)$ which is proportional to the scattering cross section measured in Inelastic Neutron Scattering experiments[110–112] at low temperatures ($k_B T \ll \hbar\omega_k$). In excellent agreement with experiments, we observed that interactions between the dominant excitations are negligible in this regime, leading to a single-mode spectrum in the integer-spin case above a certain threshold momentum transfer.[110] For a quantitative comparison of the present numerical results with Ma's data it is necessary to take into account the single-ion anisotropy of NENP which is about $D \approx 0.18J \approx 0.8$ meV.[110]

While relatively little is known about the dynamical properties of spin-1 chains, a vast literature on the spin-1/2 AHC is available. Static ground state properties have been calculated using the Bethe Ansatz.[114,115] However, an exact evaluation of $S(k, \omega)$ in Bethe's framework has not been accomplished. Müller et al.[101] proposed an approximate expression for the dynamical structure factor which agrees well with Inelastic Neutron Scattering studies on $KCuF_3$ and $CuCl_2 \cdot 2N(C_5D_5)$. [112,113] Recent experimental work by Nagler et al. [112] has nicely confirmed the existence of a spin-wave continuum with a gapless onset at the antiferromagnetic zone center ($k = \pi$) and at $k = 0$.

7.2 Spin Dynamics on the Heisenberg Chain

The Hamiltonian of the one-dimensional Quantum Heisenberg Antiferromagnet in the presence of single-ion anisotropy is defined by

$$H = J \sum_i \mathbf{S}_i \cdot \mathbf{S}_{i+1} + D \sum_i (S_i^z)^2, \quad (7.1)$$

where the sum is taken over all cluster sites, and the rest of the notation is standard. The in-plane anisotropy $E \sum_i [(S_i^x)^2 - (S_i^y)^2]$ has been neglected here. In the case of NENP it has been experimentally observed that $J \approx 3.8-4.1$ meV and $D \approx 0.18J$, [110] while for $KCuF_3$ the parameters are $J \approx 17.5$ meV and $D \approx 0$. [112] D is produced by the coupling of a spin to the orbital motion. It destroys the spin rotational symmetry of the pure Heisenberg Antiferromagnet and pulls the spins into the xy plane.

Let us shortly discuss the microscopic origin of the single-ion anisotropy. The total wavefunction for a real material contains spatial, orbital and spin contributions. The spatial and the orbital part are usually neglected for spin systems. However,

here we want to consider the effect of spin-orbit coupling $\lambda \mathbf{L} \cdot \mathbf{S}$, and thus the wavefunction has to be written as a product : $|\phi\rangle = |l, l_z\rangle \otimes |s, s_z\rangle$. For the case of Ni^{2+} ions, the orbital contribution to the wavefunction is a constant corresponding to two half-filled 3d orbitals (see the discussion of NENP in the introduction). Since spin-orbit coupling destroys the rotational symmetry of the Heisenberg Hamiltonian, we have now a preferred quantization axis which we choose to be along the z-direction. Then, the spin-orbit term at a given site 'i' is given by $\lambda L_i^z S_i^z$. Let us now treat this term to lowest order in perturbation theory. Since the spin and the orbital contribution can be separated we obtain a shift in energy of $D \sum_f |\langle f, s, s_z | S_i^z | 0, s, s_z \rangle|^2$, where 'f' denotes final states, '0' is the ground state, and the orbital contribution is absorbed in the constant $D = \lambda^2 \sum_f \frac{|\langle f, l, l_z | L_i^z | 0, l, l_z \rangle|^2}{E_f - E_0}$.

We diagonalize Eq.(7.1) on finite clusters with periodic boundary conditions using the Lanczos algorithm.[116] At $T=0$ the dynamical structure factor is given by

$$S^{\alpha\alpha}(k, \omega) = \sum_n |\langle n | S_k^\alpha | 0 \rangle|^2 \delta(\omega - (E_n - E_0)), \quad (7.2)$$

where $\alpha=x,y,z$, $S_k^\alpha = \frac{1}{\sqrt{N}} \sum_l e^{ikl} S_l^\alpha$, N is the number of sites, $|n\rangle$ denotes an eigenstate of H with energy E_n (E_0 being the ground state energy), and the rest of the notation is standard. $S^{\alpha\alpha}(k, \omega)$ is extracted from its corresponding Green's function

$$S^{\alpha\alpha}(k, \omega) = -\frac{1}{\pi} \text{Im} G^{\alpha\alpha}(k, \omega) \quad (7.3)$$

which can be written in the form of a continued fraction[116,117]

$$G^{\alpha\alpha}(k, \omega) = \frac{\langle 0 | (S_k^\alpha)^\dagger S_k^\alpha | 0 \rangle}{\omega - a_0 - \frac{b_1^2}{\omega - a_1 - \frac{b_2^2}{\omega - \dots}}}. \quad (7.4)$$

The coefficients a_n and b_n are obtained from the recursive relation

$$|f_{n+1}\rangle = H|f_n\rangle - a_n|f_n\rangle - b_n^2|f_{n-1}\rangle, |f_0\rangle = S_k^\alpha|0\rangle, \quad (7.5)$$

where Eq.(7.5) defines a set of orthogonal states. The coefficients are thus given by

$$\begin{aligned} a_n &= \langle f_n | H | f_n \rangle / \langle f_n | f_n \rangle, \\ b_{n+1}^2 &= \langle f_{n+1} | f_{n+1} \rangle / \langle f_n | f_n \rangle, b_0 = 0. \end{aligned} \quad (7.6)$$

As a check of our calculations we used the real space correlation functions to verify that the sum rule $\int d\omega S^{\alpha\alpha}(k, \omega) = S^{\alpha\alpha}(k)$ is satisfied. Here $S^{\alpha\alpha}(k) = \sum_j \exp(-ikj) \langle 0 | S_j^\alpha S_{j+1}^\alpha | 0 \rangle$ is the static structure factor.

The convergence of lattice diagonalizations with the number of sites for the gapless excitation spectrum of the spin-1/2 AHC is slower than for the spin-1 case. Thus, finite size effects have to be taken into account when information is extracted for the $N \rightarrow \infty$ limit. In order to reduce the size of our Hamiltonian matrix we use spin inversion, spin reflection and the translational symmetry of Eq.(7.1). In spite of these simplifications the characteristic Hilbert space of the 18-site spin-1 AHC has 1227112 basis elements. The construction and diagonalization of the Hamiltonian for the N=18 sites spin-1 chain at a given momentum 'k' demands less than an hour of CPU-time on a CRAY-2 supercomputer. To obtain the dynamical structure factor, a second run of roughly equal CPU-time is necessary.

7.2.1 Spin-1 AHC

Now let us analyze the results for the spin-1 chain. Previous studies have shown[104,107,109] that the ground state of the spin-1 AHC has zero-momentum and that its spin excitation spectrum is asymmetric about $k = \pi/2$. A finite (and

positive) uniaxial anisotropy splits the otherwise threefold degenerate lowest excitation into a higher-energy $S^z = 0$ state, that we will denote as the singlet, and a lower-lying $|S^z| = 1$ doublet. In our study we will concentrate on the dynamical structure factor along the z-axis which measures weights and positions of excitations in the $S^z = 0$ subspace. The splitting of the spectrum in the vicinity of $k = \pi$ due to in-plane anisotropy[110] has been neglected.

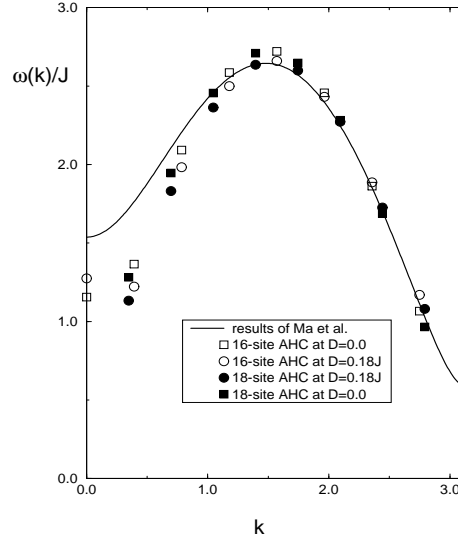


Figure 7.1: Dispersion curve for a spin-1 AHC. The solid line is a fit to experimental data for NENP. The symbols denote results from exact diagonalizations of 16-site and 18-site chains for anisotropies $D=0.0$ and $D=0.18J$, respectively. For momenta $k \leq 0.3\pi$, there is no observable spectral weight in the experimental data. The solid line in that region represents an extrapolation by the experimentalists.

In Fig. 7.1, we show the position of the lowest excitation energy observed in $S^{zz}(k, \omega)$ as a function of k , and compare it with the experimental results of Ma et al.[110] The solid line is a fit of their data to the dispersion relation

$$\omega_{||} = \sqrt{\Delta_{||}^2 + v^2 \sin^2 k + A_{||} \cos^2 \frac{k}{2}} \quad (7.7)$$

where $\Delta_{||} = 2.40 \pm 0.05$ meV, $v = 9.7 \pm 0.1$ meV and $A_{||} = 34 \pm 2$ meV. Our results were obtained from the exact diagonalization of $N=16$ and $N=18$ chains.

An excellent agreement is obtained in the region $k \geq 0.3\pi$, while there is no data available below $k = 0.3\pi$. The gap at $k = 0$ is about twice the gap at $k = \pi$, which has led to the assumption that at small k we are dealing with a continuum of excitation pairs with momentum π and $-\pi$. [110] In the slightly anisotropic case ($D=0.18J$) the $k = \pi$ singlet gap is given by $0.66J$ in agreement with the results of Golinelli et al. [109] To show the influence of the single-ion anisotropy D in the dispersion, we have also plotted our results for the $D=0$ case which may correspond to $A_gVP_2S_6$ where experimentally it was observed that $D/J \sim 10^{-4}$. [118]

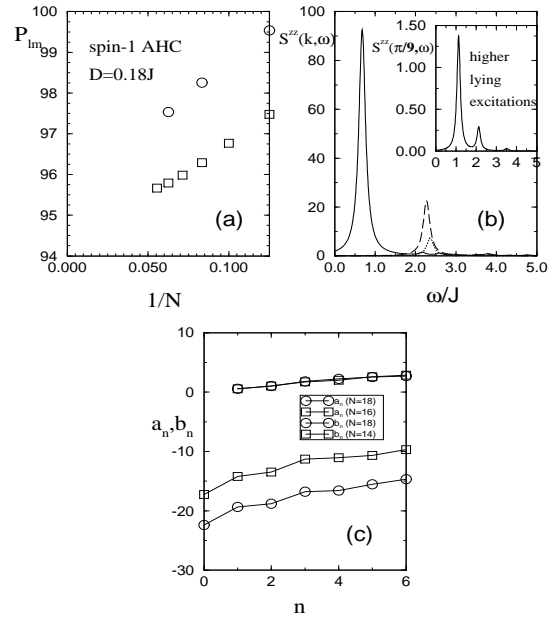


Figure 7.2: (a) Volume dependence of the spectral weight of the lowest lying excitation P_{lm} (in %) in spin-1 AHC's with up to 18 sites. Squares : $k = \pi$, octagons : $k = \pi/2$. N is the number of sites. In the limit $N \rightarrow \infty$ the spectral weights converge to finite values. (b) Out-of-plane dynamical structure factor of the $N=18$ spin-1 AHC with single-ion anisotropy $D=0.18J$ for different values of the momentum transfer. Solid line : $k = \pi$, dashed line : $k = 2\pi/3$, dotted line : $k = \pi/3$, inset : $k = \pi/9$. The delta functions have been given a finite width $\epsilon = 0.1J$. The inset shows that for low momentum transfers ($k \leq 0.3\pi$) higher lying modes are not negligible. (c) Lowest order coefficients in the continued fraction expansion for $S^{zz}(k, \pi)$. Octagons denote $N=18$, while squares correspond to $N=14$ spin-1 AHC.

The relative spectral weight of the lowest energy excitation in $S^{zz}(k, \omega)$ as a function of the lattice size N is shown in Fig. 7.2(a). As $N \rightarrow \infty$, the weights of the lowest excitation peaks converge to finite values (approximately 94% for $k = \pi$). The convergence is very rapid in the vicinity of $k = \pi$, which suggests a single-mode picture in this region. On the other hand, for low momentum transfers ($k \leq 0.3\pi$) higher lying modes appear in the spectrum, signaling the presence of multi-magnon interactions. However, the energy gap and *relative* peak intensity of the lowest excitation seem to remain finite in the bulk limit, even for small momentum transfer.

In Fig. 7.2(b), the dynamical out-of-plane structure factor of the $N=18$ chain is shown for different momenta at $D=0.18J$. The delta functions have been approximated by Lorentzians with a finite width $\epsilon=0.1J$. The integrated spectral intensity decreases rapidly as $k \rightarrow 0$, in agreement with experiments. As shown in the figure, for $k \leq 0.3\pi$ higher lying modes become visible, indicating the onset of a multi-magnon continuum. Also, we have observed that the total spectral weight of $S^{zz}(\pi, \omega)$ also decreases as a finite single-ion anisotropy D is switched on. This indicates that the spins prefer to lie in the xy plane for positive D . Correspondingly we would expect an increase in the spectral weights of $S^{xx}(\pi, \omega)$ and $S^{yy}(\pi, \omega)$ as D increases.

In Fig. 7.2(c), we show the first few coefficients of the continued fraction expansion for $S^{zz}(\pi, \omega)$ in the $N=14$ and $N=18$ chains. We observed that a truncation of the expansion beyond the first ~ 14 coefficients is possible without any noticeable change in the dynamical spectrum. It can be seen from Eq.(7.6) that the a_n 's carry units of energy while the b_n 's are dimensionless. The a_n 's are thus expected to grow proportional to the system volume N , while the b_n 's should converge to a finite value

as the bulk limit is approached. Both features, the scaling of a_n 's with the lattice size and the convergence of the b_n 's, are observed in Fig. 7.2(c). This provides evidence that the bulk limit has been already reached at $N=18$.

We have observed that the dominant low-energy pole is isolated, and the gap to higher lying excitations appears to persist in the bulk limit (a careful finite size study is necessary to verify the presence of a second gap in the spectrum). Isolated poles in the spectral functions of *holes* in two-dimensional antiferromagnets are common.[119] In that case, the creation of a hole causes a distortion of the background spin ground state. When the system relaxes to the new ground state, the hole of course still exists, but the mean values of the spins in its neighborhood have changed, and it has thus become a *dressed* hole quasiparticle. It may occur that a similar picture holds for the spin-1 chain, namely we flip a spin at a given site creating a local triplet state, and this state may relax at large times to a (still local) state not much different from the previous one, i.e. only its spin neighbors are altered. We are currently investigating this possibility.

7.2.2 Spin-1/2 AHC

The spin-1/2 chain has been studied extensively,[101–103,107,112–115] and there are approximate analytical expressions available for some dynamical observables. The onset of the excitation spectrum of a spin-1/2 AHC is given by the des Cloiseaux-Pearson dispersion[115]

$$\omega_k^{low} = \frac{\pi J}{2} |\sin(k)|, \quad (7.8)$$

which is gapless at $k = \pi$ and 0. Comparing our data in Fig. 7.3 for the lowest excitations of a $N=26$ chain with Eq.(7.8) we find good agreement. The small gap

at $k = \pi$ is due to the finite size of our chain and vanishes in the bulk limit.[117] In contrast to the massive spin-1 AHC, the spectrum is now symmetrical about $k = \pi/2$.

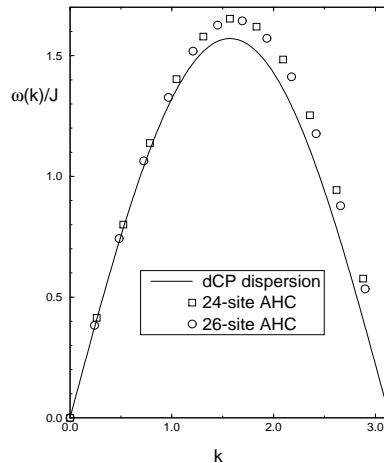


Figure 7.3: Dispersion curve of a spin-1/2 AHC. The solid line is the dispersion relation proposed by des Cloiseaux and Pearson. The symbols denote results from exact diagonalizations of 24-site and 26-site chains, respectively.

Above this lower boundary Eq.(7.8), there is a continuum of excitations which is believed to be made out of pairs of spinons[102] with momenta between 0 and $k/2$. The upper boundary of this continuum is given by

$$\omega_k^{upper} = \pi J |\sin(k/2)|. \quad (7.9)$$

In one dimension, a pair of spinons is created by flipping a pair of adjacent spins in the antiferromagnetic background (see Fig. 7.4). This process creates two frustrated links (highlighted by dashed lines in the figure) which propagate through the lattice. In Fig. 7.4, a schematic plot of a pair of spinons propagating on top of an antiferromagnetic background is given. However, note that for a spin-1/2 Heisenberg chain the background does not have long-range order (it has a gapless spectrum) because of strong quantum fluctuations.

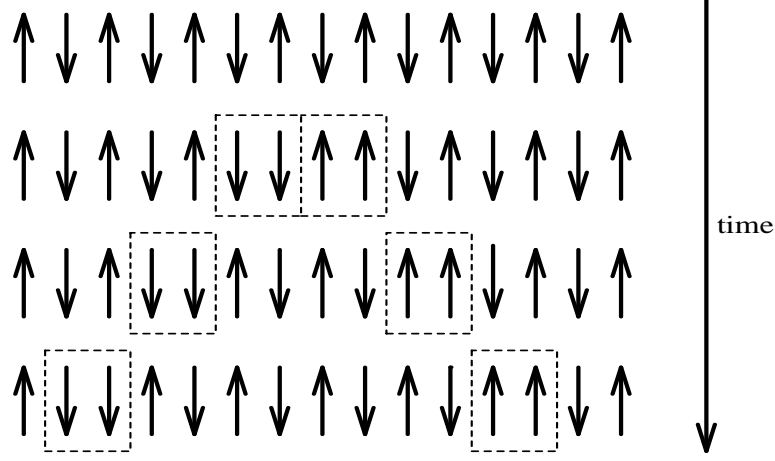


Figure 7.4: Schematic plot of a spinon pair propagating on top of an antiferromagnetic background.

Based on the selection rules and their exact dispersion curves, Müller et al.[101] have proposed the following approximate expression for the out-of-plane dynamical structure factor

$$S^{zz}(k, \omega) = \frac{A}{\sqrt{\omega^2 - \omega_k^{low2}}} \Theta(\omega - \omega_k^{low}) \Theta(\omega_k^{upper} - \omega), \quad (7.10)$$

where A is a constant and $\Theta(x)$ is a cut-off step-function. The upper cut-off at ω_k^{upper} was introduced to guarantee that the usual sum rules are satisfied. It may be interpreted as the maximum energy of a spinon pair. However, higher order scattering processes result in small contributions above this boundary which are observed in exact diagonalizations of finite clusters. Thus, Eq.(7.9) should not be interpreted as a rigorous sharp upper bound for the spectrum.

To compare these predictions with numerical results, the intensities of the lowest lying peaks in $S^{zz}(k, \omega)$ are shown for different momentum transfers in Fig. 7.5(a). In contrast to the spin-1 chain the spectral weights of these peaks seem to vanish in the bulk limit. This clearly indicates that now we are dealing with a spinon pair

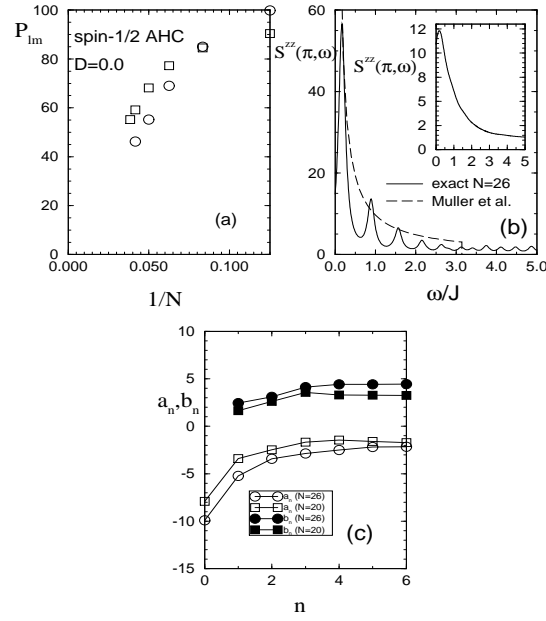


Figure 7.5: (a) Volume dependence of the spectral weight P_{lm} (in %) of the lowest lying excitations in spin-1/2 AHC's with up to 26 sites. Squares : $k = \pi$, octagons : $k = \pi/2$. N is the number of sites. In the bulk limit these weights seem to vanish. (b) Out-of-plane dynamical structure factor for a $N=26$ spin-1/2 AHC (solid line) at $k = \pi$. The delta functions have been given a finite width $\epsilon = 0.1J$. The dashed line is a fit to an approximate analytical expression by Müller et al.. The inset shows the same dynamical spectrum with broadened peaks ($\epsilon = 0.5J$). (c) Lowest order coefficients in the continued fraction expansion for $S^{zz}(k, \pi)$. Octagons denote $N=26$, while squares correspond to $N=20$ spin-1/2 AHC.

continuum as opposed to a single-mode spectrum as in the spin-1 case. As expected, finite size effects play a more important role in the gapless half-odd-integer AHC's than in a massive theory, as can be seen in our plot of $S^{zz}(\pi, \omega)$ (Fig. 7.5(b)). Although the smaller Hilbert space of spin-1/2 chains allows us to easily diagonalize systems of 26 sites, the results still show finite size effects. Actually, we expect that the peaks observed in the spectrum will merge into a continuum increasing the size of the lattice. A combination of several boundary conditions may alleviate this problem. Nevertheless, there is good qualitative agreement between Eq.(7.10) and the numerical results. The inset of Fig. 7.5(b) shows $S^{zz}(\pi, \omega)$ where the occurring poles have been approximated by Lorentzians with a large width $\epsilon = 0.5J$. The artificially broadened dynamical spectrum has the $1/\omega$ -behavior proposed by Müller, and this is roughly the result we expect in the bulk limit when more poles converge into a continuous spectrum.

In Fig. 7.5(c) the first 11 coefficients in the continued fraction expansion for $S^{zz}(\pi, \omega)$ are shown for the N=20 and N=26 chains. In contrast to the spin-1 case the b_n 's have not converged, indicating that the bulk limit has not fully been reached as anticipated. Notice that for easy comparison of the convergence in Fig. 7.2(c) and Fig. 7.5(c) we have chosen cluster sizes which render similar ratios, i.e. $14/18 \approx 20/26$.

7.3 Conclusions

In summary, the dynamical behavior of spin-1/2 and spin-1 AHC's has been studied using numerical techniques. Our data suggests that a single-mode approximation for the massive spin-1 AHC is adequate above $k = 0.3\pi$ in agreement with

recent experiments by Ma et al.[110] From the dynamical structure factor and the scaling of spectral weights with cluster size in the spin-1/2 AHC, we infer the existence of a spin-wave continuum, in contrast to the spin-1 AHC case.

CHAPTER 8

RANDOM EXCHANGE DISORDER IN THE SPIN-1/2 XXZ CHAIN

In this chapter, we study the one-dimensional XXZ model in the presence of disorder in the Heisenberg Exchange Integral. Recent predictions obtained from renormalization group calculations are investigated numerically using a Lanczos algorithm on chains of up to 18 sites. We find that in the presence of strong X-Y-symmetric random exchange couplings, a “random singlet” phase with quasi-long-range order in the spin-spin correlations persists. As the planar anisotropy is varied, the full zero-temperature phase diagram is obtained and compared with predictions of Doty and Fisher [Phys. Rev. B **45**, 2167 (1992)]. In addition, we observe a novel reentrant transition of the ordered phases when exchange disorder is included. The results presented in this chapter have been published by S. Haas, J. Riera, and E. Dagotto in Phys. Rev. B **48**, 3281 (1993).

8.1 Introduction

The study of quantum models in the presence of disorder is an emerging field onto which much attention has been focussed lately. Since all experimentally accessible systems [120] are to some extent affected by randomness in the form of impurities, random magnetic fields, or couplings, a thorough understanding of disorder effects can help in comparing experimental observations and theoretical predictions. In

particular, weakly disordered, low-dimensional quantum spin systems are of interest, since the interplay between randomness and strong quantum fluctuations can be observed.[121] At $T=0$, phase transitions in quantum spin models are driven by zero-point fluctuations, as opposed to thermal excitations in their classical counterparts. However, when a random potential is introduced, phase transitions can be also driven by random fluctuations. This mechanism is particularly interesting in the case of marginally ordered systems, where the long-range Néel order in the 2D isotropic Heisenberg model has been found to be unstable towards thermal fluctuations and random fields, but not towards randomness in the exchange couplings.[122] In this context, ‘marginal order’ alludes to the fact that the gapless spectrum of the Heisenberg system can be destroyed by an infinitesimal Ising-like anisotropy in the Hamiltonian.

8.2 The Heisenberg Chain in the Presence of a Random Exchange Potential

The anisotropic spin-1/2 Antiferromagnetic Heisenberg Chain is a generic model of strongly correlated electrons. It is described by the Hamiltonian,

$$H_0 = J \sum_i (\lambda S_i^z S_{i+1}^z + S_i^x S_{i+1}^x + S_i^y S_{i+1}^y), \quad (8.1)$$

where the notation is standard. Due to the low dimensionality, quantum fluctuations destroy long-range order in the region $-1 < \lambda \leq 1$, and the spin-spin correlations decay spatially following a power-law. Beyond the Heisenberg point (i.e. $\lambda > 1$), a gap opens in the excitation spectrum and the system develops long-range Néel order with exponentially decaying correlation functions, while for $\lambda \leq -1$ there is a ferromagnetic region with Ising-type long-range order.

Let us now introduce disorder in the form of X-Y symmetric random exchange couplings, such that the planar symmetry of H_0 is not broken by the random potential,

$$H_{random} = \sum_i \delta_i (S_i^x S_{i+1}^x + S_i^y S_{i+1}^y). \quad (8.2)$$

The random couplings δ_i are drawn from a uniform distribution $P(\delta_i) = \frac{1}{2\delta J_{xy}} [\theta(\delta_i + \delta J_{xy}) - \theta(\delta_i - \delta J_{xy})]$, where $\langle \delta_i \rangle = 0$ and $\langle (\delta_i)^2 \rangle = (\delta J_{xy})^2/3$. The cut-off parameter δJ_{xy} serves as a measure for the strength of the random potential. The physical properties induced by this distribution are believed to be universal. In order to test this idea, we also studied random exchange couplings drawn from a Gaussian distribution, $P(\delta_i) = \frac{1}{\sqrt{2\pi\sigma_{xy}}} \exp(-\delta_i^2/2\sigma_{xy})$. Here, σ_{xy} serves as a measure of the random strength.

The properties of XXZ chains in the presence of various random potentials have recently been studied by C. A. Doty and D. S. Fisher using renormalization group techniques.[123] It was found that, while random transverse fields destroy the (quasi)-long-range spin order, a power-law decay of the spin correlations may persist in the presence of random exchange couplings as long as the random Hamiltonian does not break the planar symmetry of H_0 . In particular, it was predicted that a quasi-long-range-ordered phase extends from the X-Y regime ($-1 < \lambda \leq 1$), when H_{random} is switched on.

8.3 Diagonalization and Quenched Averaging

In our study of the above system, we numerically diagonalized chains of up to 18 sites with periodic boundary conditions using a Lanczos algorithm. The observables were obtained from a quenched average, i.e. the ground state $|\phi_0(j)\rangle$ of a chain was

evaluated for a given set of random couplings $j = \{\delta_i\}$, and then the expectation value of some particular operators \hat{O} were studied. This procedure was repeated for $m \simeq 500$ (or larger) different sets of random couplings, and finally the algebraic average over all m random samples was taken. The quenched average of an operator \hat{O} is thus defined by

$$\langle\langle\hat{O}\rangle\rangle = \frac{1}{m} \sum_{j=1}^m \langle\phi_0(j)|\hat{O}|\phi_0(j)\rangle. \quad (8.3)$$

First, we would like to address the question of whether quasi-long-range order persists in the region $-1 < \lambda \leq 1$ when the disorder potential H_{random} is switched on. The relevant observable is the normalized real-space spin-spin correlation function

$$\omega^z(l) = \frac{3}{N} \sum_{i=1}^N \frac{\langle\langle S_i^z S_{i+l}^z \rangle\rangle}{S(S+1)}, \quad (8.4)$$

where N denotes the number of sites, and $S = 1/2$ in our study.

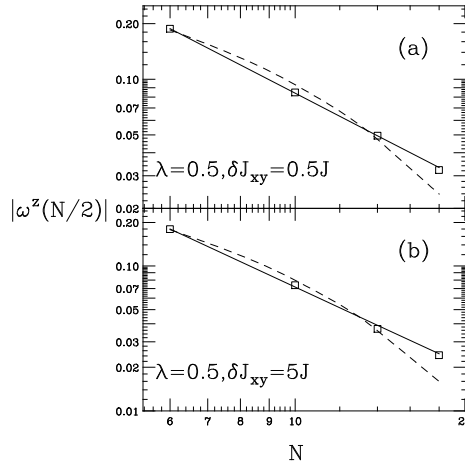


Figure 8.1: Double-logarithmic plot of real-space spin-spin correlations $|\omega^z(l)|$ at maximum separation ($l = N/2$) as a function of lattice size. The squares represent data obtained from exact diagonalizations, the solid lines are fits to a power-law decay $|\omega^z(l)| = Al^{-\eta_z}$ and the dashed lines are fits to an exponential decay $|\omega^z(l)| = A \exp(-\xi l)$. The size of the squares is comparable to the magnitude of the corresponding error bars.

In Fig. 8.1, the spin-spin correlations $\omega^z(N/2)$ at the maximum separation ($l = N/2$) are plotted as a function of the lattice size N at planar anisotropy $\lambda = 0.5$ for a couple of random strengths δJ_{xy} . If the correlations decay with a power-law $|\omega^z(l)| \propto l^{-\eta_z}$, we expect a straight line with negative slope η_z in a double-logarithmic plot. It is found that for all random strengths, δJ_{xy} , a power-law decay (solid line) fits the numerical data much better than an exponential decay (dashed line), e.g. the χ^2 -value obtained from least-square fits is typically two orders of magnitude larger when an exponential decay $|\omega^z(l)| \propto \exp(-\xi l)$ is assumed. We observed a similar power-law behavior in a large region of parameter space.

Why does the random potential not destroy quasi-long-range order in this region? According to Doty and Fisher the “random singlet” phase which extends from the X-Y phase of the pure system (H_0) can be pictured in terms of randomly distributed tightly coupled singlet pairs of spins.[123] Those spins which are not bound in a singlet pair interact via virtual excitations. It turns out that these “almost-free” spins are anomalously strongly correlated. The probability that “almost-free” spins separated by a distance R interact strongly is claimed[123] to be proportional to $1/R^2$. This gives rise to the observed power-law behavior in the spin-spin correlations. The decay exponent is found to be $\eta_z = 2$. Note that in the exactly solvable X-Y limit ($\lambda = 0$) the system maps into a tight-binding model of free fermions with random nearest-neighbor hopping. In this limit the decay exponent is given by $\eta_z = 2$ if a single characteristic localization length is assumed for the properties of the low-energy wave functions.[123]

In Fig. 8.2, we show η_z obtained in our numerical analysis, as a function of the disorder parameter δJ_{xy} for various anisotropies λ . The exponent has been extracted

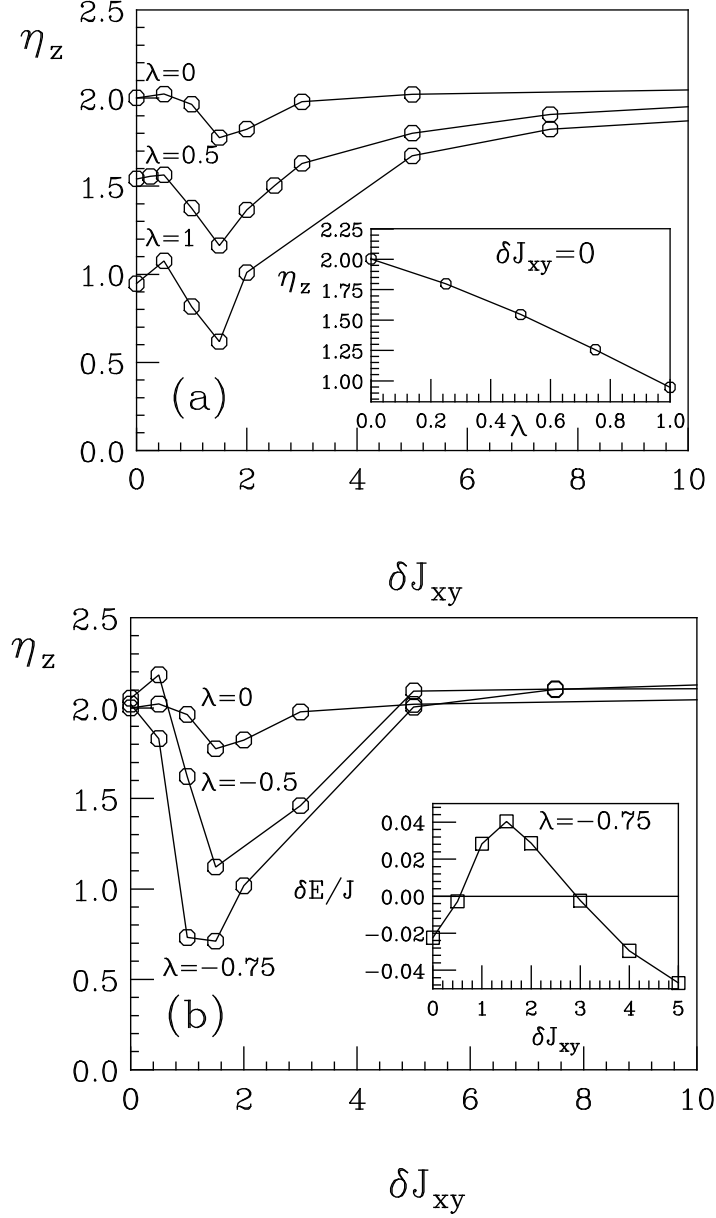


Figure 8.2: Exponents of the power-law decay $|\omega^z(l)| = Al^{-\eta_z}$ as a function of the disorder parameter δJ_{xy} for various positive planar anisotropies. The inset shows η_z as a function of anisotropy in the limit of no disorder. (b) Same as (a) but for negative anisotropies. The inset shows the energy difference $\delta E = E(S_{tot}^z = 0) - E(S_{tot}^z = 1)$ as a function of δJ_{xy} for the 14-site chain. The change in the sign of δE indicates the presence of a partially polarized phase for $0.55J \leq \delta J_{xy} \leq 3.05J$ at anisotropy $\lambda = -0.75$. The error bars are not shown explicitly for clarity, but they are of the order of 10%.

using chains of size $N=6, 10, 14$ and 18 . [124] The inset of Fig. 8.2(a) shows the decay exponent η_z for the pure system H_0 as it has also been obtained in Ref. 6. The exact diagonalization results are in excellent agreement with predictions from conformal invariance,[125] and in particular the Heisenberg limit ($|\omega^z(l)| \propto l^{-1}$) and the X-Y limit ($|\omega^z(l)| \propto l^{-2}$) are nicely recovered. For negative anisotropies, ($-1 < \lambda \leq 0$) conformal invariance predicts a constant exponent $\eta_z = 2$, which is also in reasonable agreement with our data, showing that our techniques can reproduce known results very accurately.

8.4 Phase Diagram of the Spin-1/2 Heisenberg Chain in the Presence of Disorder in the Exchange Integral

On our finite chains, and as we depart from the $\delta J_{xy} = 0$ limit, three regions can be identified:

(1) In the regime of small randomness ($\delta J_{xy} < J$) the exponent η_z increases slightly as a function of the disorder parameter δJ_{xy} , which is a sign of reduced order.[126] However, the size of our error bars ($\sim 10\%$) needs to be improved further to verify this result at small δJ_{xy} .

(2) Around $\delta J_{xy} = J$, there is an area of high competition between the quantum fluctuations of the original Hamiltonian ($J \sum_i (S_i^x S_{i+1}^x + S_i^y S_{i+1}^y)$) and H_{random} . Locally the random terms can compensate the zero-point fluctuations leading to an antiferromagnetic Ising-like behavior in the correlation functions. As a result, the decay exponent η_z has a dent with onset at around $\delta J_{xy} = J$, indicating a crossover into a more ordered Ising-like regime, where correlations decay more slowly than for the uniform system.

(3) For large disorder, ($\delta J_{xy} \gg J$) H_{random} is the dominant term. The dependence of the decay exponent on the planar anisotropy in H_0 becomes negligible, and it approaches $\eta_z = 2$ for all values of λ , as it has been predicted by renormalization group arguments.[123]

In the vicinity of $\lambda = -0.75$ the exponent η_z behaves anomalously for small disorder. The observed decay in η_z for δJ_{xy} between J and $2J$ is due to ferromagnetic behavior in the real space spin-spin correlations. This anomaly is observed specially for anisotropies $-1 < \lambda \leq -0.5$. The dent of η_z around $\delta J_{xy} = J$ can be understood as a crossover into a phase of higher order. In particular, for $\lambda = -0.75$ we observed a transition into a partially polarized phase indicated by the change of sign in the energy difference $\delta E = E(S_{tot}^z = 0) - E(S_{tot}^z = 1)$, where $E(S_{tot}^z = n)$ is the quenched ground state energy in the subspace with $S_{tot}^z = n$. The inset of Fig. 8.2(b) shows δE as a function of the disorder parameter δJ_{xy} at anisotropy $\lambda = -0.75$ for a 14-site chain. It can be nicely seen that the transition into the partially polarized phase ($0.55J \leq \delta J_{xy} \leq 3.05J$) corresponds to the dent in η_z in the same regime of disorder.

In Fig. 8.3(a), the dependence of the energy on the disorder parameters δJ_{xy} and σ_{xy} at various anisotropies is shown for a 14-site chain. As the random potential becomes dominant, the system is allowed to relax into a ground state of higher entropy. The ground state energy drops proportionally to δJ_{xy} (σ_{xy}) in this region. In Fig. 8.3(b), we show how the static structure factor ($S^{zz}(k) = \frac{1}{N} \sum_{i,j} \exp(-ik(i-j)) \langle 0 | S_j^z S_{j+i}^z | 0 \rangle$) behaves as a function of the disorder parameters at antiferromagnetic momentum transfer $k = \pi$ for the 14-site chain. In analogy to Fig. 8.2, three regions can be identified. At low disorder the struc-

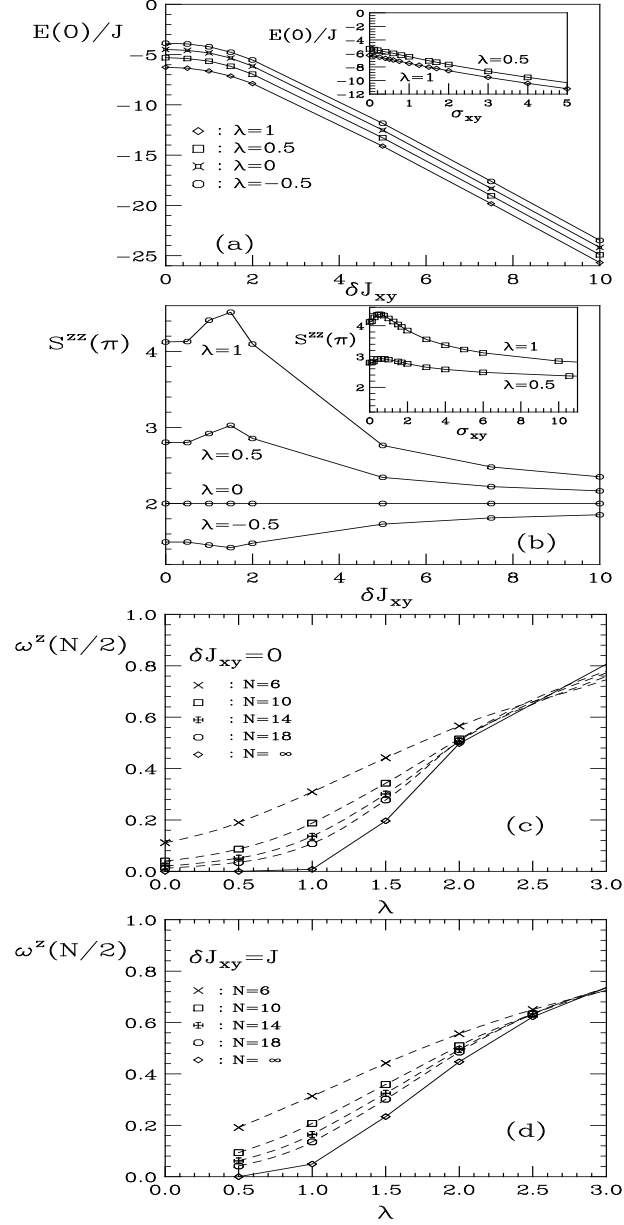


Figure 8.3: (a) Ground state energy of the 14-site spin-1/2 XXZ chain as a function of the disorder parameter δJ_{xy} at various planar anisotropies. The random exchange couplings are drawn from a uniform distribution with cut-off δJ_{xy} . The inset shows the same except when the random exchange couplings are obtained from a Gaussian distribution of width σ_{xy} . (b) Antiferromagnetic structure factor vs. disorder parameter δJ_{xy} for the 14-site spin-1/2 XXZ chain. The inset shows the same but when the random exchange couplings are obtained from a Gaussian distribution of width σ_{xy} . (c) Real space correlation functions at the maximum distance for an N site chain as a function of anisotropy at zero disorder. The bulk limit $N = \infty$ is extracted from a finite size study. (d) Same as (c) at disorder $\delta J_{xy} = J$.

ture factor remains approximately unchanged. In the region of competition, Néel order is favored for positive anisotropies ($0 \leq \lambda \leq 1$), resulting in an increase of the antiferromagnetic structure factor especially in the vicinity of $\lambda \sim 1$. For negative anisotropies ($-1 < \lambda \leq 0$), the ditch in $S^{zz}(\pi)$ indicates a crossover into a ferromagnetically polarized region. For large disorder, $S^{zz}(\pi)$ becomes independent of λ , and approaches the X-Y limit for all anisotropies.

The boundary between the long-range-ordered regime and the “random singlet” phase is obtained from the correlations $\omega^z(N/2)$. In the “random singlet” phase, the spin-spin correlations at distance N vanish in the bulk limit as $N \rightarrow \infty$. However, as the anisotropy is tuned across the critical value λ_c , $\omega^z(N/2)$ becomes finite, approaching $|\omega^z(N/2)| = 1$ in the extreme Ising limit ($\lambda = \infty$). At zero disorder the Heisenberg point $\lambda_c = 1$ is nicely recovered as the critical point (Fig. 8.3(c)). In Fig. 8.3(d), we see that the transition point between these two phases is *reduced* to about $\lambda_c = 0.75$ at $\delta J_{xy} = J$. [127] As a result of the strong competition effects in the region $\delta J_{xy} \simeq J$, the antiferromagnetic phase bends into the random singlet regime in a “*reentrant*” transition, indicating a stronger antiferromagnetic order in this region. The whole boundary between “random singlet” and Néel phase is plotted in the phase diagram given in Fig. 8.4.

Both the “random singlet” and the Néel phase lie in the $S_{total}^z = 0$ subspace. On the other hand, as the ferromagnetic limit is approached, there is a transition into a partially polarized phase, i.e. the ground state no longer has $S_{total}^z = 0$. This phase boundary, as well as the transition from the partially into the fully polarized regime, is extracted from comparing the lowest energies of the various S_{total}^z subspaces (averaged over the ensemble of random couplings). In the region

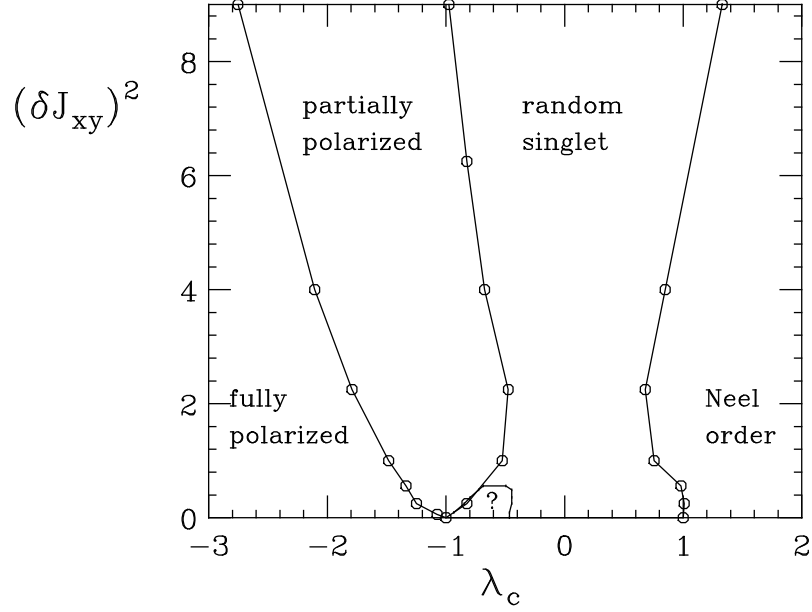


Figure 8.4: Phase diagram of the spin-1/2 XXZ chain in the presence of a random exchange potential. The question mark denotes the “mole hill” phase discussed in the text.

of competition between quantum fluctuations and the disorder term, the partially polarized phase bends into the “random singlet” regime, in analogy to the effect at the phase boundary between the “random singlet” and the Néel phase, as shown in Fig. 8.4.

For low disorder, our results agree qualitatively with those of Doty and Fisher.[123] However, their study predicts an X-Y-like “mole hill” phase in the region $-1 < \lambda \leq -0.5$, and for small disorder. Numerically, it is hard to distinguish this “mole-hill” from the “random singlet” regime, because both phases show power-law behavior in the correlation functions. However, from our exact diagonalization data we have observed a region (denoted with a question mark in Fig. 8.4) which has power-law decay, and is a member of the $S_{total}^z = 0$ subspace, but does not have

any remnant antiferromagnetic correlations, as has been discussed above in the inset of Fig. 8.2(b).

8.5 Conclusions

In summary, we have presented the first numerical study of the spin-1/2 XXZ chain in the presence of a random exchange potential (H_{random}). In contrast to a random field,[128] quasi-long-range order of the zero-disorder X-Y regime $-1 < \lambda \leq 1$ is not destroyed by an X-Y symmetric random exchange. Also, Ising-type long-range order persists in the presence of small random exchange couplings. The power-law behavior in the “random singlet” phase may be due to virtual interactions of “almost-free” spins which are not bound in randomly strong singlet pairs. A complete phase diagram is provided. In addition, we have found an interesting reentrant transition of the ordered phases (in both the ferromagnetic and antiferromagnetic Heisenberg limits) when exchange disorder is included.

CHAPTER 9

MAGNETIC RAMAN SCATTERING IN TWO-DIMENSIONAL SPIN-1/2 HEISENBERG ANTIFERROMAGNETS: SPECTRAL SHAPE ANOMALY AND MAGNETOSTRICTIVE EFFECTS

In this chapter, we calculate the Raman spectrum of the two-dimensional spin-1/2 Heisenberg antiferromagnet by exact diagonalization on a 16-site square cluster and quantum Monte Carlo techniques on clusters of up to 144 sites. The obtained spectra are compared to experimental results for various high- T_c precursors. In spite of the good agreement observed in the position of the main excitation in the B_{1g} channel, i.e., the two-magnon peak around 0.4 eV, an additional mechanism has to be invoked to account for the broad and asymmetric shape of the overall spectrum. This mechanism is motivated in part by recent experimental observations that the Raman linewidth broadens with increasing temperature. Including magnon-phonon interactions by treating the phononic degrees in a quasi-static approximation as an effective renormalization of the exchange integral, our results are in good agreement with Raman scattering experiments on various high- T_c precursors, such as La_2CuO_4 and $\text{YBa}_2\text{Cu}_3\text{O}_{6.2}$. In particular, the calculations reproduce the broad lineshape of the two-magnon peak, the asymmetry about its maximum, the existence of spectral weight at high energies, and the observation of nominally forbidden A_{1g} scattering. The results of this chapter will be published in Phys. Rev. Lett. by F.Nori, R.

Merlin, S. Haas, A.W. Sandvik, and E. Dagotto. A preliminary report was given by S. Haas, E. Dagotto, J. Riera, R. Merlin and F. Nori in J. Appl. Phys. **75**, 6340 (1994).

9.1 Introduction

Raman scattering is a powerful technique to study electronic excitations in strongly correlated systems. Recently, much attention has been given to the anomalous magnetic scattering with a very broad and asymmetric lineshape observed in the Raman spectra of the parent insulating compounds of high- T_c superconductors, such as La_2CuO_4 , and $\text{YBa}_2\text{Cu}_3\text{O}_{6.2}$ at around 3230cm^{-1} and 3080cm^{-1} , respectively [129]. The selection rules associated with this peak are anomalous : while the spin-pair excitations scatter predominantly in the B_{1g} channel, there is also a significant contribution in the nominally forbidden A_{1g} configuration, as well as much weaker B_{2g} and A_{2g} scattering[129].

Previous theoretical studies on the spin-1/2 Heisenberg model for 2D square lattices have computed the Raman spectra and its moments for a nearest-neighbor interaction[130–133] and only the moments when spin interactions along the plaquette diagonal were also included.[134] These show good agreement with experiments regarding the position of the two-magnon peak, but they fail to account for the spectral *shape*, and its enhanced *width*.

Several schemes have been considered to resolve this problem. Initially, from the analysis of the moments it was proposed that strong quantum fluctuations were responsible for the broadening (see, e.g., Ref. [130,134]). However, recent studies of spin-pair excitations in a *spin*-1 insulator, NiPS_3 , show a width comparable to that

of the spin-1/2 cuprates [135]. This questions the view that the observed anomaly is due to large quantum fluctuations intrinsic to spin-1/2 systems. We remark that the measured widths are 3-4 times larger[136] than those predicted by Canali and Girvin [133] within spin-wave theory using the Dyson-Maleev transformation, even when processes involving up to four magnons are taken into account. The work by Canali and Girvin [133] and other groups[137,138] present convincing evidence that the observed anomalous features of the magnetic scattering *cannot* be satisfactorily explained by only considering quantum fluctuations.

In order to explain the observed anomalously broad and asymmetric lineshapes, it seems then necessary to invoke an additional process. Here, we consider the interaction between magnon pairs and phonons [139]. This mechanism is motivated in part by recent experimental observations of a strong broadening of the B_{1g} and an enhancement of the A_{1g} scattering with increasing temperature[140]. In our approach we consider the phonons as static lattice distortions which induce changes, δJ_{ij} , in the exchange integral J of the undistorted lattice. We calculate the Raman spectra for a *nearest-neighbor* Heisenberg model using a *nearest-neighbor* Raman operator in the quenched-phonon approximation which, like the Born-Oppenheimer approach, focuses on the fast (high-energy) magnon modes and freezes the slow (low-energy) phonons. This approximation is valid for the cuprates because there is a clear separation of energies between the magnetic and vibrational modes. For instance, in $\text{YBa}_2\text{Cu}_3\text{O}_6$ the characteristic Debye frequency is about 340cm^{-1} while the two-magnon excitation is $\approx 3080\text{cm}^{-1}$.

9.2 Raman Lineshape without Phonon-Magnon Coupling

The isotropic Heisenberg Hamiltonian is given by $H_0 = J \sum_{\langle ij \rangle} \mathbf{S}_i \cdot \mathbf{S}_j$, where the notation is standard, and only a nearest neighbor interaction is assumed. For the cuprates, the exchange integral is $J \simeq 1450K \simeq 0.12\text{eV}$. In our study, we obtained the ground state $|\phi_0\rangle$ of H_0 on finite 2D square clusters with N spins and periodic boundary conditions using a Lanczos ($N = 16, 26$), and Quantum Monte Carlo (QMC) ($N = 144$) algorithms. We studied zero and finite temperature spectra associated with the *nearest*-neighbor scattering operator [1-4]

$$R = \sum_{\langle ij \rangle} (\mathbf{E}_{inc} \cdot \hat{\sigma}_{ij})(\mathbf{E}_{sc} \cdot \hat{\sigma}_{ij}) \mathbf{S}_i \cdot \mathbf{S}_j, \quad (9.1)$$

where $\mathbf{E}_{inc,sc}$ corresponds to the electric field of the incident and scattered photons, and $\hat{\sigma}_{ij}$ is the unit vector connecting sites i and j . In the cuprates, and for nearest-neighbors only, the irreducible representations of R are B_{1g} , A_{1g} , and E . We concentrate mainly on the dominant B_{1g} scattering, e.g., $\mathbf{E}_{inc} \propto \hat{x} + \hat{y}$ and $\mathbf{E}_{sc} \propto \hat{x} - \hat{y}$. A_{1g} scattering is characterized by $\mathbf{E}_{inc} \propto \hat{x} + \hat{y}$ and $\mathbf{E}_{sc} \propto \hat{x} + \hat{y}$. The phases associated with these two dominant channels are schematically depicted in Fig. 9.1

The spectrum of the scattering operator can be written as

$$I(\omega) = \sum_n |\langle \phi_n | R | \phi_0 \rangle|^2 \delta(\omega - (E_n - E_0)), \quad (9.2)$$

where ϕ_n denotes the eigenvectors of the Heisenberg model with energy E_n . When doing exact diagonalizations on small clusters, the dynamical spectrum $I(\omega)$ is extracted from a continued fraction expansion of the quantity

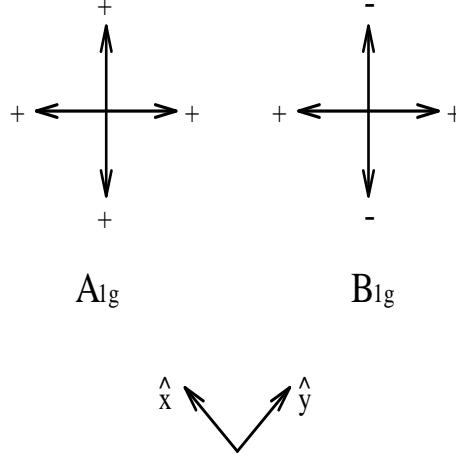


Figure 9.1: Phases associated with the Raman scattering channels

$$I(\omega) = -\frac{1}{\pi} \text{Im} \langle \phi_0 | R \frac{1}{\omega + E_0 + i\epsilon - H_0} R | \phi_0 \rangle, \quad (9.3)$$

where ϵ is a small real number introduced in the calculation to shift the poles of Eq. 9.3 into the complex plane. In the QMC simulations, the imaginary-time correlator $\langle R(\tau)R(0) \rangle$ is calculated and $I(\omega)$ is obtained by numerically continuing this function to real frequencies using a maximum entropy procedure[141].

Our calculated B_{1g} spectra are shown in Fig. 9.2(a). They were obtained from exact diagonalization ($N = 16$) and QMC ($N = 144$) studies of the Heisenberg Hamiltonian on square lattices. The two-magnon excitation observed experimentally lies around $3J$, which is in good agreement with the location of the main peak obtained from exact diagonalization in Fig. 9.2. The position of this peak can be understood in terms of the Ising model, which corresponds to the limit of the anisotropic Heisenberg Hamiltonian when no quantum fluctuations are present. In its ground state, the Ising spins align antiferromagnetically for $J > 0$. Within this model and for a 2D square lattice, the incoming light creates a local spin-pair

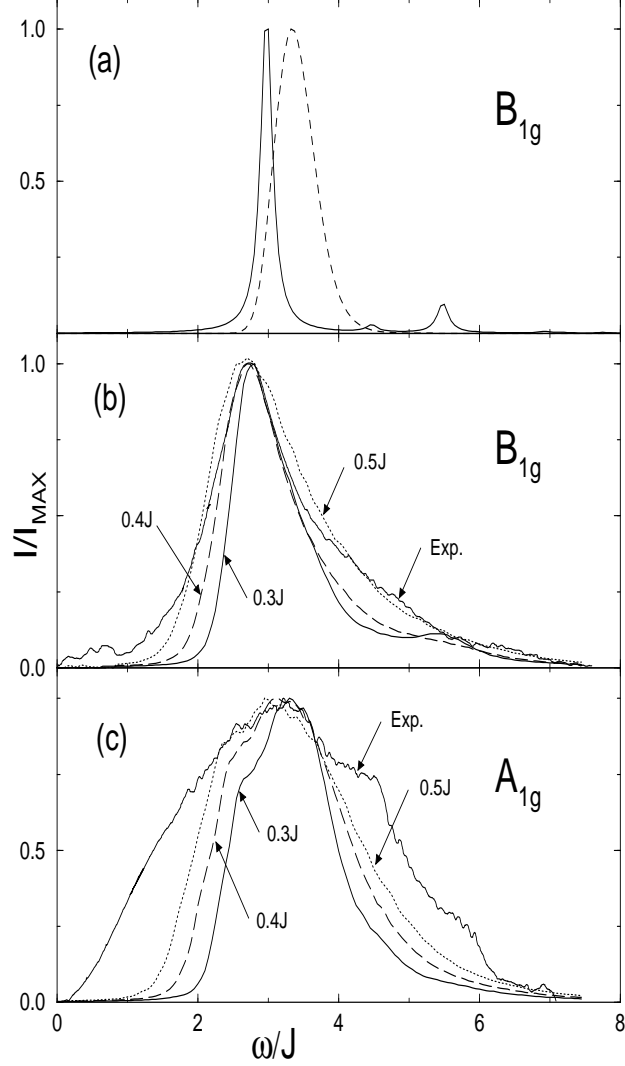


Figure 9.2: Normalized Raman cross section, $I(\omega)/I_{max}$, versus ω/J , for the spin-1/2 Heisenberg model with N sites. (a) B_{1g} Raman spectra obtained from exact diagonalization with $N = 16$, $T = 0$, and $\epsilon = 0.1J$; and from QMC with $N = 144$ and $T = J/4$. B_{1g} (b) and A_{1g} (c) spectra obtained from exact diagonalization ($N = 16$) with randomness in the exchange integral representing the interaction between spin-pairs and the phonons. The continuous, dashed and dotted lines in (b) and (c) correspond, respectively, to $\sigma = 0.3J$, $0.4J$, and $0.5J$. For comparison, the experimental results are shown.

flip at an energy $3J$ higher than the ground state energy. This argument remains approximately valid even in the presence of quantum fluctuations[130–133]. Our results indicate that the two-magnon excitation is at $2.9757J$, $3.0370J$, and $3.2J$ for the 16-, 26-, and 144-site square lattices, respectively. Finite-size effects are small because of the local nature of the Raman operator. For the 144-site lattice, the QMC calculation was carried out at a temperature $T = J/4$ to confirm the position of the two-magnon peak at $3.2J$. This calculation on a larger cluster carries robust error bars since it is not exact for those clusters. The slight shift of the peak position, compared to the $T = 0$ results for the smaller clusters, is consistent with the finite- T exact diagonalization results of Ref.[131]. Statistical errors, absent in the exact diagonalization results but unavoidable in any stochastic simulation, enhance the width of the 144-site spectrum. These results confirm that neither finite-size effects nor finite temperature can account for the discrepancies with the experimental spectra.

9.3 Lineshape Anomaly

The Raman spectra obtained from the pure Heisenberg model (see Fig. 9.2) show good agreement with experiments in regard to the two-magnon peak position, but the calculated width is too small. We will consider here the coupling between the magnon pair and phonons [139,140] to account for the observed wide and asymmetric lineshape. Our mechanism relates to that proposed by Halley [142] to account for two-magnon infrared absorption in, e.g., MnF_2 .

Quantum and thermal fluctuations distort the lattice. The exchange coupling, which depends on the instantaneous positions of the ions, can be expanded in terms

of the their displacements from equilibrium \mathbf{u} . Keeping only the dominant linear terms: $J_{ij}(\mathbf{r}) = J_{ij} = J + \delta J_{ij} = J + \mathbf{u} \cdot \nabla J_{ij}(\mathbf{R})$. Here, δJ_{ij} represents the instantaneous value of $\mathbf{u} \cdot \nabla J_{ij}(\mathbf{R})$, where \mathbf{R} denotes the equilibrium position of the ion carrying the spin (located at $\mathbf{r} = \mathbf{R} + \mathbf{u}$). In the quenched-disorder approximation, the effective Hamiltonian is

$$H_1 = \sum_{\langle ij \rangle} (J + \delta J_{ij}) \mathbf{S}_i \cdot \mathbf{S}_j, \quad (9.4)$$

where $|\delta J_{ij}| < J$ is a random variable corresponding to taking a snapshot of the lattice. This new Hamiltonian is no longer translational invariant.

In our study, the random couplings δJ_{ij} were drawn from a Gaussian distribution $P(\delta J_{ij}) = \exp(-(\delta J_{ij})^2/2\sigma)/\sqrt{2\pi\sigma}$. $I(\omega)$ was obtained as the quenched average over $m \simeq 1000$ realizations of the randomly distorted lattice. The quenched average of an operator \hat{O} is defined by $\langle\langle \hat{O} \rangle\rangle = \frac{1}{m} \sum_{j=1}^m \langle \phi_0(j) | \hat{O} | \phi_0(j) \rangle$, where $\phi_0(j)$ is the ground state of the j th realization of the disordered system.

In Fig. 9.2(b) we show the B_{1g} Raman spectrum from Eq. 9.1 for a 16-sites square lattice with $\sigma \sim 0.4J$, which we found to agree best with experimental spectra [129]. Our calculations do not consider the effect of frozen phonons on the scattering operator R . Notice that the coefficients pertaining to R are generally unrelated to the matrix elements of the system's Hamiltonian (e.g., $\partial J/\partial Q$ in H bears on e^2/r , while the corresponding terms $\propto QS_iS_j$ in R bear on the dipole moment). In particular, and unlike the case without phonons, the fully symmetric A_{1g} component of the scattering operator does not commute with H .

We find that the three main features observed in the B_{1g} configuration[129], namely, the broad lineshape of the two-magnon peak, the asymmetry about its maximum, and the existence of spectral weight up to $\omega \sim 7J$ are well reproduced.

Beyond the two-magnon peak, there is a continuum of phonon-multi-magnon excitations. The small feature around $\omega \simeq 5.5J$ (for $0 \leq \sigma \leq 0.3J$) is compatible with a four-magnon excitation.

9.4 Magnetostriction

Since the effects of the phonon-magnon interaction (i.e., magnetostriction) have not been extensively studied by theoretical work in the cuprates, a few comments are in order. The coupling between the spin and strain degrees of freedom modifies both elastic and magnetic properties. In fact, there are extensive studies on the (sometimes very strong) influence of elasticity on magnetism[143–145]. Mattis and Shultz[143] considered the influence of *uniform compression* (i.e., all bonds *equally distorted*) in their classic study of magnetothermomechanics. Their results were criticized[144] for ignoring the effects of phonons (i.e., *local fluctuations* in the bond lengths, which are taken into account in the present work). Recently, *giant* magnetostrictive effects have been reported in several high- T_c superconductors[146]. Also, important magnetostrictive effects have been reported in heavy-fermion[147] and low- T_c [148] superconductors.

9.5 Superexchange-Phonon Coupling

The width of the Gaussian distribution, σ , represents changes in J due to large *incoherent* atomic displacements. Thus, one can write $\sigma \sim |\langle \delta \ln J / \delta Q \rangle \langle Q \rangle|$ where $\langle Q \rangle$ is an average *zero point motion* (at $T = 0$) and $\langle \delta J / \delta Q \rangle$ is a weighted average of ∇J_{ij} with respect to the displacement of *all* the ions participating in the exchange.

Parenthetically, it is trivial to treat the case $T \neq 0$ by increasing δJ . Let r be the Cu-Cu distance, v the sound velocity, and M an effective reduced mass for the ions. A simple calculation gives $\langle Q \rangle / r \sim (Mvr/\hbar)^{-1/2} \sim 0.05$ which is consistent with X-ray measurements of the mean displacement of oxygen atoms normal to the layers[149,150]. While ∇J_{ij} is not known for most phonons, values for longitudinal acoustic modes can be gained from the r -dependence of J in the form $J(r) \sim r^{-\alpha}$ or $\partial \ln J / \partial \ln r = -\alpha$ [151]. For conventional transition metal oxides and halides, $10 \leq \alpha \leq 14$ [151], in reasonable agreement with the theoretical estimate $\alpha = 14$ [152]. For the cuprates, high-pressure Raman measurements[153] and material trends[154] give, respectively, $\alpha \approx 5 - 7$ and $\alpha \approx 2 - 6$. These values translate into $\sigma \approx (0.1 - 0.35)J$. We emphasize that the relevant *incoherent* δJ 's (or δQ 's) of our case are much larger than those in pressure studies involving *coherent* motion of ions (see, e.g., the discussion in p. 466 of [142]). Thus, we must use larger σ ($\sigma \sim 0.4J$).

Finally, we would like to stress that not every kind of disorder gives rise to the observed broadening of the spectrum. For instance, disorder by point defects or twinning planes will not produce such an effect. Also, it is observed in experiments that the Raman linewidth broadens with increasing temperature[140]. This is a strong indication of a phonon mechanism for the broadening.

9.6 A_{1g} and B_{2g} Symmetries

For the A_{1g} symmetry, the undistorted Raman operator commutes with the Heisenberg Hamiltonian, and *no* scattering can take place. However, the addition of disorder changes the commutator and can produce an A_{1g} signal. Instead, the silent B_{2g} channel remains forbidden within our *nearest-neighbor* Raman operator.

Fig. 9.2(c) shows the comparison between our numerically obtained A_{1g} spectra (for $\sigma \sim 0.4J$) and the experimental results [129,134]. The agreement between theory and experiments is reasonably good. We stress that the A_{1g} scattering follows naturally from our model unlike approaches relying on additional hypotheses, like, for instance, diagonal-nearest-neighbor couplings[134], 4-spin terms[137], new fermionic quasiparticles[155], or spinons. For a detailed discussion of these and other proposed explanations of the lineshape anomaly, see [133,138].

9.7 Conclusions

We find that light scattering spectra by spin excitations is caused by intrinsic spin-spin interactions and also by interactions with phonons. We provide evidence that the two-magnon Raman peak is strongly modified by coupling to low-energy phonons which randomly distort the lattice. Our calculations are in good agreement with experiments and provide a simple explanation of four puzzling features of the data: the broad lineshape of the two magnon peak, the asymmetry about its maximum, the existence of a spectral weight at high energies, and the observation of nominally forbidden A_{1g} scattering.

CHAPTER 10

CONCLUSIONS

Here, we attempt to summarize what can be learned from the Lanczos studies on the dynamics of fermionic systems presented in the preceeding chapters.

The exact diagonalization method enables us to extract very accurate information on the dynamical properties of fermionic systems on finite lattices.[159] In particular, we can study observables which can be measured directly by inelastic Neutron scattering ($S(\mathbf{k}, \omega)$), Raman scattering ($I_{B_{1g}}(\omega)$, $I_{A_{1g}}(\omega)$), and Photoemission spectroscopy ($A(\mathbf{p}, \omega)$). As opposed to the maximum entropy method which is frequently used to analytically continue the imaginary-time Green's functions obtained from Monte Carlo simulations, our method has an arbitrarily fine resolution on the ω -axis without any systematic errors but those intrinsic to the finite size of the lattice.

In the case of the spin-1 Heisenberg chain, there is a gap in the spin-spectrum which corresponds to a finite spin-spin correlation length of roughly 6 lattice spacings.[160] Since we are able to study clusters of up to 18 sites, the physical system is entirely contained in the lattices we can handle numerically. The gapped spectrum is believed to be due to a topological Hopf term in the effective non-linear σ -model this system can be mapped into. This idea has been first proposed by D. Haldane in 1981, and the minimum gap Δ in integer-spin chains corresponding to a massive boson with momentum π has subsequently been called *Haldane gap*. At

momentum-transfer $k=0$, which is not accessible to the Neutron scattering experiment, we expect a gap twice as large as Δ , corresponding to two massive bosons with momenta π and $-\pi$ respectively. This leads to an asymmetry in the dispersion relation about $k=\pi/2$.

In contrast to the Haldane systems, half-odd-integer-spin chains ($S=1/2, 3/2, \dots$) do not have a gap in their spectrum, and their spin dispersion is symmetric about $k=\pi/2$. Since they do not have a finite magnetic correlation length, they can never be entirely contained in a finite cluster, which imposes potential problems to any numerical study of these systems. However, from their spectrum the presence of low-lying modes can be easily identified, and correlations can be measured. A study of clusters of various sizes allows at least for a qualitative analysis of the physics of systems with long-range order. We have shown that some dynamic quantities on finite clusters have a behavior compatible with what is expected for the bulk (i.e. $S(\pi, \omega) \propto 1/\omega$).

While the disorder in the ground state of integer-spin chains is due to topological excitations, we can also study systems where disorder is introduced by external mechanisms such as phononic distortions.[161] To lowest order, phononic distortions can often be treated as a quasi-static perturbation to the spin system, since there is a separation of energy scales by typically an order of magnitude (between optical phonons and magnons). Then, the incoherent part of the phonons simply renormalizes the exchange integral of the spin Hamiltonian in a random manner, e.g. $J \rightarrow J + \delta J_{ij}$, where δ is a parameter that controls the strength of the random renormalization.

In the 1D spin-1/2 chain, we find that disorder that only renormalizes the exchange constant does not necessarily lead to an exponential decay in the real-space spin-spin correlation functions.[162] However, we know from other studies that this is not the case for random magnetic fields. Then our results support the conjecture that a disorder term has to break the continuous symmetry of the original system (here the 1D Heisenberg model) to induce exponential decay in the correlation functions.

However, disorder may very well affect the shape of experimental observables such as the lineshape of the dominant magnetic Raman peaks in the cuprate precursors. It has been an outstanding problem in the Raman community why the two-magnon features observed in the cuprates have a broad width and asymmetry that seem incompatible with calculations on the 2D spin-1/2 Heisenberg antiferromagnet, which has been otherwise very successful in predicting physical properties for these systems. Thus, it seems natural to propose external mechanisms, such as phononic induced disorder, to account for these features. We have shown such a scenario to be compatible with the widths and asymmetries in the B_{1g} and A_{1g} channels observed in the insulating parent compounds of the cuprate superconductors.[161]

Furthermore, a phonon mediated broadening is suggested by the apparent temperature dependence of the observed lineshapes. Also, since the A_{1g} Raman operator commutes with the pure 2D Heisenberg Hamiltonian, there has to be an additional symmetry-breaking term in the model to account for the finite spectral weight observed in that channel. The mechanism we propose produces such a structure which is peaked around an energy transfer of $3J$ consistent with the experiments.

Although we have gained some understanding of the cuprates at half-filling in terms of a 2D Heisenberg antiferromagnet and weak inter-plane magnetic coupling giving rise to a finite Néel temperature of 300K, there is much controversy about what happens in the doped systems. In particular, long-range antiferromagnetic order disappears rapidly upon hole-doping. However, there are strong indications for robust short-range magnetic correlations provided by NMR and Neutron scattering experiments. In contrast to the conventional superconductors, such as Pb where the superconducting condensate forms due to electron-phonon interactions, magnetic fluctuations in the high- T_c materials do not act as “pair-brakers”. On the contrary, there are scenarios which propose spin-fluctuation mediated pair-formation in the doped cuprates.

Then it becomes important to study the effect of short-range magnetic correlations on the Fermi surface of these materials as a function of doping.[163] Indeed, at low enough hole doping ($\delta \leq 15\%$) we have observed two distinct features in the spectral function $A(\mathbf{p}, \omega)$ and the momentum distribution function $n(\mathbf{p}) = \int d\omega A(\mathbf{p}, \omega)$ which deviate from normal Fermi Liquid behavior and can be attributed to short-range antiferromagnetic fluctuations :

- As a remnant of magnetically induced folding of the unit cell at half-filling - the antiferromagnetic unit cell is twice as large as the original unit cell - there are Photoemission bands observed in recent experiments that cannot be understood by simple band theory arguments. However, in our numerical study of the corresponding spectral function, we have argued that these *shadow bands* are possibly induced by short-range antiferromagnetic fluctuations, and should be observable up to a doping level of $\delta \approx 15\%$.

- Some transport measurements on the cuprates at low hole-doping ($\delta < 10\%$) and low temperatures suggest the presence of small pocket-like Fermi surfaces rather than a large topologically connected Fermi surface. We have shown, that there is indeed some evidence suggesting the presence of hole-pockets in both the t-J and the one-band Hubbard model in 1D and 2D.[164] This behavior does not necessarily violate Luttinger's theorem - which states that the volume of the Fermi sea is equal to that of the non-interacting electron gas -, since this conjecture strictly only applies to *non-gapped* metallic systems.

Also, it has been under much discussion whether there is a quasiparticle-like band distinct from the lower Hubbard band in models of strongly correlated electrons. Using both exact diagonalization and Quantum Monte Carlo techniques, we have argued[165] that up to hole-doping levels of $\delta \approx 15\%$ there are two distinct features in the spectral function, namely a lower Hubbard band which disperses with an energy scale given by the hopping integral t , and a quasiparticle band with a smaller energy scale given by the exchange integral J . When the antiferromagnetic correlation length ξ_{AF} becomes negligible (at higher doping levels) there is a crossover into a regime where the dispersion of the quasiparticles resembles that of a weakly interacting system.

Commonly, the long-range Coulomb tail is suppressed in studies of systems of correlated electrons since it is difficult to handle analytically. In our study of the effect of such long-range interactions on the phase diagram of the t-J model, we found that there is a strong competition between superconducting and charge-density-wave phases.[166] We also showed that the modulation of the charge-density-wave depends

strongly on the strength of the interaction parameters. These features are found to be generic for electronic models in low dimensions.

We hope to have shown in this thesis that the exact diagonalization method is a valuable tool to determine the dynamical properties of fermionic systems in the presence of strong Coulomb repulsions and random interactions. In particular, in the absence of controlled analytical techniques which can treat strong correlations without bias, some insight into the physics of the high- T_c cuprates and some organic antiferromagnets has been gained using numerical techniques. With the exponential increase of present day computer capacities we expect to be able to apply the exact diagonalization method to larger clusters in the near future.

APPENDICES

APPENDIX A

STRONG COUPLING EXPANSION OF THE HUBBARD MODEL

This appendix is based on class notes provided by Dan Duffy for the course on high- T_c superconductivity taught by E. Dagotto in the spring of 1994. The derivation of the t-J model is based on "Electron Correlations in Molecules and Solids" (Springer verlag series in solid-states sciences number 100) by P. Fulde. In order to study the effects of strong interactions between electrons, it is useful to study the Hubbard model in the limit of strong coupling, i.e., $U/t \gg 1$. The Hubbard model can be written as:

$$H = U \sum_i n_{i\uparrow} n_{i\downarrow} - t \sum_{\langle i,j \rangle, \sigma} (c_{i\sigma}^\dagger c_{j\sigma} + h.c.) \quad (\text{A.1})$$

$$H = H_U + H_t \quad (\text{A.2})$$

where U contains the strong Coulomb interaction between electrons, t is the hopping integral, $c_{i\sigma}^\dagger$ creates an electron of spin $\sigma = \uparrow$ or \downarrow at site i , while $c_{i\sigma}$ destroys an electron of spin σ at that site. ' i ' denotes a vector, i.e. $i = (i_x, i_y)$ in the 2D case.

If we take the U -term as the unperturbed Hamiltonian, then we have a highly degenerate ground state of energy equal to zero. At half-filling, there is one spin per site (no doubly occupied sites) with a total of 2^N possible configurations. Away from half-filling, the ground state again does not have any doubly occupied sites but it contains holes. The first excited state therefore has an energy of U and contains one doubly occupied site. The second excited state has energy $2U$ with two doubly occupied sites, and so on.

When we apply the hopping term as a perturbation, the degeneracy is lifted. Instead of having all 2^N ground states located at zero energy, there will be a band of states located around the energy of zero. Similarly, the excited states of U , $2U$, etc. become bands of states. By applying perturbation theory up to second order, we can generate an effective Hamiltonian - the t-J Hamiltonian - which corresponds to the lowest energy band of the Hubbard problem.

A.1 Derivation of the Effective Hamiltonian

If we start with the usual matrix equation

$$H | \Psi \rangle = E | \Psi \rangle, \quad (\text{A.3})$$

we can expand $| \Psi \rangle$ in a complete basis that contains all possible spin configurations for a given number of electrons on the lattice. For example, suppose we had a linear chain of four sites with four electrons. Two possible basis states can be constructed by

$$\begin{aligned} | \uparrow \downarrow \uparrow \downarrow \rangle &= c_{1\uparrow}^\dagger c_{2\downarrow}^\dagger c_{3\uparrow}^\dagger c_{4\downarrow}^\dagger | 0 \rangle \\ | \uparrow \downarrow 0 \uparrow \downarrow \rangle &= c_{1\uparrow}^\dagger c_{2\downarrow}^\dagger c_{4\uparrow}^\dagger c_{4\downarrow}^\dagger | 0 \rangle, \end{aligned}$$

where the creation operators are acting on the vacuum state. Then, we can see that we can break the basis states up into two subsets: the lower band which contains no doubly occupied sites (L total states), and the upper band which contains all the rest of the states which have double occupancy (M total states). Therefore,

$$| \Psi \rangle = | \Psi_p \rangle + | \Psi_q \rangle, \quad (\text{A.4})$$

where

$$| \Psi_p > = \sum_l A_l | l > \quad (\text{A.5})$$

$$| \Psi_q > = \sum_m A_m | m > . \quad (\text{A.6})$$

Note that $l \subset n$ (i.e., l is a subset of n) with no doubly occupied sites, and $m \subset n$ with doubly occupied sites.

Now we can write in matrix form, the equation we want to solve, Eq. (A.3).

$$\begin{bmatrix} H_{PP} & H_{PQ} \\ H_{QP} & H_{QQ} \end{bmatrix} \begin{bmatrix} \Psi_P \\ \Psi_Q \end{bmatrix} = E \begin{bmatrix} \Psi_P \\ \Psi_Q \end{bmatrix}$$

Note that we have broken up the Hamiltonian into four parts. H_{PP} is only the part of the Hamiltonian that acts on states with no doubly occupancy, i.e., the lower band. Similarly, H_{QQ} is only that part of the Hamiltonian which acts on states that have at least one doubly occupied site. H_{PQ} and H_{QP} connect the upper and lower bands.

Multiplying these matrices out gives the following matrix equations:

$$H_{PP} | \Psi_p > + H_{PQ} | \Psi_q > = E | \Psi_p > \quad (\text{A.7})$$

$$H_{QP} | \Psi_p > + H_{QQ} | \Psi_q > = E | \Psi_q > \quad (\text{A.8})$$

We can eliminate $| \Psi_q >$ in the equations above to get an expression just for $| \Psi_p >$. However, the order of the operators is important to consider. Therefore, from Eq. (A.8),

$$H_{QP} | \Psi_p > = (E - H_{QQ}) | \Psi_q >$$

$$| \Psi_q \rangle = \frac{1}{E - H_{qq}} H_{qp} | \Psi_p \rangle$$

Now, when we put this result back into Eq. (A.7.), we obtain a “Schroedinger-like” equation for the subspace $| \Psi_p \rangle$ only:

$$(H_{pp} + H_{pq} \frac{1}{E - H_{qq}} H_{qp}) | \Psi_p \rangle = E | \Psi_p \rangle. \quad (\text{A.9})$$

Thus, we can define the effective Hamiltonian to be

$$\tilde{H} = H_{pp} + H_{pq} \frac{1}{E - H_{qq}} H_{qp}. \quad (\text{A.10})$$

Now that the Hilbert space has been divided into two bands, we can create projection operators that will project out the basis states that lie in those bands. Let the lower band have another projection operator P and the upper band projection operator Q . If we only want that part of the Hamiltonian that acts on states of no double occupancy, we need to do the following matrix multiplication:

$$\begin{bmatrix} 1 & 0 \\ 0 & 0 \end{bmatrix} \begin{bmatrix} H_{pp} & H_{pq} \\ H_{qp} & H_{qq} \end{bmatrix} \begin{bmatrix} 1 & 0 \\ 0 & 0 \end{bmatrix} = \begin{bmatrix} H_{pp} & 0 \\ 0 & 0 \end{bmatrix}$$

Therefore, we can write $H_{pp} = PHP$. We can thus define our projection operators P and Q as follows:

$$P = \prod_i (1 - n_{i,\downarrow} n_{i,\uparrow}) \quad (\text{A.11})$$

$$Q = 1 - P. \quad (\text{A.12})$$

Also, we have

$$H_{pp} = PHP, \quad H_{qq} = QHQ \quad (\text{A.13})$$

$$H_{pq} = PHQ, \quad H_{qp} = QHP. \quad (\text{A.14})$$

Putting this into our effective Hamiltonian gives the general result:

$$\tilde{H} = PHP - PHQ \frac{1}{QHQ - E} QHP. \quad (\text{A.15})$$

The second term of the effective Hamiltonian contains operators in the denominator which pose some problem when acting on the state $|\Psi\rangle$. When QHP acts on this state, P projects out only those states with no double occupancy. Then, H, which in this case is only H_t , has to create a double occupancy, otherwise the Q will kill it. Therefore, the fractional term in the effective Hamiltonian only acts on states that have just one doubly occupied site. We need only consider that part of QHQ with U along the diagonal and off diagonal elements of order t. In the limit of large U, we can approximate $QHQ \simeq U$. Then, making an expansion, we can write

$$\frac{1}{QHQ - E} \simeq \frac{1}{U - E} = \frac{1}{U} \left(1 + \frac{E}{U} + \dots\right). \quad (\text{A.16})$$

As U gets large, the large on-site repulsion of the electrons will make the contributions of the upper band to our state $|\Psi\rangle$ small. Therefore, the energy of the state will not diverge as U gets large; it will be finite as $U \rightarrow \infty$. Thus, we can approximate:

$$\frac{1}{QHQ - E} \simeq \frac{1}{U}. \quad (\text{A.17})$$

Then, our effective Hamiltonian in the limit of large U is given by:

$$\tilde{H} = PHP - \frac{1}{U} PHQQHP. \quad (\text{A.18})$$

The second term of the effective Hamiltonian assures that when it acts on some state of our system, it is acting only on one of those states that has no doubly occupied sites. Then, the right H creates a virtual doubly occupied site before the leftmost H moves one of the spins off of the doubly occupied site onto a hole.

A.2 t-J Model

From the definition of P , Eq. (A.11), we can first evaluate PHP . Since the left P ensures that we are acting on states with no double occupancy, we can replace H with just the hopping term of the Hamiltonian. The Coulomb repulsion term does not contribute. Therefore,

$$PHP = PH_tP = -t \prod_l (1 - n_{l\uparrow}n_{l\downarrow}) \sum_{\langle i,j \rangle \sigma} (c_{i\sigma}^\dagger c_{j\sigma} + h.c.) \prod_k (1 - n_{k\uparrow}n_{k\downarrow}). \quad (\text{A.19})$$

We will only need to consider the case when $l = i,j$ and when $k = i,j$. The other terms of the products will become unnecessary later when we claim to only act on states with no double occupancy. Then, we have

$$PH_tP = -t \sum_{\langle ij \rangle} (1 - n_{i\uparrow}n_{i\downarrow})(1 - n_{j\uparrow}n_{j\downarrow}) [c_{i\uparrow}^\dagger c_{j\uparrow} + c_{i\downarrow}^\dagger c_{j\downarrow} + h.c.] (1 - n_{i\uparrow}n_{i\downarrow})(1 - n_{j\uparrow}n_{j\downarrow}).$$

Note that we have explicitly written out the sum over the spins. Let us consider only the first term of the above equation. Since i and j are nearest neighbors i will not be equal to j . We can then commute the i and j operators according to the anticommutation relation

$$c_{i\sigma}^\dagger, c_{j\sigma'} = \delta_{i,j} \delta_{\sigma\sigma'}. \quad (\text{A.20})$$

Therefore, the first term can be written as

$$(1 - n_{i\uparrow}n_{i\downarrow}) c_{i\uparrow}^\dagger (1 - n_{i\uparrow}n_{i\downarrow}) (1 - n_{j\uparrow}n_{j\downarrow}) c_{j\uparrow} (1 - n_{j\uparrow}n_{j\downarrow}).$$

Next note that

$$c_{i\uparrow}^\dagger (1 - n_{i\uparrow}n_{i\downarrow}) = c_{i\uparrow}^\dagger - c_{i\uparrow}^\dagger c_{i\uparrow}^\dagger c_{i\uparrow} n_{i\downarrow} = c_{i\uparrow}^\dagger, \quad (\text{A.21})$$

where we have invoked the Pauli Exclusion Principle:

$$\begin{aligned} c_{j\sigma} c_{j\sigma} | \alpha \rangle &= 0 \\ c_{j\sigma}^\dagger c_{j\sigma}^\dagger | \alpha \rangle &= 0. \end{aligned} \quad (\text{A.22})$$

The first term now looks like $(1 - n_{i\uparrow} n_{i\downarrow}) c_{i\uparrow}^\dagger c_{j\uparrow} (1 - n_{j\uparrow} n_{j\downarrow})$. Since, $c_{i\uparrow}^\dagger$ creates a spin-up and $n_{i\uparrow}$ will just count that spin, we can write $(1 - n_{i\uparrow} n_{i\downarrow}) c_{i\uparrow}^\dagger = (1 - n_{i\downarrow}) c_{i\uparrow}^\dagger$. Therefore, the first term becomes $(1 - n_{i\downarrow}) c_{i\uparrow}^\dagger c_{j\uparrow} (1 - n_{j\downarrow})$. We can then define hole operators, i.e. operators that only give a non-zero result when acting on a hole, by

$$\hat{c}_{i\sigma}^\dagger = c_{i\sigma}^\dagger (1 - n_{i-\sigma}), \quad \hat{c}_{i\sigma} = c_{i\sigma} (1 - n_{i-\sigma}). \quad (\text{A.23})$$

Note that these creation and annihilation operators only act in the reduced Hilbert space of no doubly occupied sites. Therefore, the first term of the PHP term reduces to $\hat{c}_{i\uparrow}^\dagger \hat{c}_{j\uparrow}$. Then the full PHP term can be written as

$$PHP = -t \sum_{\langle i,j \rangle \sigma} (\hat{c}_{i\sigma}^\dagger \hat{c}_{j\sigma} + h.c.). \quad (\text{A.24})$$

In order to evaluate PHQ and QHP, we again use the full Hubbard Hamiltonian, Eq. (A.1). However, since the P projects into the space of no doubly occupied sites, the H_U term in the Hamiltonian will not contribute. We are thus left with the hopping term:

$$\begin{aligned} QH_tP &= (1 - P)H_tP = H_tP - PH_tP \\ &= \sum_{\langle i,j \rangle \sigma} \prod_l (1 - n_{l\uparrow} n_{l\downarrow}) (c_{i\sigma}^\dagger c_{j\sigma} + h.c.) \\ &+ \prod_l (1 - n_{l\uparrow} n_{l\downarrow}) \sum_{\langle i,j \rangle \sigma} (c_{i\sigma}^\dagger c_{j\sigma} + h.c.) \prod_k (1 - n_{k\uparrow} n_{k\downarrow}). \end{aligned} \quad (\text{A.25})$$

As above, we need only to consider those cases where the projection operators have terms of subscript i and j . This leaves us with

$$\begin{aligned} QH_tP &= \sum_{\langle i,j \rangle \sigma} c_{i\sigma}^\dagger c_{j\sigma} (1 - n_{i\uparrow} n_{i\downarrow}) (1 - n_{j\uparrow} n_{j\downarrow}) \\ &+ \sum_{\langle i,j \rangle \sigma} (1 - n_{i\uparrow} n_{i\downarrow}) (1 - n_{j\uparrow} n_{j\downarrow}) c_{j\sigma}^\dagger c_{i\sigma} (1 - n_{i\uparrow} n_{i\downarrow}) (1 - n_{j\uparrow} n_{j\downarrow}). \end{aligned} \quad (\text{A.26})$$

Using the results of Eq. (A.21), we can rearrange the terms in H_tP . Also, using our result for PHP, Eq. (A.24), we can write for the first term of the spin sum

$$QH_tP = \sum_{\langle i,j \rangle} [c_{i\uparrow}^\dagger c_{j\uparrow} (1 - n_{j\uparrow} n_{j\downarrow}) - (1 - n_{i\downarrow}) c_{i\uparrow}^\dagger c_{j\downarrow} (1 - n_{j\downarrow})]. \quad (\text{A.27})$$

Adding the two terms in the above equation gives

$$QH_tP = \sum_{\langle i,j \rangle} n_{i\downarrow} c_{i\uparrow}^\dagger c_{j\uparrow} (1 - n_{j\downarrow}). \quad (\text{A.28})$$

The entire term of QHP can be written as

$$QH_tP = \sum_{\langle i,j \rangle \sigma} (n_{i-\sigma} c_{i\sigma}^\dagger c_{j\sigma} (1 - n_{j-\sigma}) + h.c.). \quad (\text{A.29})$$

A similar argument holds for the PHQ term to get

$$PH_tQ = \sum_{\langle i,j \rangle \sigma} ((1 - n_{i-\sigma}) c_{i\sigma}^\dagger c_{j\sigma} n_{j-\sigma} + h.c.) \quad (\text{A.30})$$

Putting these two terms together is difficult. Initially, one might expect to write two separate pairs of indices, one for the PHQ term and the other for the QHP term. Furthermore, one might expect these pairs of indices, say $\langle i, j \rangle$ and $\langle l, k \rangle$ to be independent of one another. However, that is not the case. The QHP creates a virtual doubly occupied site and relies on the PHQ to remove the doubly occupancy. Therefore, we have only three indices, of which two are nearest neighbors to the third

index. Thus, we can write:

$$PH_tQQH_tP = \sum_{\langle i,j \rangle \langle j,k \rangle \sigma \tau} ((1 - n_{i-\sigma})c_{i\sigma}^\dagger c_{j\sigma} n_{j-\sigma} + h.c.) \\ (n_{j-\tau} c_{j\tau}^\dagger c_{k\tau} (1 - n_{k-\tau}) + h.c.) \quad (\text{A.31})$$

where we have included specifically two different spins σ and τ . We will then have to consider two cases: when the spins are equal and when they are antiparallel. We will only consider the first term of the above equation.

Altogether, there will be four cases to consider: (1) when the spins are parallel and i and k are different, (2) when the spins are antiparallel and i and k are the different, (3) when the spins are parallel and i and k are the same, and (4) when the spins are antiparallel and i and k are the same. We start with the two cases where i and k are different.

Case 1. First, consider when $\sigma = \tau$:

$$\begin{aligned} A &= \sum_{\langle i,j,k \rangle \sigma} (1 - n_{i-\sigma}) c_{i\sigma}^\dagger c_{j\sigma} n_{j-\sigma} n_{j-\sigma} c_{j\sigma}^\dagger c_{k\sigma} (1 - n_{k-\sigma}) \\ &= \sum_{\langle i,j,k \rangle \sigma} \hat{c}_{i\sigma}^\dagger c_{j\sigma} n_{j-\sigma} c_{j\sigma}^\dagger \hat{c}_{k\sigma} \\ &= \sum_{\langle i,j,k \rangle \sigma} \hat{c}_{i\sigma}^\dagger c_{j\sigma} c_{j\sigma}^\dagger n_{j-\sigma} \hat{c}_{k\sigma} \\ &= \sum_{\langle i,j,k \rangle \sigma} \hat{c}_{i\sigma}^\dagger (1 - c_{j\sigma}^\dagger c_{j\sigma}) n_{j-\sigma} \hat{c}_{k\sigma} \\ &= \sum_{\langle i,j,k \rangle \sigma} (\hat{c}_{i\sigma}^\dagger n_{j-\sigma} \hat{c}_{k\sigma} - \hat{c}_{i\sigma}^\dagger n_{j\sigma} n_{j-\sigma} \hat{c}_{k\sigma}) \end{aligned} \quad (\text{A.32})$$

Note that we have used the anticommutation relations of the creation and annihilation operators to move terms around, given by:

$$\begin{aligned} \{c_{i\sigma}^\dagger, c_{j\tau}\} &= \delta_{i,j} \delta_{\sigma,\tau} \\ \{c_{i\sigma}^\dagger, c_{j\tau}^\dagger\} &= 0 \\ \{c_{i\sigma}, c_{j\tau}\} &= 0 \end{aligned} \quad (\text{A.33})$$

Also, note that we have used $n_{j-\sigma}^2 = n_{j-\sigma}n_{j-\sigma} = n_{j-\sigma}$, which is valid since $n_{j-\sigma}$ can be only 0 or 1. Since we start out with states that have no doubly occupied sites, then the last term will not contribute since either $n_{j\sigma}$ or $n_{j-\sigma}$ will be zero. Thus, we are left with the following contribution:

$$A = \sum_{\langle i,j,k \rangle \sigma} \hat{c}_{i\sigma}^\dagger n_{j-\sigma} \hat{c}_{k\sigma}. \quad (\text{A.34})$$

Case 2. Now we will consider the case when i is not the same as k and the spins are antiparallel. This term will be:

$$\begin{aligned} B &= \sum_{\langle i,j,k \rangle \sigma} (1 - n_{i-\sigma}) c_{i\sigma}^\dagger c_{j\sigma} n_{j-\sigma} n_{j\sigma} c_{j-\sigma}^\dagger c_{k-\sigma} (1 - n_{k\sigma}) \\ &= \sum_{\langle i,j,k \rangle \sigma} \hat{c}_{i\sigma}^\dagger c_{j\sigma} n_{j-\sigma} n_{j\sigma} c_{j-\sigma}^\dagger \hat{c}_{k-\sigma} \\ &= \sum_{\langle i,j,k \rangle \sigma} \hat{c}_{i\sigma}^\dagger c_{j\sigma} n_{j-\sigma} c_{j-\sigma}^\dagger n_{j\sigma} \hat{c}_{k-\sigma} \\ &= \sum_{\langle i,j,k \rangle \sigma} \hat{c}_{i\sigma}^\dagger c_{j\sigma} c_{j-\sigma}^\dagger c_{j-\sigma} c_{j-\sigma}^\dagger n_{j\sigma} \hat{c}_{k-\sigma} \\ &= \sum_{\langle i,j,k \rangle \sigma} \hat{c}_{i\sigma}^\dagger c_{j\sigma} c_{j-\sigma}^\dagger (1 - c_{j-\sigma}^\dagger c_{j-\sigma}) n_{j\sigma} \hat{c}_{k-\sigma} \\ &= \sum_{\langle i,j,k \rangle \sigma} \hat{c}_{i\sigma}^\dagger (c_{j\sigma} c_{j-\sigma}^\dagger n_{j\sigma} - c_{j\sigma} c_{j-\sigma}^\dagger c_{j-\sigma}^\dagger c_{j-\sigma} n_{j\sigma}) \hat{c}_{k-\sigma}. \end{aligned} \quad (\text{A.35})$$

The second term of the above tries to create two spins at site j . Since this is not allowed by the Pauli Principle, we must ignore this term. We then have:

$$\begin{aligned} B &= \sum_{\langle i,j,k \rangle \sigma} \hat{c}_{i\sigma}^\dagger c_{j\sigma} c_{j-\sigma}^\dagger n_{j\sigma} \hat{c}_{k-\sigma} \\ &= - \sum_{\langle i,j,k \rangle \sigma} \hat{c}_{i\sigma}^\dagger c_{j-\sigma}^\dagger c_{j\sigma} n_{j\sigma} \hat{c}_{k-\sigma}. \end{aligned} \quad (\text{A.36})$$

Looking at the number operator in the above equation, we can see that it is unnecessary. If there is a spin σ on site j , the number operator will count that spin and then the destruction operator will destroy that spin. If there is no spin σ on site j ,

the number operator returns zero. This has the same effect as if we just applied the destruction operator. This can also be seen from the commutation relations, when we try to permute those two terms. Upon permutation, we are left with a term of $c_{j\sigma}$ and another of $c_{j\sigma}^\dagger c_{j\sigma} c_{j\sigma}$. The second term must be ignored due to the Pauli Principle. Thus, we are left with:

$$B = - \sum_{\langle i,j,k \rangle_\sigma} \hat{c}_{i\sigma}^\dagger c_{j-\sigma}^\dagger c_{j\sigma} \hat{c}_{k-\sigma}. \quad (\text{A.37})$$

Case 3. The next two cases are for i and k being equal. We first consider the case with $\sigma = \tau$. This gives us:

$$\begin{aligned} C &= \sum_{\langle i,j \rangle_\sigma} (1 - n_{i-\sigma}) c_{i\sigma}^\dagger c_{j\sigma} n_{j-\sigma} n_{j\sigma} c_{j\sigma}^\dagger c_{i\sigma} (1 - n_{i-\sigma}) \\ &= \sum_{\langle i,j \rangle_\sigma} \hat{c}_{i\sigma}^\dagger c_{j\sigma} n_{j-\sigma} c_{j\sigma}^\dagger \hat{c}_{i\sigma} \end{aligned} \quad (\text{A.38})$$

Case 4. When the spins are antiparallel:

$$\begin{aligned} D &= \sum_{\langle i,j \rangle_\sigma} \hat{c}_{i\sigma}^\dagger c_{j\sigma} n_{j-\sigma} n_{j\sigma} c_{j-\sigma}^\dagger \hat{c}_{i-\sigma} \\ &= \sum_{\langle i,j \rangle_\sigma} \hat{c}_{i\sigma}^\dagger c_{j\sigma} n_{j\sigma} n_{j-\sigma} c_{j-\sigma}^\dagger \hat{c}_{i-\sigma} \\ &= \sum_{\langle i,j \rangle_\sigma} \hat{c}_{i\sigma}^\dagger c_{j\sigma} c_{j\sigma}^\dagger c_{j\sigma} n_{j-\sigma} c_{j-\sigma}^\dagger \hat{c}_{i-\sigma} \\ &= \sum_{\langle i,j \rangle_\sigma} \hat{c}_{i\sigma}^\dagger (1 - c_{j\sigma}^\dagger c_{j\sigma}) c_{j\sigma} n_{j-\sigma} c_{j-\sigma}^\dagger \hat{c}_{i-\sigma}. \end{aligned} \quad (\text{A.39})$$

The second term above must be ignore because of the Pauli Principle. Continuing, we have:

$$\begin{aligned} D &= \sum_{\langle i,j \rangle_\sigma} \hat{c}_{i\sigma}^\dagger c_{j\sigma} c_{j-\sigma}^\dagger c_{j-\sigma} c_{j\sigma}^\dagger \hat{c}_{i-\sigma} \\ &= \sum_{\langle i,j \rangle_\sigma} \hat{c}_{i\sigma}^\dagger c_{j\sigma} c_{j-\sigma}^\dagger (1 - c_{j-\sigma}^\dagger c_{j-\sigma}) \hat{c}_{i-\sigma} \\ &= \sum_{\langle i,j \rangle_\sigma} \hat{c}_{i\sigma}^\dagger c_{j\sigma} c_{j-\sigma}^\dagger \hat{c}_{i-\sigma}. \end{aligned} \quad (\text{A.40})$$

Note, again we have dropped the second term because of the Pauli Principle.

Putting all four terms (A, B, C, and D) together, the effective Hamiltonian is still incomplete. We have not taken into account the three other terms in Eq. (3.13). When doing so, similar calculations can be made to find the effective Hamiltonian to be:

$$\tilde{H} = H_1 + H_2 + H_3 \quad (\text{A.41})$$

where

$$H_1 = -t \sum_{\langle i,j \rangle_\sigma} (\hat{c}_{i\sigma}^\dagger \hat{c}_{j\sigma} + h.c.) \quad (\text{A.42})$$

$$H_2 = -\frac{2t^2}{U} \sum_{\langle i,j \rangle_\sigma} (\hat{c}_{i\sigma}^\dagger c_{j\sigma} n_{j-\sigma} c_{j\sigma}^\dagger \hat{c}_{i\sigma} + \hat{c}_{i\sigma}^\dagger c_{j\sigma} c_{j-\sigma}^\dagger \hat{c}_{i-\sigma}) \quad (\text{A.43})$$

$$H_3 = -\frac{t^2}{U} \sum_{\langle i,j,k \rangle_\sigma} (\hat{c}_{i\sigma}^\dagger n_{j-\sigma} \hat{c}_{k\sigma} - \hat{c}_{i\sigma}^\dagger c_{j-\sigma}^\dagger c_{j\sigma} \hat{c}_{k-\sigma} + h.c.) \quad (\text{A.44})$$

In order to make the effective Hamiltonian look more like the t-J model, we can rewrite the second term of the Hamiltonian as follows. Only looking at the first term of H_2 , we have:

$$\begin{aligned} \text{1st Term of } H_2 &= \hat{c}_{i\sigma}^\dagger c_{j\sigma} n_{j-\sigma} c_{j\sigma}^\dagger \hat{c}_{i\sigma} \\ &= \hat{c}_{i\sigma}^\dagger c_{j\sigma} c_{j\sigma}^\dagger n_{j-\sigma} \hat{c}_{i\sigma} \\ &= \hat{c}_{i\sigma}^\dagger (1 - c_{j\sigma}^\dagger c_{j\sigma}) n_{j-\sigma} \hat{c}_{i\sigma} \\ &= \hat{c}_{i\sigma}^\dagger n_{j-\sigma} \hat{c}_{i\sigma} - \hat{c}_{i\sigma}^\dagger n_{j\sigma} n_{j-\sigma} \hat{c}_{i\sigma}. \end{aligned} \quad (\text{A.45})$$

The second term will not contribute in the reduced Hilbert space of our problem, i.e., there is no double occupancy at site j. That leaves us with,

$$H_2 = -\frac{2t^2}{U} \sum_{\langle i,j,k \rangle_\sigma} (\hat{c}_{i\sigma}^\dagger n_{j-\sigma} \hat{c}_{i\sigma} + \hat{c}_{i\sigma}^\dagger c_{j\sigma} c_{j-\sigma}^\dagger \hat{c}_{i-\sigma})$$

$$\begin{aligned}
&= -\frac{2t^2}{U} \sum_{\langle i,j,k \rangle_\sigma} ((1 - n_{i-\sigma})n_{i\sigma}n_{j-\sigma}(1 - n_{i-\sigma}) + \hat{c}_{i\sigma}^\dagger c_{j\sigma} c_{j-\sigma}^\dagger \hat{c}_{i-\sigma}) \\
&= -\frac{2t^2}{U} \sum_{\langle i,j,k \rangle_\sigma} ((1 - n_{i-\sigma})n_{i\sigma}n_{j-\sigma} + \hat{c}_{i\sigma}^\dagger c_{j\sigma} c_{j-\sigma}^\dagger \hat{c}_{i-\sigma}), \tag{A.46}
\end{aligned}$$

where we have used $(1 - n_{i-\sigma})^2 = (1 - n_{i-\sigma})$. Thus, if we only consider the reduced Hilbert space of the problem, we have,

$$\begin{aligned}
H_2 &= -\frac{2t^2}{U} \sum_{\langle i,j,k \rangle_\sigma} (n_{i\sigma}n_{j-\sigma} + c_{i\sigma}^\dagger c_{j\sigma} c_{j-\sigma}^\dagger c_{i-\sigma}) \\
&= -\frac{2t^2}{U} \sum_{\langle i,j,k \rangle_\sigma} (n_{i\sigma}n_{j-\sigma} + c_{i\sigma}^\dagger c_{i-\sigma} c_{j\sigma} c_{j-\sigma}^\dagger) \\
&= -\frac{2t^2}{U} \sum_{\langle i,j,k \rangle_\sigma} (n_{i\sigma}n_{j-\sigma} - c_{i\sigma}^\dagger c_{i-\sigma} c_{j-\sigma}^\dagger c_{j\sigma}) \tag{A.47}
\end{aligned}$$

This term seems unfamiliar until we look at the spin operators defined by

$$\vec{S}_i = \frac{1}{2} \sum_{\alpha\beta} c_{i\alpha}^\dagger \vec{\sigma}_{\alpha\beta} c_{i\beta} \tag{A.48}$$

where these operators act in the reduced Hilbert space of no doubly occupied sites.

In component form, the spin operator for site i looks like,

$$S_i^x = \sum_{\alpha\beta} c_{i\alpha}^\dagger \sigma_{\alpha\beta}^x c_{i\beta} \tag{A.49}$$

where σ_x is the usual Pauli spin matrix for a spin 1/2 particle. Also, c_i^\dagger is a row matrix consisting of

$$c_i^\dagger = (c_{i\uparrow}^\dagger, c_{i\downarrow}^\dagger), \tag{A.50}$$

and c_i is just the hermitian conjugate of the above (which gives us a column matrix).

Multiplying out the terms gives us,

$$S_{ix} = \frac{1}{2}(c_{i\uparrow}^\dagger c_{i\downarrow} + c_{i\downarrow}^\dagger c_{i\uparrow}) \tag{A.51}$$

$$S_{iy} = -\frac{i}{2}(c_{i\uparrow}^\dagger c_{i\downarrow} - c_{i\downarrow}^\dagger c_{i\uparrow}) \tag{A.52}$$

$$S_{iz} = \frac{1}{2}(c_{i\uparrow}^\dagger c_{i\uparrow} - c_{i\downarrow}^\dagger c_{i\downarrow}). \tag{A.53}$$

Now look at the dot product of two spins of nearest neighbor sites.

$$\begin{aligned}
\vec{S}_i \cdot \vec{S}_j &= \frac{1}{4}((c_{i\uparrow}^\dagger c_{i\downarrow} + c_{i\downarrow}^\dagger c_{i\uparrow})(c_{j\uparrow}^\dagger c_{j\downarrow} + c_{j\downarrow}^\dagger c_{j\uparrow}) \\
&+ i^2(c_{i\uparrow}^\dagger c_{i\downarrow} - c_{i\downarrow}^\dagger c_{i\uparrow})(c_{j\uparrow}^\dagger c_{j\downarrow} - c_{j\downarrow}^\dagger c_{j\uparrow}) \\
&+ (c_{i\uparrow}^\dagger c_{i\uparrow} - c_{i\downarrow}^\dagger c_{i\downarrow})(c_{j\uparrow}^\dagger c_{j\uparrow} - c_{j\downarrow}^\dagger c_{j\downarrow}))
\end{aligned} \tag{A.54}$$

Several of the above terms will cancel to give us,

$$\begin{aligned}
\vec{S}_i \cdot \vec{S}_j &= \frac{1}{4}(2c_{i\uparrow}^\dagger c_{i\downarrow} c_{j\downarrow}^\dagger c_{j\uparrow} + 2c_{i\downarrow}^\dagger c_{i\uparrow} c_{j\uparrow}^\dagger c_{j\downarrow} \\
&+ n_{i\uparrow} n_{j\uparrow} + n_{i\downarrow} n_{j\downarrow} - n_{i\uparrow} n_{j\downarrow} - n_{i\downarrow} n_{j\uparrow})
\end{aligned} \tag{A.55}$$

Next, we want to look at the above equation minus a factor of $n_i n_j$ where $n_i = n_{i\uparrow} + n_{i\downarrow}$. Then,

$$\begin{aligned}
\vec{S}_i \cdot \vec{S}_j - \frac{1}{4} n_i n_j &= \frac{1}{4}(2c_{i\uparrow}^\dagger c_{i\downarrow} c_{j\downarrow}^\dagger c_{j\uparrow} + 2c_{i\downarrow}^\dagger c_{i\uparrow} c_{j\uparrow}^\dagger c_{j\downarrow} \\
&+ n_{i\uparrow} n_{j\uparrow} + n_{i\downarrow} n_{j\downarrow} - n_{i\uparrow} n_{j\downarrow} - n_{i\downarrow} n_{j\uparrow} \\
&- n_{i\uparrow} n_{j\uparrow} - n_{i\downarrow} n_{j\downarrow} - n_{i\uparrow} n_{j\downarrow} - n_{i\downarrow} n_{j\uparrow}) \\
&= \frac{1}{2}(c_{i\uparrow}^\dagger c_{i\downarrow} c_{j\downarrow}^\dagger c_{j\uparrow} + c_{i\downarrow}^\dagger c_{i\uparrow} c_{j\uparrow}^\dagger c_{j\downarrow} - n_{i\uparrow} n_{j\downarrow} - n_{i\downarrow} n_{j\uparrow}).
\end{aligned} \tag{A.56}$$

If we include the summation over the spins explicitly, we get

$$\vec{S}_i \cdot \vec{S}_j - \frac{1}{4} n_i n_j = \frac{1}{2} \sum_{\sigma} (c_{i\sigma}^\dagger c_{i-\sigma} c_{j-\sigma}^\dagger c_{j\sigma} - n_{i\sigma} n_{j-\sigma}). \tag{A.57}$$

If we consider the reduced Hilbert space, this term is exactly like the second term of our effective Hamiltonian, up to a factor of two. Thus, finally, we have the effective Hamiltonian - the t-J model - including 3-site terms:

$$H_{t-J} = -t \sum_{\langle i,j \rangle_{\sigma}} (\hat{c}_{i\sigma}^\dagger \hat{c}_{j\sigma} + h.c.) \tag{A.58}$$

$$+ J \sum_{\langle i,j \rangle_\sigma} (\vec{S}_i \cdot \vec{S}_j - \frac{1}{4} n_i n_j) \quad (\text{A.59})$$

$$- \frac{t^2}{U} \sum_{\langle i,j,k \rangle_\sigma} (\hat{c}_{i\sigma}^\dagger n_{j-\sigma} \hat{c}_{k\sigma} - \hat{c}_{i\sigma}^\dagger c_{j-\sigma}^\dagger c_{j\sigma} \hat{c}_{k\sigma} + h.c.) \quad (\text{A.60})$$

where the factor J is defined as $J = 4t^2/U$.

The first term of the above t - J model (including the three site term) describes hopping processes of spins from one site to an unoccupied site on the lattice. This process tends to destroy the established antiferromagnetic order since it mixes spins among the two sublattices. This process is shown in Fig A.1(a). Note that this term cannot create a doubly occupied site since we have creation and annihilation operators only acting in the subspace of no double occupancy. The second term is just the interaction of the spins between nearest neighbor sites. This term can cause spin deviations, i.e., spin waves, in the system. One such interaction between spins can cause nearest neighbor spins to flip. Note, though, that the spins do not actually change position, they just change orientation (Fig. A.1(b)).

Finally, the three site terms describe the movement of a spin from a given site to a virtual state that is doubly occupied and finally to a third site which is unoccupied. In effect, the hole is moved from a site k to a site i , i.e., along the diagonal (Fig. A.1(c)). For the most part, the three site terms are ignored. This assumption is really only valid at half-filling when there are no holes. When doping occurs, these terms start to play a role in the Hamiltonian. However, when the doping is low, i.e., you are close to half-filling, it is a good approximation to neglect these terms not only because of a low density of holes, but because of the coefficient in front of the three site terms. Since the coefficient is of order t^2/U , it will play a much smaller role than the H_1 term which has a coefficient of t .

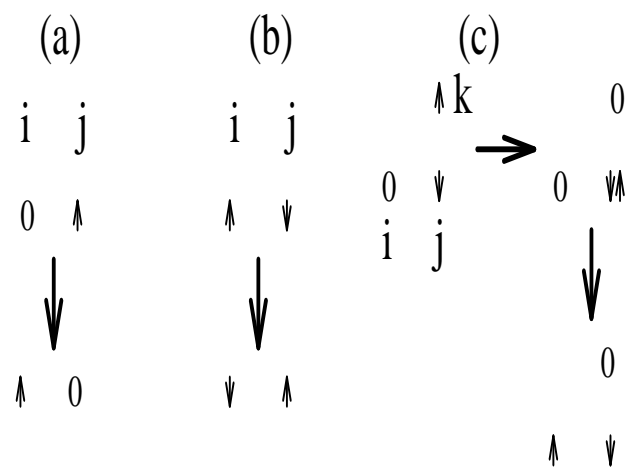


Figure A.1: Hopping processes in the extended t-J model.

APPENDIX B

DIAGONALIZATION OF A 4-SITE CLUSTER

As an illustrative example, mainly directed to beginning graduate students that may be learning the exact diagonalization method, we solve the problem of diagonalizing the Heisenberg Hamiltonian for a 4-site cluster with periodic boundary conditions. The 4-site cluster is unique, since it represents a one-dimensional as well as a two-dimensional system, when periodic boundary conditions are applied. This can be seen when the Heisenberg Hamiltonian is expanded in its individual terms for the two cases :

$$\begin{aligned} H_{1D} &= J \sum_i \mathbf{S}_i \cdot \mathbf{S}_{i+1} = J[\mathbf{S}_1 \cdot \mathbf{S}_2 + \mathbf{S}_2 \cdot \mathbf{S}_3 + \mathbf{S}_3 \cdot \mathbf{S}_4 + \mathbf{S}_4 \cdot \mathbf{S}_1] \\ H_{2D} &= J \sum_{\langle ij \rangle} \mathbf{S}_i \cdot \mathbf{S}_j = J[\mathbf{S}_1 \cdot \mathbf{S}_2 + \mathbf{S}_2 \cdot \mathbf{S}_3 + \mathbf{S}_3 \cdot \mathbf{S}_4 + \mathbf{S}_4 \cdot \mathbf{S}_1] \end{aligned} \quad (\text{B.1})$$

In the 2D case, the bracket denotes summation over nearest neighbor pairs. A convenient basis in which the Hamiltonian operator may be represented is given by all possible Ising configurations ($|\uparrow\uparrow\uparrow\uparrow\rangle, |\downarrow\uparrow\uparrow\uparrow\rangle, |\downarrow\downarrow\uparrow\uparrow\rangle$, etc.). It is easy to see that the Hamiltonian matrix is blockdiagonal corresponding to the accessible S_{tot}^z -subspaces in this representation, e.g. for the 4-site chain we have $S_{tot}^z = -2, -1, 0, 1, 2$. It turns out that the groundstate for the finite systems we consider is usually a singlet state with zero momentum. With that a priori knowledge we will only consider $S_{tot}^z = 0$ in this example. However, there are exceptions to this set of quantum numbers depending on the choice of parameters (like i.e. exchange-coupling and

hopping integrals, or Hubbard repulsion), fillings, boundary conditions and lattice size. The $S_{tot}^z = 0$ basis is given by 6 states :

$$|\downarrow\downarrow\uparrow\uparrow\rangle, |\downarrow\uparrow\downarrow\uparrow\rangle, |\downarrow\uparrow\uparrow\downarrow\rangle, |\uparrow\downarrow\downarrow\uparrow\rangle, |\uparrow\downarrow\uparrow\downarrow\rangle, |\uparrow\uparrow\downarrow\downarrow\rangle. \quad (\text{B.2})$$

In this reduced basis the Hamiltonian assumes the form :

$$H = J \begin{pmatrix} 0 & 1/2 & 0 & 0 & 1/2 & 0 \\ 1/2 & -1 & 1/2 & 1/2 & 0 & 1/2 \\ 0 & 1/2 & 0 & 0 & 1/2 & 0 \\ 0 & 1/2 & 0 & 0 & 1/2 & 0 \\ 1/2 & 0 & 1/2 & 1/2 & -1 & 1/2 \\ 0 & 1/2 & 0 & 0 & 1/2 & 0 \end{pmatrix}, \quad (\text{B.3})$$

where $\hbar = 1$. The eigenvalues and eigenvectors of this small matrix can be obtained analytically. They are given by

eigenvectors	eigenvalues
$\frac{1}{\sqrt{3}}[\downarrow\uparrow\downarrow\uparrow\rangle + \uparrow\downarrow\uparrow\downarrow\rangle] - \frac{1}{\sqrt{12}}[\downarrow\downarrow\uparrow\uparrow\rangle + \downarrow\uparrow\uparrow\downarrow\rangle + \uparrow\downarrow\downarrow\uparrow\rangle + \uparrow\uparrow\downarrow\downarrow\rangle]$	-2J
$\frac{1}{\sqrt{2}}[\downarrow\uparrow\downarrow\uparrow\rangle - \uparrow\downarrow\uparrow\downarrow\rangle]$	-J
$\frac{1}{\sqrt{6}}[\downarrow\uparrow\downarrow\uparrow\rangle + \uparrow\downarrow\uparrow\downarrow\rangle + \downarrow\downarrow\uparrow\uparrow\rangle + \downarrow\uparrow\uparrow\downarrow\rangle + \uparrow\downarrow\downarrow\uparrow\rangle + \uparrow\uparrow\downarrow\downarrow\rangle]$	J
$\frac{1}{2}[\downarrow\downarrow\uparrow\uparrow\rangle - \downarrow\uparrow\uparrow\downarrow\rangle - \uparrow\downarrow\downarrow\uparrow\rangle + \uparrow\uparrow\downarrow\downarrow\rangle]$	0
$\frac{1}{2}[\downarrow\uparrow\uparrow\downarrow\rangle - \uparrow\downarrow\downarrow\uparrow\rangle + i \downarrow\downarrow\uparrow\uparrow\rangle - i \uparrow\uparrow\downarrow\downarrow\rangle]$	0
$\frac{1}{2}[\downarrow\uparrow\uparrow\downarrow\rangle - \uparrow\downarrow\downarrow\uparrow\rangle - i \downarrow\downarrow\uparrow\uparrow\rangle + i \uparrow\uparrow\downarrow\downarrow\rangle]$	0

For the eigenvalue '0' there is a threefold degeneracy. Thus any mutually orthogonal linear combination of the eigenvectors listed for this value would be a solution as well.

By applying the translational operator to the groundstate we verify that the groundstate momentum of this system is indeed $k = 0$. Now we will consider the effect of translating each basis state by one lattice spacing to the right ($r=1$):

$$\begin{aligned}
\hat{T}_{r=1}(k) & \frac{1}{\sqrt{6}} [|\downarrow\uparrow\downarrow\uparrow\rangle + |\uparrow\downarrow\uparrow\downarrow\rangle + |\downarrow\downarrow\uparrow\uparrow\rangle + |\downarrow\uparrow\uparrow\downarrow\rangle + |\uparrow\downarrow\downarrow\uparrow\rangle + |\uparrow\uparrow\downarrow\downarrow\rangle] \\
& = 1 \cdot \frac{1}{\sqrt{6}} [|\uparrow\downarrow\uparrow\downarrow\rangle + |\downarrow\uparrow\uparrow\downarrow\rangle + |\uparrow\downarrow\downarrow\uparrow\rangle + |\downarrow\downarrow\uparrow\uparrow\rangle + |\uparrow\uparrow\downarrow\downarrow\rangle + |\downarrow\uparrow\uparrow\downarrow\rangle] \\
& = e^{(-ikr)} \frac{1}{\sqrt{6}} [|\downarrow\uparrow\downarrow\uparrow\rangle + |\uparrow\downarrow\uparrow\downarrow\rangle + |\downarrow\downarrow\uparrow\uparrow\rangle + |\downarrow\uparrow\uparrow\downarrow\rangle + |\uparrow\downarrow\downarrow\uparrow\rangle + |\uparrow\uparrow\downarrow\downarrow\rangle] \quad (\text{B.4})
\end{aligned}$$

From $e^{(-ikr)} = 1$ it follows that $k = 0$. Similarly it can be shown that the eigenstates with energy $-J$ and J have momentum $k = \pi$ and $k = 0$ respectively. The $E=J$ state differs from the $E=-2J$ state in that it has $S^2 = 1$ while the groundstate is a singlet. The threefold degenerate $E=0$ states have momenta $k = \pi, \pi/4$ and $3\pi/4$ respectively.

Since all eigenstates have momentum as a good quantum number it is a good idea to incorporate the momentum already in the choice of basis states, and thus to decrease the size of the matrix to be diagonalized. Let us set up the basis with momentum $k = 0$ by applying the translational operator to a given representative (i.e. $|\downarrow\downarrow\uparrow\uparrow\rangle$), and generate from this configuration a class of basis states which form a new basis state with good momentum :

$$\begin{aligned}
& e^{(-i0.0)}|\downarrow\downarrow\uparrow\uparrow\rangle + e^{(-i0.1)}|\uparrow\downarrow\uparrow\downarrow\rangle + e^{(-i0.2)}|\uparrow\uparrow\downarrow\downarrow\rangle + e^{(-i0.3)}|\downarrow\uparrow\uparrow\downarrow\rangle, \\
& e^{(-i0.0)}|\downarrow\uparrow\downarrow\uparrow\rangle + e^{(-i0.1)}|\uparrow\downarrow\uparrow\downarrow\rangle \quad (\text{B.5})
\end{aligned}$$

These classes need to be properly normalized by factors $\frac{1}{2}$ and $\frac{1}{\sqrt{2}}$ respectively to become an orthonormal basis. The Hamiltonian in the subspace of $k=0$ is now

represented by a 2x2 matrix

$$H_{k=0} = J \begin{pmatrix} 0 & \sqrt{2} \\ \sqrt{2} & -1 \end{pmatrix}, \quad (\text{B.6})$$

with eigenvalues $-2J$ and J , and the corresponding eigenvectors are given in the table above.

Similarly, the $k = \pi$ block of the Hamiltonian becomes

$$H_{k=\pi} = J \begin{pmatrix} 0 & 0 \\ 0 & -1 \end{pmatrix}, \quad (\text{B.7})$$

which is already diagonal. The subspaces $k = \pi/4$ and $k = 3\pi/4$ have only one state with $E=0$ each.

As can be seen from this example, by introducing symmetries and working in the appropriate S_{tot}^z - subspace the effective Hilbert space for a given problem can be reduced dramatically, in particular for a cluster with N sites translational invariance yields a reduction of almost $1/N$ in the size of the Hilbert space (this becomes exact in the bulk limit $N \rightarrow \infty$).

In addition to the translational symmetry - which in general yields the greatest reduction in Hilbert space - spin-inversion and rotational symmetries can also be implemented. These symmetries typically give a reduction of $1/2$ ($1/4$) in the number of basis states. Using the spin-inversion symmetry the basis can be reduced to

$$\begin{aligned} & \frac{1}{2} [| \downarrow \downarrow \uparrow \uparrow \rangle \pm | \uparrow \uparrow \downarrow \downarrow \rangle], \\ & \frac{1}{2} [| \downarrow \uparrow \downarrow \uparrow \rangle \pm | \uparrow \downarrow \uparrow \downarrow \rangle], \\ & \frac{1}{2} [| \downarrow \uparrow \uparrow \downarrow \rangle \pm | \uparrow \downarrow \downarrow \uparrow \rangle]. \end{aligned} \quad (\text{B.8})$$

The groundstate is contained in the '+'-block

$$H_+ = J \begin{pmatrix} 0 & 1 & 0 \\ 1 & -1 & 1 \\ 0 & 1 & 0 \end{pmatrix}, \quad (\text{B.9})$$

which has eigenvalues $-2J, 0$ and J . Hence these states have even parity under spin-inversion while the remaining three states behave odd under this transformation.

Finally, several symmetries can be applied at the same time. In our example, the subsequent application of even spin-inversion to the $k=0$ basis-subset does not give a Hilbert space size reduction since the two $k=0$ states are already even under spin-inversion. However, for bigger systems the action of the various symmetries decouple, and each one yields a considerable reduction in the number of basis states. Since there still remains a large matrix after exhausting all available symmetries, it becomes important to find algorithms which deal efficiently with large - and in general sparse - matrices. If only the groundstate and the first few excited states which comprise the low-energy physics of a given quantum system are needed, the Lanczos algorithm in particular is a viable numerical tool.

BIBLIOGRAPHY

- [1] Bednorz, J. G., and K. A. Müller, 1986, Z. Phys. B64, 189; Rev. Mod. Phys. 60, 585 (1988).
- [2] D. R. Harshman and A. P. Mills, Phys. Rev. B45, 10684 (1992).
- [3] E. Dagotto, Rev. Mod. Phys. 66, 763 (1994).
- [4] T. Imai et al., Phys. Rev. B47, 9158 (1993).
- [5] C. Almasan and M. B. Maple, “Chemistry of High Temperature Superconductors”, ed. C. N. R. Rao. Singapore: World Scientific (1991).
- [6] see e.g. D. Pines and P. Nozieres, “ The Theory of Quantum Liquids”, W. A. Benjamin (1966).
- [7] H. Y. Hwang et al., Phys. Rev. Lett. 72, 2636 (1994).
- [8] Z. Fisk, private communications.
- [9] S. Chakravarty in *High – Temperature Superconductivity*, eds. K. Bedell, D. Coffey, D. Meltzer, D. Pines, and J. R. Schrieffer, Addison-Wesley, p.136 (1990).
- [10] S. Chakravarty, B.I. Halperin, and D.R. Nelson, Phys. Rev. B39, 7443 (1988).
- [11] B. Keimer et al., Phys. Rev. B46, 14034 (1992).
- [12] M. K. Wu et al., Phys. Rev. Lett.58, 908 (1987).
- [13] J. D. Jorgensen et al., 1988, Phys. Rev. B38, 11337.
- [14] S. Ma et al., Phys. Rev. Lett. 69, 3571 (1992).
- [15] This figure was provided by C. Brunell.

- [16] R. M. White, “Quantum Theory of Magnetism”, pp. 57, McGraw-Hill (1970).
- [17] A. P. Sutton, “Electronic Structure Of Materials”, Oxford science publications, chapters 6 and 9 (1993).
- [18] M.J. Massey et al., Phys. Rev. Lett. **69**, 2299 (1992).
- [19] P. Fulde, “Electron Correlations in Molecules and Solids”, Springer-Verlag series in Solid-State Sciences 100 (1991).
- [20] V. J. Emery, Phys. Rev. Lett. **58**, 2794 (1987).
- [21] M. Hybertsen, M. Schlüter, N. E. Christensen, Phys. Rev. **B39**, 9028 (1989).
M. Hybertsen et al., Phys. Rev. **B41**, 11068 (1990).
- [22] H. Eskes, Ph.D. thesis, Groningen (1992).
- [23] D. Dessau, Ph.D. thesis, Stanford (1992).
- [24] F. C. Zhang and T. M. Rice, 1988, Phys. Rev. **B37**, 3759.
- [25] J. Hubbard, Proc. R. Soc. London, Ser. A **276**, 238 (1963); **281**, 401 (1964).
- [26] C. Lanczos, J. Res. Natl. Bur. Stand. **45**, 255 (1950); D. G. Pettifor, D. L. Weaire (eds.): *The Recursion Method and Its Applications*, Springer Ser. Solid-State Sci., Vol. 58 (Springer, Berlin, Heidelberg 1985).
- [27] W. H. Press et al., Numerical Recipes (Cambridge University Press, Cambridge 1992).
- [28] E. Dagotto and A. Moreo, Phys. Rev. **D31**, 865 (1985).
- [29] E. Gagliano and C. Balseiro, Phys. Rev. Lett. **59**, 2999 (1987).
- [30] J. Oitmaa and D. D. Betts, Can. J. Phys. **56**, 897 (1978).
- [31] In appendix B, we demonstrate how the eigen-problem of this Hamiltonian is solved on a 4-site cluster. This illustrative example should guide the reader through the following sections.
- [32] W. Wenzel and K.G. Wilson, Phys. Rev. Lett. **69**, 800 (1992).

- [33] J. Riera and E. Dagotto, Phys. Rev. B **47**, 15346 (1993).
- [34] T. Imai et al., Phys. Rev. B **47**, 9158 (1993).
- [35] P. Aebi et al., Phys. Rev. Lett. **72**, 2757 (1994); J. Osterwalder et al., Appl. Phys. A **60**, 247 (1995).
- [36] A. Kampf and J. R. Schrieffer, Phys. Rev. B **41**, 6399 (1990); Phys. Rev. B **42**, 7967 (1990).
- [37] E. Dagotto, A. Nazarenko and M. Boninsegni, Phys. Rev. Lett. **73**, 728 (1994); E. Dagotto, A. Nazarenko and A. Moreo, Phys. Rev. Lett. **74**, 310 (1995).
- [38] B. O. Wells et al., Phys. Rev. Lett. **74**, 964 (1995).
- [39] R. N. Silver et al., Phys. Rev. B **41**, 2380 (1990); S. R. White, Phys. Rev. B **44**, 4670 (1991).
- [40] We thank B. O. Wells (private communication) for this suggestion.
- [41] D. Duffy and A. Moreo, Phys. Rev. B **51**, 11882 (1995); R. Eder and Y. Ohta, Phys. Rev. B **51**, 6041 (1995); S. Trugman, Phys. Rev. Lett. **65**, 500 (1990).
- [42] For similar QMC ME results, see N. Bulut, D. J. Scalapino and S. R. White, Phys. Rev. B **50**, 7215 (1994).
- [43] E. Dagotto, F. Ortolani and D. Scalapino, Phys. Rev. B **46**, 3183 (1992); N. Bulut, D. J. Scalapino and S. R. White, Phys. Rev. Lett. **73**, 748 (1994).
- [44] Note also that naively the position of the peaks in states (1,1) and (3,3) of Fig.2 at $\langle n \rangle = 1$ seem different in disagreement with our expectations. However, this just reflects on the low accuracy of the ME method, rather than on the physics of the problem.
- [45] Here, we *assume* that the PES spectral weight induced by antiferromagnetism is mainly a function of ξ_{AF} i.e. we compare numerical and experimental results at different temperatures, but having the same spin correlation.
- [46] E. Dagotto, Rev. Mod. Phys. **66**, 763 (1994).
- [47] These calculations were carried out on a Cray-90 supercomputer and IBM workstations. The largest Hilbert space handled (i.e. $N=18$, 5 holes) contains 816816

states, exploiting the translational invariance symmetry. Typically each PES figure contains about 200 poles.

- [48] E. Dagotto et al., Phys. Rev. B **41**, 9049 (1990).
- [49] Y. Koike et al., Physica C **159**, 105 (1989).
- [50] D.S. Dessau et al., Phys. Rev. Lett. **71**, 2781 (1993); A. A. Abrikosov, J. C. Campuzano, and K. Gofron, Physica C **214**, 73 (1993); D. M. King et al., Phys. Rev. Lett. **73**, 3298 (1994); K. Gofron et al., Phys. Rev. Lett. **73**, 3302 (1994).
- [51] For a comprehensive review, see E. Dagotto, Rev. Mod. Phys. **66**, 763 (1994).
- [52] E. Dagotto, A. Nazarenko and M. Boninsegni, Phys. Rev. Lett. **73**, 728 (1994).
- [53] Z. Liu and E. Manousakis, Phys. Rev. B **45**, 2425 (1992).
- [54] N. Bulut, D. J. Scalapino and S. R. White, Phys. Rev. B **50**, 7215 (1994).
- [55] R. Putz, R. Preuss, A. Muramatsu, and W. Hanke, preprint.
- [56] A. Kampf and J. R. Schrieffer, Phys. Rev. B **41**, 6399 (1990).
- [57] E. Dagotto, A. Nazarenko and A. Moreo, Phys. Rev. Lett. **74**, 310 (1995).
- [58] S. Haas, A. Moreo, and E. Dagotto, Phys. Rev. Lett. **74**, 4281 (1995).
- [59] S. Trugman, Phys. Rev. Lett. **65**, 500 (1990); R. Eder, Y. Ohta, and T. Shimozato, Phys. Rev. B **50**, 3350 (1994).
- [60] P. Aebi et al., Phys. Rev. Lett. **72**, 2757 (1994).
- [61] N. Bulut, D. J. Scalapino and S. R. White, Phys. Rev. Lett. **73**, 748 (1994).
- [62] E. Dagotto and J. R. Schrieffer, Phys. Rev. B **43**, 8705 (1991).
- [63] The third structure immediately after the quasiparticle peak has been extensively analyzed under the name of “string-states”. [51,53] These features should be more sensitive to doping than the dominant quasiparticle state, and thus they are not discussed in detail here.

- [64] M. Jarrell and J. E. Gubernatis, unpublished; R. N. Silver, D. S. Sivia, and J. E. Gubernatis, Phys. Rev. B **41**, 2380 (1990).
- [65] E. Dagotto, F. Ortolani and D. Scalapino, Phys. Rev. B **46**, 3183 (1992).
- [66] The simulations of Ref.[54,61] did not observe such structure mainly due to finite temperature effects and also the use of a different ME technique with less resolution.
- [67] B.O. Wells et al., Phys. Rev. Lett. **74**, 964 (1995).
- [68] A. Nazarenko, K. Vos, S. Haas, E. Dagotto, and R. Gooding, Phys. Rev. B **51**, 8676 (1995).
- [69] R. Eder and Y. Ohta, Phys. Rev. B **50**, 10043 (1994), and references therein.
- [70] This result is to be contrasted with $\mathbf{p} = (0, 0)$. The PES weight at this momenta is not as drastically density-dependent as at (π, π) because for both AF and paramagnetic backgrounds the $(0, 0)$ state is populated at all finite densities.
- [71] R. Preuss, W. Hanke and W. von der Linden, preprint (1994).
- [72] W. Stephan and P. Horsch, Phys. Rev. Lett. **66**, 2258 (1991).
- [73] R. Eder and Y. Ohta, Phys. Rev. Lett. **72**, 2816 (1994); R. Eder and Y. Ohta, Phys. Rev. B **51**, 6041 (1995).
- [74] J.R. Schrieffer, X.G. Wen and S.C. Zhang, Phys. Rev. Lett. **60**, 944 (1988); J.R. Schrieffer, X.G. Wen and S.C. Zhang, Phys. Rev. B **39**, 11663 (1989).
- [75] S. Trugman, Phys. Rev. Lett. **65**, 500 (1990).
- [76] E. Dagotto, A. Nazarenko and M. Boninsegni, Phys. Rev. Lett. **73**, 728 (1994); E. Dagotto, Rev. Mod. Phys. **66**, 763 (1994); E. Dagotto, J. Riera, Y. C. Chen, A. Moreo, A. Nazarenko, F. Alcaraz, and F. Ortolani, Phys. Rev. B **49**, 3548 (1994).
- [77] P.W. Anderson, Physica B **199**, 8 (1994), and references therein.
- [78] R.R.P. Singh and R.L. Glenister, Phys. Rev. B **46**, 14313 (1992).

- [79] R.J. Gooding et al., Phys. Rev. B **49**, 4119 (1994).
- [80] D. Duffy and A. Moreo, Phys. Rev. B **51**, 11882 (1995).
- [81] D. Poilblanc and E. Dagotto, Phys. Rev. B **42**, 4861 (1990).
- [82] C.G. Olson et al., Science **245**, 731 (1989); C.G. Olson et al., Phys. Rev. B **42**, 381 (1990); D.S. Dessau et al., Phys. Rev. Lett. **71**, 2781 (1993).
- [83] The near-degeneracy between $(\pi/2, \pi/2)$, $(\pi, 0)$ and $(0, \pi)$ in the cuprates leads to a quick washing out of pockets from $(0, \pi)$ to $(\pi, 0)$ at small temperatures. In general, the existence of pockets along the $k = k_x = k_y$ direction is a feature very difficult to see. In small lattices, .i.e. 4×4 , 8×8 , not even at $T = 0$, the pockets cannot be observed at the mean field level along the $k_x = k_y$ direction.
- [84] P. Aebi et al., Phys. Rev. Lett. **72**, 2757 (1994); J. Osterwalder et al., Appl. Phys. A **60**, 247 (1995).
- [85] H.J. Schultz, Int. J. Mod. Phys. B **5**, 57 (1991) and references therein.
- [86] M. Ogata et al., Phys. Rev. Lett. **66**, 2388 (1991); M. Ogata and H. Shiba, Phys. Rev. B **41**, 2326 (1990); H. Yokoyama and M. Ogata, Phys. Rev. Lett. **67**, 3610 (1991); H. Shiba and M. Ogata, Prog. Theor. Phys. **108**, 265 (1992).
- [87] E.Dagotto, A. Nazarenko and A. Moreo, Phys. Rev. Lett. **74**, 310 (1995).
- [88] S. Haas, E. Dagotto, A. Nazarenko and J. Riera, Phys. Rev. B **51**, 5989 (1995).
- [89] D. Poilblanc, Phys. Rev. B **44**, 9562 (1991). Instead of taking a full average in the flux parameter space as performed in this reference, in the present study we average over the various possible choices of obtaining a given fixed momentum for $N_h > 1$.
- [90] H.-Q. Ding, Physica C **203**, 91 (1992).
- [91] Another small difference with Refs. [73,90] is concerned with apparent anisotropies they find in Fermi surfaces at odd hole dopings. These anisotropies occur when $n(\mathbf{k})$ is evaluated from $c_{\mathbf{k}}|\textit{groundstate}\rangle$ with $\mathbf{k} \neq 0$. We have obtained the momentum distribution function from $c_0|\textit{groundstate}\rangle = \sum_i c_i|\textit{groundstate}\rangle$ and then taken the Fourier transform, which effectively just averages over the anisotropies in Refs. [73,90] , but seems to be more appropriate because of symmetry.

- [92] W. Putikka, private communications.
- [93] J. Bonca, P. Prelovsek and I. Sega, Solid State Comm. **78**, 109 (1991).
- [94] D. Poilblanc, J. Low Temp. Phys. **99**, 481 (1995).
- [95] T. Tohyama and S. Maekawa, Phys. Rev. B **49**, 3596 (1994).
- [96] V. J. Emery and S. A. Kivelson, Physica C **209**, 597 (1993) and references therein; S. A. Kivelson and V. J. Emery, preprint (1994).
- [97] E. Dagotto and J. Riera, Phys. Rev. Lett. **70**, 682 (1993); Phys. Rev. B **46**, 12084 (1992).
- [98] J. Riera and E. Dagotto, Phys. Rev. B **50**, 3215 (1994).
- [99] A similar proximity of various CDW phases was also observed in a study of a spin-1 Ising chain : U. Löw et al., Phys. Rev. Lett. **72**, 1918 (1994).
- [100] S. Haas, E. Dagotto, A. Nazarenko, and J. Riera, Phys. Rev. B **51**, 5989 (1995).
- [101] G. Müller et.al., Phys. Rev. B **24**, 1429 (1981) and references therein.
- [102] L.D. Fadeev and L.A. Takhtajan. Phys. Lett. **85 A**, 375 (1981).
- [103] J.B. Parkinson and J.C. Bonner, Phys. Rev. B **32**, 4703 (1985); J. Borysowicz, T.A. Kaplan and P. Horsch, Phys. Rev. B **31**, 1590 (1985).
- [104] A. Moreo, Phys. Rev. B **35**, 8562 (1987); Phys. Rev. B **36**, 8582 (1987); F. Alcaraz and A. Moreo, Phys. Rev. B **46**, 2896 (1992).
- [105] Dynamical results for spin chains have been presented by J. Deisz, M. Jarrel and D.L. Cox, Phys. Rev. B **42**, 4869 (1990) using the maximum entropy method. These results were obtained at finite temperature, and with the guidance of a default model. Although the broadening intrinsic to the maximum entropy method prevents a detailed comparison with our exact results for smaller chains, in general we observed an overall good qualitative agreement.
- [106] F.D.M. Haldane, Phys. Rev. Lett. **50**, 1153 (1983); Phys. Lett. A **93**, 464 (1983).

- [107] M. Takahashi, Phys. Rev. Lett. **62**, 2313 (1989); T. Sakai and M. Takahashi, Phys. Rev. B**42**, 1090 (1990); M. Takahashi, Phys. Rev. B**38**, 5188 (1988).
- [108] M.P. Nightingale and H.W. Blöte, Phys. Rev. B**33**, 659 (1986).
- [109] O. Golinelli, T. Jolicoeur and R. Lacaze, Phys. Rev. B**45**, 9798 (1992).
- [110] S. Ma et al., Phys. Rev. Lett. **69**, 3571 (1992).
- [111] W.J.L. Buyers et al., Phys. Rev. Lett. **56**, 371 (1986); Z. Tun et al., Phys. Rev. B**42**, 4677 (1990).
- [112] S.E. Nagler et al., Phys. Rev. B**44**, 12361 (1991); S.E. Nagler et al., J. Mag. Mag. Mat. **102-107**, 847 (1992).
- [113] R.A. Cowley et al., to be published.
- [114] H.A. Bethe, Z. Phys. **71**, 205 (1931).
- [115] J. des Cloiseaux and J.J. Pearson, Phys. Rev. **128**, 2131 (1962).
- [116] E. Dagotto, Int. J. Mod. Phys. B**5**, 907 (1991) and references therein.
- [117] E.R. Gagliano and C.A. Balseiro, Phys. Rev. Lett. **59**, 2999 (1987). See also *The Recursion Method and Its Applications*, edited by D.G. Pettifor and D.L. Weaire (Springer, Berlin Heidelberg, 1985).
- [118] H. Mutka et al., Phys. Rev. Lett. **67**, 497 (1991).
- [119] E. Dagotto et al., Phys. Rev. B**41**, 9049 (1990).
- [120] See, e.g., W. Wu et al., Phys. Rev. Lett. **67**, 2076 (1991); S. Nagler, et al., J. Phys. C : Solid State Phys. **17**, 4819 (1984); G. Theodorou, Phys. Rev. B**16**, 2273 (1977).
- [121] G. Theodorou, Phys. Rev. B**16**, 2264 (1977); W.G. Clark and L.C. Tippie, Phys. Rev. B**20**, 2914 (1979); S. Ma, et al., Phys. Rev. Lett. **43**, 1434 (1979); S.R. Bondeson and Z.G. Soos, Phys. Rev. B**22**, 1793 (1980); C. Das Gupta and S. Ma, Phys. Rev. B**22**, 1305 (1980); J.E. Hirsch, Phys. Rev. B**22**, 5355 (1980); J.E. Hirsch and J.V. José, *ibid.*, 5339 (1980); H.B. Schüttler, et al., Phys. Rev. B**35**, 3461 (1987); K. Runge, Phys. Rev. B**45**, 13136 (1992).

- [122] G. Murthy, Phys. Rev. B **38**, 5162 (1988).
- [123] C.A. Doty and D.S. Fisher, Phys. Rev. B **45**, 2167 (1992).
- [124] The exponent η_z was extracted from finite size data for the correlation function at maximum separation $\omega^z(N/2)$ using $\eta_z(N/2) \sim \frac{\ln(A/\omega^z(N/2))}{\ln(N/2)}$ at large N .
- [125] A. Moreo, Phys. Rev. B **36**, 8582 (1987); F.C. Alcaraz and A. Moreo, Phys. Rev. B **46**, 2896 (1992).
- [126] The error bars in Fig. 2 are approximately 10%. For large disorder ($\delta J_{xy} > J$), a larger number of realizations of the disordered system ($m \simeq 1000$) was necessary to reduce the statistical error to approximately the same level.
- [127] Since the $\omega^z(N/2)$ were measured only at certain anisotropies ($\lambda = 0.0, 0.5, 1.0, \dots$), the critical anisotropies λ_c were roughly obtained from a linear extrapolation using $\omega^z(\infty)$ for λ values closely above the point where the spin gap opens.
- [128] K. Runge and G. Zimanyi, Phys. Rev. B **49**, 15212 (1994).
- [129] K.B. Lyons et al., Phys. Rev. B **39**, 2293 (1989); I. Ohana *et al.*, *ibid* **39**, 2293 (1989); P.E. Sulewski *et al.*, *ibid* **41**, 225 (1990); T. Tokura *et al.*, *ibid* **41**, 11657 (1990); authors S. Sugai *et al.*, *ibid* **42**, 1045 (1990).
- [130] E. Dagotto and D. Poilblanc, Phys. Rev. B **42**, 7940 (1990).
- [131] F. Nori, E. Gagliano, and S. Bacci, Phys. Rev. Lett. **68**, 240 (1992); S. Bacci and E. Gagliano, Phys. Rev. B **43**, 6224 (1991); **42**, 8773 (1990).
- [132] Z. Liu and E. Manousakis, Phys. Rev. B **43**, 13246 (1991).
- [133] C.M. Canali and S.M. Girvin, Phys. Rev. B **45**, 7127 (1992).
- [134] R.R.P. Singh *et al.*, Phys. Rev. Lett. **62**, 2736 (1989).
- [135] S. Rosenblum, A.H. Francis, and R. Merlin, Phys. Rev. B **49**, 4352 (1994).
- [136] H.W. Weber and G.W. Ford, Phys. Rev. B **40**, 6890 (1989).

- [137] S. Sugai, Sol. Stat. Comm. **75**, 795 (1990); M. Roger and J.M. Delrieu, Synthetic Metals **29**, F673 (1989).
- [138] L. Marville, Ph.D. thesis, MIT (1992).
- [139] M.J. Massey, R. Merlin, and S.M. Girvin, Phys. Rev. Lett. **69**, 2299 (1992); J.B. Sokoloff, J. Phys. C **5**, 2482 (1972); M.G. Cottam, J. Phys. C **7**, 2901 (1974).
- [140] P. Knoll *et al.*, Phys. Rev. B **42**, 4842 (1990).
- [141] J.E. Gubernatis *et al.*, Phys. Rev. B **44**, 6011 (1991).
- [142] J.W. Halley, Phys. Rev. **154**, 458 (1967).
- [143] D.C. Mattis and T.D. Shultz, Phys. Rev. **129**, 175 (1963).
- [144] M.E. Fisher, Phys. Rev. **176**, 257 (1968); G.A. Baker and J.W. Essam, Phys. Rev. Lett. **24**, 447 (1970); H. Wagner and J. Swift, Z. Phys. **239**, 182 (1970); H.C. Bolton and B.S. Lee, J. Phys. C **3**, 1433 (1970); F.J. Wegner, *ibid*, 2109 (1974); E. Pytte, Phys. Rev. B **10**, 2039 (1974). D.J. Bergman and B.I. Halperin, Phys. Rev. B **13**, 2145 (1976); Z.-Y. Chen and M. Kardar, *ibid* B **30**, 4113 (1984).
- [145] M. Hase, *et al.*, K. Uchinokura Phys. Rev. Lett. **70**, 3651 (1993); J.P. Pouget, *et al.*, *ibid* **72**, 4037 (1994); K. Hirota, *et al.*, *ibid* **73**, 736 (1994); Q.J. Harris, *et al.*, Phys. Rev. B **50**, 12606 (1994).
- [146] H. Ikuta, *et al.*, Phys. Rev. Lett. **70**, 2166 (1993); A. del Moral, *et al.*, Physica C **161**, 48 (1989); A.M. Kadomtseva, *et al.*, *ibid* **162**, 1361 (1989).
- [147] F.E. Kayzel, *et al.*, Physica B **147**, 231 (1987); A. de Visser *et al.*, *ibid*, **165-166**, 375 (1990).
- [148] M. Isino *et al.*, Phys. Rev. B **38**, 4457 (1988).
- [149] G.H. Kwei, A.C. Lawson, M. Mostoller, Physica C **175**, 135 (1991).
- [150] A.S. Borovik, A.A. Epiphanov, V.S. Malyshevsky, and V.I. Makarov, Phys. Lett. A **161**, 523 (1992).
- [151] see, e.g., M.J. Massey *et al.*, Phys. Rev. B **41**, 8776 (1990), and references therein.

- [152] W.A. Harrison, *Electronic Structure and the Properties of Solids* (Freeman, San Francisco, 1980).
- [153] M. Aronson *et al.*, Z. Fisk, Phys. Rev. B **44**, 4657 (1991).
- [154] S.L. Cooper *et al.*, Phys. Rev. B **42**, 10785 (1990).
- [155] T. Hsu, Phys. Rev. B **41**, 11379 (1990); this Raman lineshape does not agree with experiments, e.g., the A_{1g} and B_{1g} spectra look almost identical, and the asymmetry has the wrong sign.
- [156] J.D. Perkins *et al.*, Phys. Rev. Lett. **71**, 1621 (1993).
- [157] Merlin *et al.*, (unpublished); J. Lorenzana and G.A. Sawatzky, (unpublished); J.R. McBride, L.R. Miller, and W.H. Weber, Phys. Rev. B **49**, 12224 (1994); B. Normand, H. Kohno, and H. Fukuyama (unpublished).
- [158] R. Fehrenbacher, Phys. Rev. B **49**, 12230 (1994).
- [159] E. Dagotto, Rev. Mod. Phys. **66**, 763 (1994).
- [160] S. Haas, J. Riera, and E. Dagotto, Phys. Rev. B **48**, 3281 (1993).
- [161] S. Haas, E. Dagotto, J. Riera, R. Merlin and F.Nori, J. Appl. Phys. **75**, 6340 (1994), F.Nori, R. Merlin, S. Haas, A.W. Sandvik, and E. Dagotto, to appear in Phys. Rev. Lett..
- [162] S. Haas, J. Riera, and E. Dagotto, Phys. Rev. B **48**, 3281 (1993).
- [163] S. Haas, A. Moreo, and E. Dagotto, Phys. Rev. Lett. **74**, 4281 (1995).
- [164] S. Haas, Phys. Rev. B **51**, 11748 (1995).
- [165] A. Moreo, S. Haas, and E. Dagotto, Phys. Rev. B **51**, 12045 (1995).
- [166] S. Haas, E. Dagotto, A. Nazarenko, and J. Riera, Phys. Rev. B **51**, 5989 (1995).

BIOGRAPHICAL SKETCH

Stephan Haas

Education

Vordiplom in Physics, Technische Universität Berlin, Berlin, Germany (October 1989); Master of Science (Physics), Florida State University, Tallahassee, Florida (August 1992); Ph.D. (Physics), Florida State University, Tallahassee, Florida, Summer 1995.

Professional Employment

Teaching Assistant, Department of Physics, Florida State University (1990-1991); Research Assistant, Supercomputer Computations Research Institute (SCRI) and Department of Physics, Florida State University (1991-present).

Honors, Awards and Grants

Fulbright Scholar (1990-1991), SCRI Fellow (1991-present).

Publications

1. *Magnetic Raman scattering in two-dimensional spin-1/2 Heisenberg antiferromagnets : spectral shape anomaly and magnetostrictive effects.* F.Nori, R. Merlin, S. Haas, A.W. Sandvik, and E. Dagotto, to appear in Phys. Rev. Lett..

2. *Antiferromagnetically induced photoemission band in the cuprates.* S. Haas, A. Moreo, and E. Dagotto, Phys. Rev. Lett. **74**, 4281 (1995).
3. *Quasiparticle dispersion of the t - J and Hubbard models.* A. Moreo, S. Haas, and E. Dagotto, Phys. Rev. B **51**, 12045 (1995) (RC).
4. *Photoemission spectra of $Sr_2CuO_2Cl_2$: a theoretical analysis.* A. Nazarenko, K.J.E. Vos, S. Haas, E. Dagotto, and R.J. Gooding, Phys. Rev. B **51**, 8676 (1995) (RC).
5. *Doping dependence of the Fermi surface in the $t - J$ model.* S. Haas, Phys. Rev. B **51**, 11748 (1995).
6. *Liaison between superconductivity and phase separation.* S. Haas, E. Dagotto, A. Nazarenko, and J. Riera, Phys. Rev. B **51**, 5989 (1995).
7. *Raman spectra of two-dimensional spin-1/2 Heisenberg antiferromagnets.* S. Haas, E. Dagotto, J. Riera, R. Merlin and F.Nori, J. Appl. Phys. **75**, 6340 (1994).
8. *Magnetic properties of an isolated ferromagnetic bond embedded in Heisenberg antiferromagnets.* S.T. Ting, S. Haas, and J.E. Crow, J. Appl. Phys. **75**, 6748 (1994).
9. *Random Exchange Disorder in the spin-1/2 XXZ chain.* S. Haas, J. Riera, and E. Dagotto, Phys. Rev. B **48**, 3281 (1993) (RC).
10. *Dynamical properties of antiferromagnetic Heisenberg spin chains.* S. Haas, J. Riera, and E. Dagotto, Phys. Rev. B **48**, 3281 (1993).

11. *Magnetic properties of an isolated missing link in the anisotropic two-dimensional Heisenberg antiferromagnet.* S. Haas, J. Appl. Phys. **73**, 6642 (1993).
12. *Isolated ferromagnetic bonds in the two-dimensional spin-1/2 Heisenberg antiferromagnet.* S. Haas, D. Duffy, et al., Phys. Rev. B **46**, 3135 (1992).